

Dissertation  
submitted to the  
Combined Faculties for the Natural Sciences and for Mathematics  
of the Ruperto-Carola University of Heidelberg, Germany  
for the degree of  
Doctor of Natural Sciences

presented by  
Dipl.-Phys. Arnd Roth  
born in Heilbronn, Germany  
Oral examination: 21st April 2004



# New biophysical methods for the characterization of signal transfer in neurons

Referees:

Prof. Dr. Bert Sakmann  
Prof. Dr. Winfried Denk



## **Neue biophysikalische Methoden zur Charakterisierung der Signalübertragung in Nervenzellen**

Viele Nervenzellen besitzen ausgedehnte Dendritenbäume, und die somatische Spannungsklemme dendritischer Synapsen führt daher zu Verzerrungen und Abschwächungen der gemessenen synaptischen Ströme. Eine neue Methode wird vorgestellt, die die genaue Bestimmung der Abfallszeitkonstante der synaptischen Leitfähigkeit, unabhängig von der Geometrie der Zelle und dem elektrotonischen Ort der Synapse, erlaubt. In allen getesteten Geometrien wurde der Zeitverlauf der synaptischen Leitfähigkeit auch bei hohen Serienwiderständen, geringen Membranwiderständen und distalen, verteilten Synapsen mit hoher Genauigkeit rekonstruiert. Die Methode liefert auch den Zeitverlauf der Spannungsantwort am Ort der Synapse auf einen somatischen Spannungssprung, und ist daher nützlich bei der Konstruktion von Kompartimentmodellen von Nervenzellen und zur Abschätzung des relativen elektrotonischen Abstands von Synapsen.

Die Ausbreitung dendritischer Aktionspotentiale verbindet die Informationsverarbeitung in verschiedenen Regionen des Dendritenbaums. Trotz identischer Vorschriften für die Platzierung von spannungsgesteuerten Kanälen verursachten verschiedene dendritische Verzweigungsmuster in Kompartimentmodellen von Nervenzellen eine Verteilung verschieden starker Aktionspotentialausbreitung, wie sie auch experimentell beobachtet wird. Das Verzweigungsmuster bestimmt auch, zu welchem Grad die Modulation von Kanaldichten die Aktionspotentialausbreitung verändern kann. Die Vorwärtsausbreitung dendritisch initiiertes Aktionspotentiale wird von der Geometrie auf ähnliche Weise beeinflusst. Indem sie das räumliche Muster der Aktionspotentialausbreitung bestimmt, trägt die dendritische Geometrie maßgeblich dazu bei, die Größe und Wechselwirkung zwischen funktionellen Kompartimenten in einer Nervenzelle zu bestimmen.

## **New biophysical methods for the characterization of signal transfer in neurons**

Many neurons have extensive dendritic trees, and therefore somatic voltage clamp of dendritic synapses is often associated with substantial distortion and attenuation of the synaptic currents. A new method is presented which permits faithful extraction of the decay time constant of the synaptic conductance independent of dendritic geometry and the electrotonic location of the synapse. The decay time course of the synaptic conductance was recovered with high accuracy in all the tested geometries, even with high series resistances, low membrane resistances, and electrotonically remote, distributed synapses. The method also provides the time course of the voltage change at the synapse in response to a somatic voltage clamp step, and thus will be useful for constraining compartmental models and estimating the relative electrotonic distance of synapses.

Action potential propagation in dendrites links information processing in different regions of the dendritic tree. In simulations using compartmental models with identical complements of voltage-gated channels, different dendritic branching patterns caused a range of backpropagation efficacies, similar to that observed experimentally. Dendritic geometry also determines the extent to which modulation of channel densities can affect propagation. Forward propagation of dendritically initiated action potentials is influenced by geometry in a similar manner. By determining the spatial pattern of action potential signalling, dendritic geometry thus helps to define the size and interdependence of functional compartments in the neuron.



# Contents

|   |    |
|---|----|
| 1 Introduction .....  | 1  |
| 1.1 The cable equation.....   | 7  |
| 1.1.1 Main assumptions.....   | 7  |
| 1.1.2 The linear cable equation.....  | 8  |
| 1.1.3 Steady-state solution in an infinite cable.....   | 10 |
| 1.2 Compartmental models .....  | 10 |
| 1.2.1 Introduction.....   | 10 |
| 1.2.2 The Hodgkin–Huxley model.....   | 11 |
| 1.2.3 The NEURON simulation environment .....   | 13 |
| 2 Estimating the time course of the synaptic conductance under conditions of<br>inadequate space clamp .....                          | 15 |
| 2.1 Introduction .....  | 15 |
| 2.2 Methods .....   | 17 |
| 2.2.1 Equivalent cylinder model.....  | 17 |
| 2.2.2 CA3 pyramidal cell model .....  | 17 |
| 2.2.3 Neocortical pyramidal cell model .....  | 18 |
| 2.3 Results .....   | 19 |
| 2.3.1 Attenuation and filtering of synaptic currents under poor space-clamp<br>conditions.....  | 19 |
| 2.3.2 Measuring charge recovery .....   | 20 |
| 2.3.3 Charge recovery after the onset of the synaptic conductance is<br>determined by the conductance time course .....               | 22 |
| 2.3.4 Charge recovery before the onset of the synaptic conductance is<br>determined by the electrotonic distance of the synapse ..... | 25 |
| 2.3.5 A simple analytical function describes the charge recovery curve .....  | 25 |
| 2.3.6 The voltage jump method also works in current-clamp mode.....   | 29 |
| 2.3.7 Effect of voltage escape at the synapse .....   | 29 |
| 2.3.8 Application to realistic neuronal geometries: CA3 pyramidal cell.....   | 31 |
| 2.3.9 Application to realistic neuronal geometries: Neocortical pyramidal cell..  | 35 |

|   |    |
|---|----|
| 2.3.10 Estimating synaptic conductance time course with a train of brief voltage jumps .....                    | 37 |
| 2.3.11 Estimating the attenuation of synaptic charge .....  | 39 |
| 2.4 Discussion .....  | 43 |
| 2.4.1 Comparison with previous approaches .....   | 43 |
| 2.4.2 Sources of error.....   | 44 |
| 2.4.3 Application to neocortical pyramidal cells.....   | 46 |
| 2.4.4 Application to Bergmann glia cells.....   | 49 |
| 2.4.5 Application to hippocampal interneurons.....  | 50 |
| 2.4.6 Application in cerebellar granule cells .....   | 51 |
| 2.4.7 Future applications of the voltage jump method .....  | 51 |
| <br>  |    |
| 3 Propagation of action potentials in dendrites depends on dendritic geometry .....                             | 53 |
| <br>  |    |
| 3.1 Introduction .....  | 53 |
| <br>  |    |
| 3.2 Methods .....   | 55 |
| 3.2.1 Dendritic geometries .....  | 55 |
| 3.2.2 Compartmental models .....  | 55 |
| 3.2.3 Measurements.....   | 57 |
| <br>  |    |
| 3.3 Results.....  | 58 |
| 3.3.1 Action potential backpropagation depends on dendritic geometry .....                                      | 58 |
| 3.3.2 Sensitivity of backpropagation to modulation of channel densities in different dendritic geometries ..... | 60 |
| 3.3.3 Morphological determinants of backpropagation .....   | 63 |
| 3.3.4 Forward propagation of dendritic APs depends on dendritic geometry ...                                    | 68 |
| <br>  |    |
| 3.4 Discussion .....  | 72 |
| 3.4.1 The link between dendritic geometry and propagation .....   | 72 |
| 3.4.2 Modulation of AP propagation in dendrites.....  | 74 |
| 3.4.3 Implications for dendritic computation .....  | 75 |
| <br>  |    |
| 4 Comprehensive discussion .....  | 77 |
| <br>  |    |
| 4.1 Applications of the voltage jump method .....   | 77 |



---

|   |     |
|---|-----|
| 4.2 Validation of compartmental models .....        | 79  |
| 4.3 Functional compartments in dendritic trees..... | 80  |
| 4.4 Simple versus complex models.....               | 81  |
| 4.5 Acknowledgements .....                          | 83  |
| <br>  |     |
| 5 References.....                                   | 85  |
| 5.1 References cited .....                          | 85  |
| 5.2 Vita.....                                       | 101 |
| 5.3 Publications.....                               | 102 |
| 5.3.1 Papers .....                                  | 102 |
| 5.3.2 Book chapters.....                            | 103 |
| 5.3.3 Abstracts.....                                | 104 |
| <br>  |     |
| 6 Abbreviations .....                               | 107 |



# 1 Introduction

Progress in science depends on new techniques, new discoveries, and new ideas, probably in that order. – Sydney Brenner

Typical neurons in the brain consist of a cell body or "soma" containing the nucleus, and two types of tree-like processes emerging from it: the dendrites and an axon. In the classical view of signal processing in the brain, the dendrites receive information from other neurons, while the axon transmits information on to other neurons (Ramón y Cajal, 1904). The dendrites of different neuronal types have characteristic branching patterns (Fig. 1.1), as do the axons. Neurons are connected to each other via synapses, where an electrical action potential in the presynaptic (sending) axon causes the release of vesicles containing neurotransmitter molecules from the presynaptic element of the synapse, which subsequently diffuse in the synaptic cleft between the pre- and postsynaptic elements and bind to ligand-gated ion channels in the postsynaptic membrane. Ligand binding leads to opening of these channels, resulting in an additional electrical conductance in the postsynaptic membrane, which causes a current to flow at the location of the synapse.

If we look more closely the picture becomes much more complicated since chemical synaptic transmission involves a long cascade of signalling mechanisms. In addition, there is electrical transmission, caused by gap junctions which mediate direct electrical connections between neurons, and retrograde chemical transmission whereby messenger substances released from the postsynaptic neuron act on presynaptic receptor molecules. Retrograde signalling of this type can cause long-term changes in the characteristics of synaptic transmission.

Here I focus on what happens in the postsynaptic neuron once a synaptic conductance has been activated, a process called synaptic integration. In its simplest form, the neuron is described as a single, isopotential compartment, with a single state variable, the membrane potential. Synaptic currents change the membrane potential by charging or discharging the membrane capacitance, and any resulting perturbations away from the resting potential of the cell decay exponentially due to a constant membrane resistance in parallel to the membrane capacitance, with a time constant equal to the product of the membrane capacitance and the membrane resistance. When the membrane potential reaches a certain threshold value, the neuron instantaneously fires a spike and resets the membrane potential. This abstraction of neuronal function is generally referred to as the integrate-and-fire neuron (Lapicque, 1907).

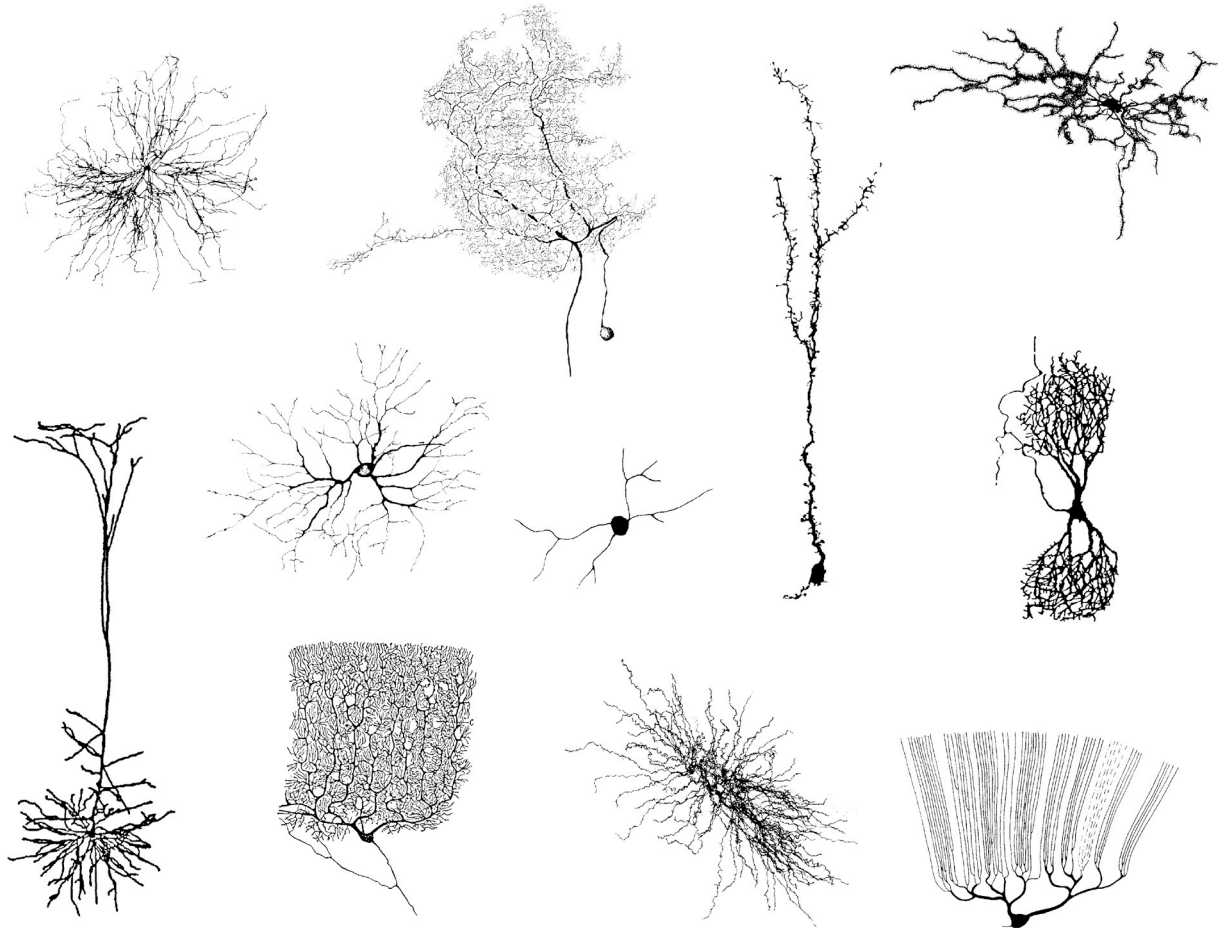


**Fig. 1.1.** Dendritic branching patterns of different types of neurons. Top row, left to right: alpha motoneuron in cat spinal cord (2.6 mm); spiking interneuron in mesothoracic ganglion of locust (540  $\mu\text{m}$ ); granule cell from mouse olfactory bulb (260  $\mu\text{m}$ ); spiny projection neuron in rat striatum (370  $\mu\text{m}$ ). Middle row, left to right: retinal ganglion cell in postnatal cat (390  $\mu\text{m}$ ); amacrine cell in the retina of larval tiger salamander (160  $\mu\text{m}$ ); neuron in the Nucleus of Burdach in human fetus. Bottom row, left to right: layer 5 pyramidal neuron in rat neocortex (1030  $\mu\text{m}$ ); Purkinje cell in human cerebellum; Relay neuron in rat ventrobasal thalamus (350  $\mu\text{m}$ ); Purkinje cell in mormyrid fish (420  $\mu\text{m}$ ). Adapted from Mel, 1994.

When synapses are located on extended dendritic trees, however, a single-compartment integrate-and-fire model of synaptic integration is too simple, even in the "passive" case when no nonlinearities due to voltage-dependent conductances are involved. Rall (1964) was the first to point out that spatially extended dendritic cables endow a neuron with mechanisms to distinguish different spatiotemporal patterns of synaptic input (Fig. 1.2).

The lowest threshold site for action potential initiation in neurons of the mammalian central nervous system is located in the axon, but action potentials back-propagate into the dendrites (Fig. 1.3; Stuart & Sakmann, 1994), providing a retrograde signal to the dendritic synapses that the axon has fired. Action potential backpropagation is possible because dendrites contain "active", voltage-dependent conductances (albeit at a lower density than the axon). These channels also enable

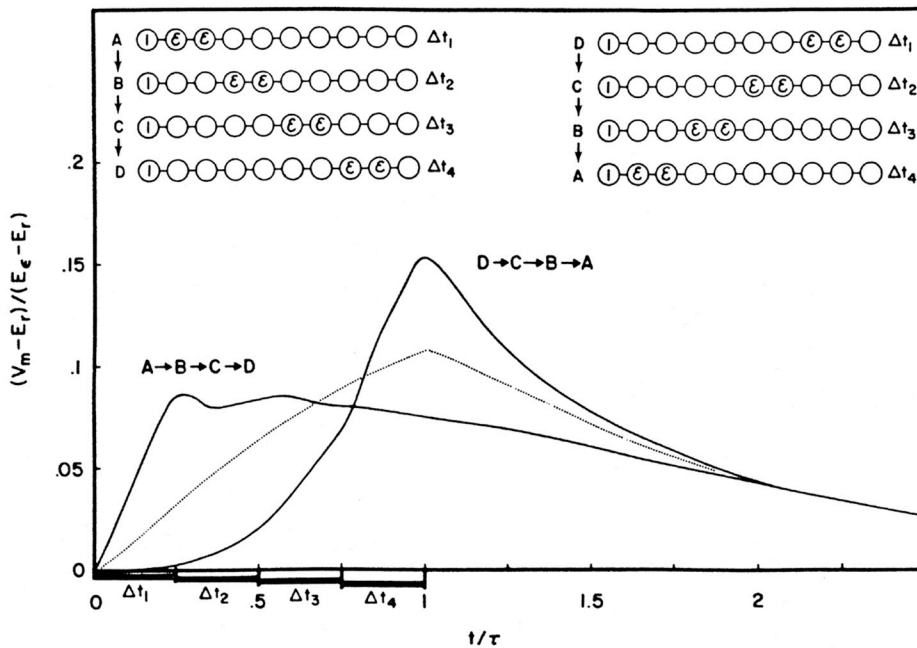


**Fig. 1.2.** The first compartmental model of a neuron. *Top*, structure of the compartmental model. In each of the instances the somatic compartment is shown on the left, and nine dendritic compartments to the right. *Bottom*, the amplitude and time course of the somatic membrane potential  $V_m$  (plotted in units of the synaptic driving force, i.e. the difference between the reversal potential of the synaptic conductance  $E_\varepsilon$  and the resting potential  $E_r$  of the neuron) depend on the temporal sequence in which synaptic conductances (denoted by  $\varepsilon$ ) at different locations on the dendrite are activated. Synaptic activation in the order  $A \rightarrow B \rightarrow C \rightarrow D$ , i.e. proximal synapses first and distal synapses last, results in a small but sustained somatic depolarization. The peak amplitude reached is not significantly higher than that in response to synaptic activation in configuration A alone. In contrast, activation in the order  $D \rightarrow C \rightarrow B \rightarrow A$ , i.e. distal synapses first and proximal synapses last, results in a larger but delayed somatic depolarization. Synaptic potentials activated in this order summate more synchronously and thus more effectively at the soma, because the delays in activation partly compensate the delays in the spread of the depolarization from the synaptic locations to the soma. The dotted line shows the effect of a synaptic conductance  $\varepsilon/4$  activated in each of eight compartments (2 through 9) for the period  $0 \leq t \leq \tau$ . See also section 1.2. Adapted from Rall, 1964.

dendrites to initiate their own spikes (Fig. 1.4; Helmchen et al., 1999). In contrast to linear (or subthreshold) synaptic integration, spikes are characterized by a voltage threshold beyond which excursions of the membrane potential become self-amplifying due to the recruitment of additional voltage-dependent conductances (Jack et al., 1983). Backpropagating action potentials can lower the threshold for initiation of dendritic spikes, thus providing nonlinear coupling mechanisms between several spike initiation zones in a neuron (Larkum et al., 1999b; Schaefer et al.,

2003b). The conditions for initiation of spikes in the dendrites are not the subject of this thesis, however.

Neurons are not identical particles. There is considerable diversity in the types of synapses between neurons, with different characteristics of transmission – different transmitters, different receptors, different amplitude and kinetics of the synaptic conductance, different degrees of variability and reliability, and different rules of short- and long-term synaptic plasticity. The exact purpose of this diversity is unclear, but since many parameters of synaptic transmission are actively regulated

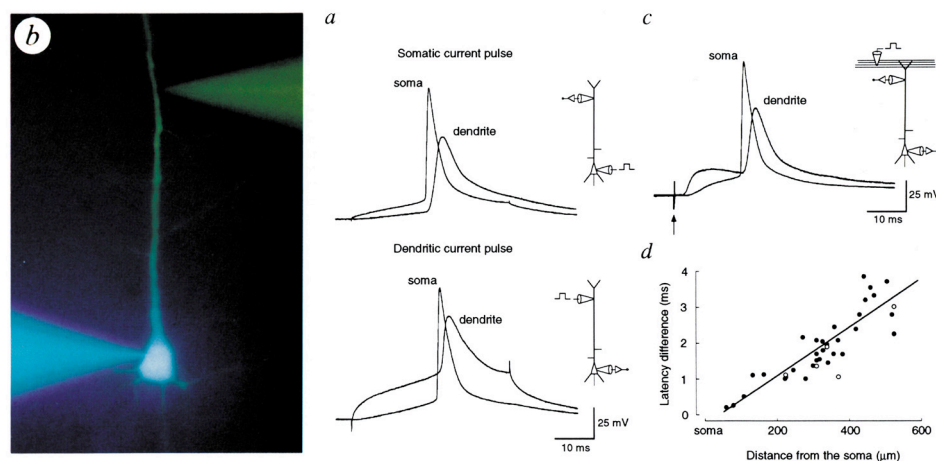


**Fig. 1.3.** Somatic action potentials back-propagate into the dendrites of layer 5 neocortical pyramidal neurons. *a*, simultaneous whole-cell recordings from the soma and apical dendrite (525  $\mu\text{m}$  from the soma) of a layer 5 pyramidal neuron *in vitro*. Action potentials were evoked by somatic (top, 150 pA) or dendritic (bottom, 300 pA) current injection. *b*, simultaneous filling of the same layer 5 pyramidal neuron from the dendrite and the soma with different fluorescent dyes: Cascade blue at the soma and Lucifer yellow in the dendrite (dendritic recording 190  $\mu\text{m}$  from the soma). *c*, action potentials initiated by distal synaptic stimulation in layer 1 (arrow); same cell and dendritic recording as in *a*. *d*, plot of the latency difference of the peak of somatic and dendritic action potentials at different distances from the soma. Action potentials were initiated by either somatic current pulses (filled symbols;  $n = 32$ ) or distal synaptic stimulation (open symbols;  $n = 5$ ). The linear fit has an inverse slope of  $0.15 \text{ m s}^{-1}$ . Adapted from Stuart & Sakmann, 1994.

by feedback loops over various time scales (Turrigiano & Nelson, 2004), and since small perturbations in the characteristics of synaptic transmission often have drastic effects (as can be observed in genetically modified animals – in many cases they suffer from epilepsy) it is likely that the diversity is required for normal brain function. Different types of neurons also exhibit different dendritic branching patterns (Fig. 1.1). Clearly, the different projection patterns of axons and dendrites determine which neurons can talk to which other neurons because they define the regions where axons and dendrites overlap and where synapses can be formed (Lübke et al., 2003). But beyond that, one might hypothesize that this diversity is not simply an epiphenomenon due to the need to wire up the cortex in a particular way, but that the consequences of the different branching patterns for the intrinsic properties of

different types of neurons, as well as variability among individual neurons of the same type are also important for the operation of the brain and, ultimately, the behaviour of the animal.

So what do neurons do? Can we look at any of the neurons in Fig. 1.1 and say what it does, or might do? In chapter 3 of this thesis I argue that the answer to this question is a cautious "yes". We can predict some aspects of dendritic function already from the dendritic branching pattern. Two complementary aspects which are relevant to information processing in neurons are highlighted by the following two questions: Firstly, how do neurons transform synaptic inputs to their dendrites into action potential output to their axon? And secondly, what are the functional compartments in dendritic trees?

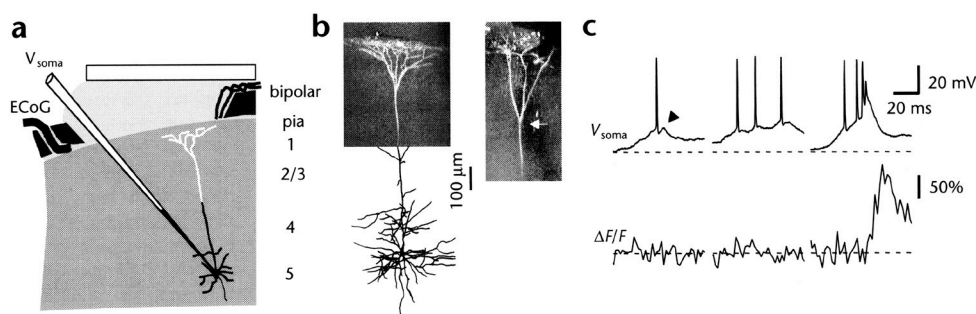


**Fig. 1.4.** All-or-none events triggered in the apical dendrite of layer 5 pyramidal neurons *in vivo*. *a*, experimental configuration for simultaneous somatic whole-cell recording and two-photon laser scanning microscopy. *b*, side projections of two apical tufts. The left layer 5 pyramidal neuron was recovered histologically, and a collage of the neurobiotin reconstruction (lower part) and the fluorescence image (upper part) is shown. The arrow indicates the location of the line-scans shown in *c*. *c*, single or multiple somatic sodium action potentials ( $V_{\text{soma}}$ ) did not evoke detectable  $[\text{Ca}^{2+}]$  transients ( $\Delta F/F$ ) near the main bifurcation of the right cell in *b* (left and middle). However, a spontaneous burst of somatic sodium action potentials superimposed on a slow depolarizing potential was accompanied by a large  $[\text{Ca}^{2+}]$  transient at the same location (right) indicating that a dendritic calcium spike was initiated. Adapted from Helmchen et al., 1999.

With time the answers to both questions have become more complicated. Starting from the integrate-and-fire neuron, many variants of single-compartment models have been developed, which make increasingly precise predictions of output spike trains given a time series of synaptic inputs. On the other end of the spectrum very detailed compartmental models of neurons have been constructed, with thousands of compartments, thousands of state variables and even more free parameters, which are tuned to reproduce a large range of experimental data (e.g. De Schutter & Bower, 1994). Models of this type are usually very complex, and it is often difficult to understand *why* a particular set of model parameters resulted in a good agreement between the predictions of the model and the experimental data, while a slightly different set of parameters specified a model that failed to do so.

Accordingly, it is difficult to reduce these complex models to a simpler, more tractable description that will predict for all possible spatiotemporal patterns of input how the output will look like (but see Poirazi et al., 2003). Models of intermediate complexity, such as conductance-based single-compartment models, two-compartment models (Pinsky & Rinzel, 1994), three-compartment models (Larkum et al., 2001) and equivalent cables (Fleishman et al., 1988; Clements & Redman, 1989; Ohme & Schierwagen, 1998; chapter 3), are therefore active areas of research.

Integrate-and-fire neurons are still the default devices in typical network models of the brain. Maybe this is indeed the appropriate abstraction of the function of a single neuron in the network 99% of the time. Maybe not. Perhaps it is justified to work with integrate-and-fire neurons at the network level as long as we do not have better working models of single neuron function which are not too complicated, not too inaccurate, and which have been validated by comparison with experiments *in vitro* and *in vivo* and with very detailed compartmental models.

To avoid this conceptual uncertainty in current network models, the present thesis follows the "bottom-up" approach. It assumes that we need to understand the signalling mechanisms at the molecular and cellular level if we really want to understand how behaviour at the next level emerges. The basic problem of the bottom-up approach towards the understanding of the brain is our current lack of knowledge about many (actually, most) of the details required for a reasonably accurate quantitative description even of a small part of the system, such as a single neuron. This is somewhat ironic, exactly because the firm conviction underlying the bottom-up approach is that details do matter, and also because a large amount of data is already described in the literature – but experience shows that whenever the value of a particular quantity is needed in order to construct a quantitative model of a certain aspect of neuronal function, chances are that no useful information is available on it. Typically, there are several reasons for this. Either there are no data available at all on this particular quantity, or the measurements were too indirect, not sufficiently accurate, not done under the right conditions, or the results are not presented in a useful format.

A quantitative description of the input-output relationship of a neuron depends on parameters such as the amplitude and kinetics of the synaptic conductance, the passive membrane parameters, and also on the effects of active conductances. Many of the underlying parameters are difficult to measure experimentally in cortical neurons due to the electrical cable structure of their spatially distributed, highly branched, thin dendrites. New methods are needed to obtain more accurate measurements of these parameters, and the strategy for the present thesis is to develop closely integrated, combined experimental and modelling methods to address or circumvent the experimental difficulties.



This introduction continues with two sections describing the theoretical background of the new methods, cable theory (in section 1.1), and the tools used to apply and to test the new techniques: compartmental models (in section 1.2). Chapter 2 presents a method for unbiased measurements of the kinetics of synaptic conductances located in the dendrites of a neuron, remote from the recording site at the cell body. Chapter 3 shows how compartmental models of neurons including active, voltage-dependent conductances can be used to examine the link between form and function of neurons, focusing on the backpropagation and forward propagation of action potentials in the dendrites. The thesis concludes with a comprehensive discussion.

## 1.1 The cable equation

### 1.1.1 Main assumptions

The dendrites and axons of neurons are cable-like structures, consisting of a conducting core and a surface membrane which can be represented as a capacitance and a resistance in parallel (Jack et al., 1983). The core conductor – the intracellular medium of the neuron – is an electrolyte solution whose electrical conductivity is determined by the concentration of mobile intracellular ions such as  $K^+$  and  $Cl^-$  and by the excluded volume taken up by intracellular organelles such as mitochondria. Typical values for the specific resistivity  $R_i$  of the intracellular medium in neurons of the mammalian central nervous system range from 70 to 150  $\Omega$  cm (for discussion see Roth & Häusser, 2001). The capacitance per unit area of the cell membrane,  $C_m$ , is determined by the effective thickness and the effective dielectric constant of the lipid bilayer, both of which are not exactly known since the protein content of the membrane is variable. However, direct measurements of  $C_m$  in neurons typically yield values around 1  $\mu F$   $cm^{-2}$  (Gentet et al., 2000). Among the proteins embedded in the lipid bilayer are various types of ion channels whose density and conductance – which can be voltage-dependent, as described in section 1.2.2 below – determine the membrane resistance. Typical values of the specific membrane resistance  $R_m$  near the resting membrane potential  $V_{rest}$  (about  $-70$  mV; measured as intracellular potential minus extracellular potential) depend mostly on the density of voltage-independent (leak) ion channels in the neuron and range from 10 to 100  $k\Omega$   $cm^2$ . As long as  $R_m$  is not voltage-dependent, we speak of a "passive" cable; if there is a significant voltage dependence of the specific membrane resistance (see section 1.2.2), the cable is called "active".

Locally, between branch points, the geometry of the cable can be approximated by a cylinder. This cylinder is sufficiently long and thin, and the membrane resistance is large compared to the intracellular resistivity such that the dominant fraction of the current inside the dendrite flows parallel to its longitudinal axis. Thus, we do not need to solve for voltage in three dimensions: the problem can be reduced to a description of voltage along a single spatial dimension  $x$ . We also assume that the intracellular resistivity is Ohmic since any capacitive effects inside the cytoplasm can be ignored on the millisecond time scale, and inductive effects can be completely neglected (Jack et al., 1983). This leaves one major approximation which we can safely make for our purposes here, but which may not always be appropriate when studying the intact brain *in vivo*: we assume that the extracellular medium has a negligible resistivity and is virtually isopotential.

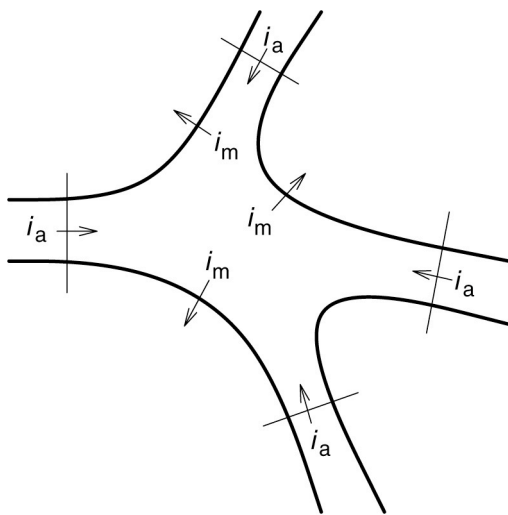


**Fig. 1.5.** Cross-section of dendritic processes meeting at a branch point.  $i_a$ , axial current;  $i_m$ , membrane current (see section 1.1.2). The net current entering a given region must be zero according to Kirchhoff's law of current conservation.

### 1.1.2 The linear cable equation

To derive the cable equation it is convenient to reexpress  $R_i$ ,  $C_m$  and  $R_m$  as quantities per unit length of the cable, i.e.

$$r_a = \frac{4R_i}{\pi d^2} \quad (1.1)$$

is the axial resistance in units of  $\Omega \text{ cm}^{-1}$ ,

$$r_m = \frac{R_m}{\pi d} \quad (1.2)$$

is the membrane resistance in units of  $\Omega \text{ cm}$  and

$$c_m = C_m \cdot \pi d \quad (1.3)$$

is the membrane capacitance in units of  $\mu\text{F cm}^{-1}$ , where  $d$  is the diameter of the cable. According to Ohm's law, the spatial gradient of the membrane potential is proportional to both the axial resistance per unit length and the axial current,

$$\frac{\partial V(x,t)}{\partial x} = -r_a \cdot i_a(x,t). \quad (1.4)$$

On the other hand, Kirchhoff's law of current conservation states that any local change in the axial current is only possible if there is a nonzero membrane current per unit length,

$$i_m(x,t) = -\frac{\partial i_a(x,t)}{\partial x}, \quad (1.5)$$

and inserting the spatial derivative of Eq. 1.4 into Eq. 1.5 yields

$$i_m(x,t) = \frac{1}{r_a} \frac{\partial^2 V(x,t)}{\partial x^2}. \quad (1.6)$$

We have arrived at a second-order ordinary differential equation relating the profile of the membrane voltage and the membrane current, assuming an Ohmic intracellular cytoplasm. Now we need to specify the different contributions to the membrane current – an ohmic contribution due to the membrane resistance, a capacitive current due to the membrane capacitance, and possible external currents,

$$i_m(x,t) = \frac{V(x,t) - V_{\text{rest}}}{r_m} + c_m \frac{\partial V(x,t)}{\partial t} - i_{\text{pip}}(x,t), \quad (1.7)$$

where  $i_{\text{pip}}$  is a current injected into the cable, in parallel to the membrane current  $i_m$ , via an electrode with access to the intracellular medium, for example a patch pipette in the whole-cell recording configuration. By combining Eq. 1.6 and Eq. 1.7 and multiplying with  $r_m$  we obtain

$$\lambda^2 \frac{\partial^2 V(x,t)}{\partial x^2} = (V(x,t) - V_{\text{rest}}) + \tau_m \frac{\partial V(x,t)}{\partial t} - r_m i_{\text{pip}}(x,t), \quad (1.8)$$

where  $\lambda = \sqrt{\frac{r_m}{r_a}}$  is the steady-state space constant and  $\tau_m = r_m c_m$  is the membrane time constant. Eq. 1.8 is the linear cable equation, a partial differential equation of the parabolic type, similar to the diffusion equation.

### 1.1.3 Steady-state solution in an infinite cable

Analytical solutions of the linear cable equation have been obtained for a number of situations (Jack et al., 1983; Major et al., 1993). Here we give only the solution for an infinite cable in the steady-state, where the cable equation simplifies to

$$\lambda^2 \frac{\partial^2 V(x,t)}{\partial x^2} = (V(x,t) - V_{\text{rest}}) - r_m i_{\text{pip}}(x). \quad (1.9)$$

For a current injection at  $x = 0$ , represented by  $i_{\text{pip}}(x) = I \cdot \delta(x)$  where  $\delta(x)$  is the Dirac delta distribution, Eq. 1.9 has the solution

$$V(x) = V_{\text{rest}} + V_0 e^{-|x|/\lambda} \quad (1.10)$$

where  $V_0 = \frac{I \cdot r_m}{2\lambda}$  (or  $V_0 = \frac{I \cdot r_m}{\lambda}$  for a semi-infinite cable). Thus the input resistance of the semi-infinite cable is  $R_{\text{in}} = \frac{V_0}{I} = \frac{r_m}{\lambda} = \sqrt{r_a r_m} = \sqrt{R_i R_m} \cdot \frac{2}{\pi d^{3/2}}$ , a result which we will revisit in chapter 3.

## 1.2 Compartmental models

### 1.2.1 Introduction

Analytical solutions become more complicated when the diameter of the cable changes or when multiple cables are connected at branch points, as is the case in real dendritic trees. The level of difficulty jumps especially when the cables become active and  $r_m$  depends on voltage (Jack et al., 1983). In these cases it is convenient

to solve Eq. 1.8 numerically. Spatial discretization (Fig. 1.6) gives rise to a family of ordinary differential equations of the form

$$c_j \frac{dV_j}{dt} + I_{ion_j} = \sum_k \frac{V_k - V_j}{r_{jk}} \quad (1.11)$$

which again represent Kirchhoff's law of current conservation: the membrane current leaving compartment  $j$  must be equal to the sum of axial currents entering this compartment from all connected compartments  $k$ . Compartmental models of neurons were first used by Rall (1964; see Fig. 1.2).

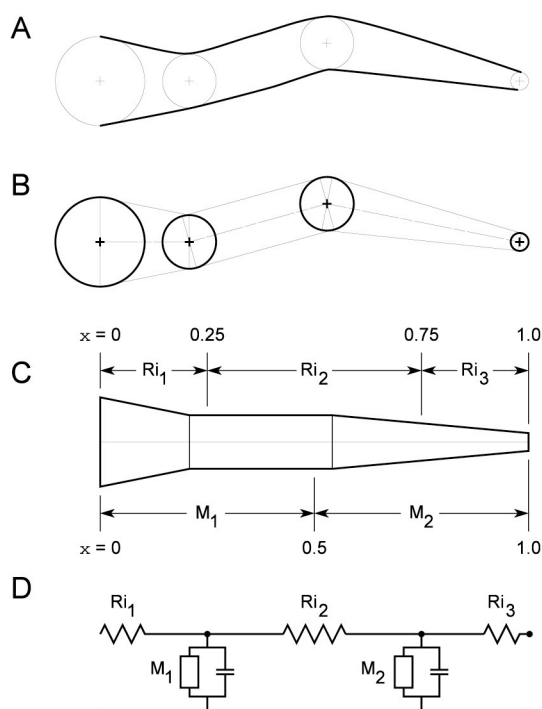


**Fig. 1.6.** A, schematic representation of an unbranched section of a dendrite. Computer-aided light-microscopic reconstruction of neurons provides lists of local coordinates (crosses) and diameters (circles) of neurites. B, as a first step towards the construction of a compartmental model based on a morphological reconstruction of a dendrite, each adjacent pair of diameter measurements (circles) forms the parallel faces of a truncated cone. C, bends are straightened out since any bend angles are ignored when constructing the one-dimensional cable equation. D, electrical equivalent circuit with two compartments.  $R_i$  refers to the axial resistors and  $M$  to the membrane areas associated with the left and right compartment.  $x$  is a relative spatial coordinate with values ranging from 0 (left end of section) to 1 (right end of section). Adapted from Hines & Carnevale, 1997.

## 1.2.2 The Hodgkin–Huxley model

The classical description of excitability in neurons is the model of Hodgkin & Huxley (1952). It is a phenomenological model in which the ionic transmembrane current  $I_{ion}$  in Eq. 1.11 consists of a component mediated by voltage-dependent  $\text{Na}^+$  channels,  $I_{\text{Na}}$ , a component mediated by voltage-dependent  $\text{K}^+$  channels,  $I_{\text{K}}$ , and a leak current mediated by a voltage-independent leak conductance (see also Fig. 1.7)

$$I_{ion} = I_{\text{Na}} + I_{\text{K}} + I_{\text{leak}} \quad (1.12)$$

Each of these currents is the product of a maximal conductance, a gating variable (which is effectively constant in the case of the leak) and the driving force (the

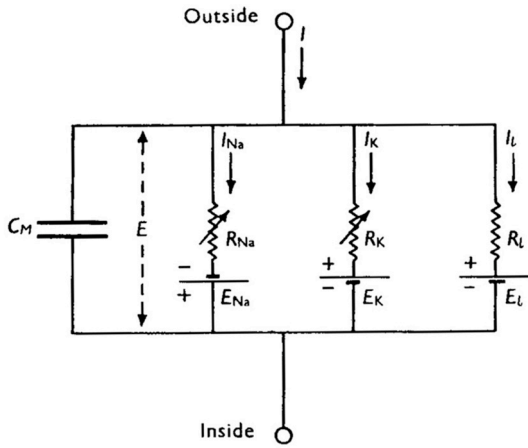


**Fig. 1.7.** Equivalent circuit for the Hodgkin-Huxley model in a single compartment. The outside and inside of the cell membrane are connected by a capacitor representing the membrane capacitance, two voltage-dependent resistors and batteries representing the reversal potential for the sodium and potassium conductances, respectively, and a constant resistor and battery representing the leak conductance and its reversal potential. From Hodgkin & Huxley, 1952.

membrane potential minus the reversal potential given by the Nernst equation). The  $K^+$  current is given by

$$I_K = \bar{g}_K n^4 (V - E_K), \quad (1.13)$$

where  $\bar{g}_K$  is the maximal potassium conductance,  $n$  is the gating variable ( $n^4$  implying four independent gates per channel) and  $V - E_K$  is the driving force for potassium ions. Similarly, the  $Na^+$  current is given by

$$I_{Na} = \bar{g}_{Na} m^3 h (V - E_{Na}), \quad (1.14)$$

where  $m$  and  $h$  are two gating variables for the activation and inactivation of the sodium channels, respectively. The voltage- and time-dependence of these gating variables is governed by the following differential equations

$$\begin{aligned} \frac{dn}{dt} &= \alpha_n(V)(1-n) - \beta_n(V)n \\ \frac{dm}{dt} &= \alpha_m(V)(1-m) - \beta_m(V)m \\ \frac{dh}{dt} &= \alpha_h(V)(1-h) - \beta_h(V)h, \end{aligned} \quad (1.15)$$

where the rate constants  $\alpha$  and  $\beta$  have the following voltage dependence in the original model of Hodgkin & Huxley (1952)

$$\begin{aligned}
\alpha_n(V) &= \frac{10 \text{ mV} - V}{100 \text{ mV} \cdot \text{ms} (e^{(10 \text{ mV} - V)/(10 \text{ mV})} - 1)} \\
\beta_n(V) &= 0.125 \text{ ms}^{-1} e^{-V/(80 \text{ mV})} \\
\alpha_m(V) &= \frac{25 \text{ mV} - V}{10 \text{ mV} \cdot \text{ms} (e^{(25 \text{ mV} - V)/(10 \text{ mV})} - 1)} \\
\beta_m(V) &= 4 \text{ ms}^{-1} e^{-V/(18 \text{ mV})} \\
\alpha_h(V) &= 0.07 \text{ ms}^{-1} e^{-V/(20 \text{ mV})} \\
\beta_h(V) &= \frac{1 \text{ ms}^{-1}}{e^{(30 \text{ mV} - V)/(10 \text{ mV})} + 1}.
\end{aligned} \tag{1.16}$$

These parameters describe the voltage-dependence and kinetics of the Na<sup>+</sup> and K<sup>+</sup> currents in the squid giant axon, which was the model system studied by Hodgkin & Huxley. The voltage-gated ion channels found in neurons of the mammalian central nervous system are related to those in the squid, but do differ in their detailed properties, not least because of the different body temperature and the different ionic composition of the extracellular medium compared to sea water. Thus, chapter 3 of this thesis uses a Hodgkin–Huxley-type model of neuronal excitability with the same structure as the original Hodgkin & Huxley (1952) model but slightly different parameters describing action potential initiation and propagation in neocortical neurons (Mainen et al., 1995; Mainen & Sejnowski, 1996).

### 1.2.3 The NEURON simulation environment

NEURON, a free software package written by Michael Hines (Hines & Carnevale, 1997), has become the standard tool for simulations of compartmental models of neurons. NEURON uses an efficient numbering scheme for the  $n$  compartments representing a branched cable such that the connectivity matrix can be inverted in  $O(n)$  steps. Thus, implicit methods for the solution of the discretized cable equation can be applied in an efficient manner. The default method is the backward Euler method, which is stable for large time steps and robust in practice. NEURON also provides facilities for the construction of compartmental models based on detailed morphological reconstructions of neurons (Fig. 1.8).

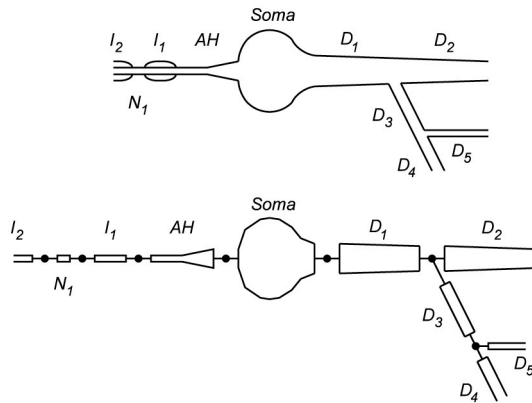


**Fig. 1.8.** *Top*, morphological reconstruction of a neuron with a cell body (Soma), dendrites (D), axon hillock (AH), and an axon consisting of myelinated internodes (I) and nodes of Ranvier (N). *Bottom*, conceptual representation of the same cell in NEURON as a set of sections connected at branch points. Each section can be subdivided into several compartments (called segments) as shown in Fig. 1.6.

Different parts of the neuronal morphology may be endowed with different membrane properties in NEURON. For example,  $\text{Na}^+$  and  $\text{K}^+$  channels are often placed at high density in the nodes of Ranvier and the axon hillock (see also Fig. 3.2), and low membrane capacitance is used in the myelinated internodes.



## 2 Estimating the time course of the synaptic conductance under conditions of inadequate space clamp

### 2.1 Introduction

Knowledge of the time course of the synaptic conductance is of fundamental importance to our understanding of synaptic transmission. The kinetics of the synaptic conductance influences neuronal function in a variety of ways, from shaping the resulting synaptic potential and influencing the time window for synaptic integration, to determining the charge associated with the synaptic current (particularly relevant when a significant fraction of the current is carried by ions with second-messenger effects, such as  $\text{Ca}^{2+}$ ). Furthermore, comparing the synaptic conductance time course to receptor channel kinetics can provide valuable information about the signal cascade underlying synaptic transmission.

Synaptic conductance is conventionally measured by recording the synaptic current with somatic voltage clamp. In cells where all synapses are electrotonically close to or at the soma, such as cerebellar granule cells (Silver et al., 1992, 1995), neuroendocrine cells (Schneggenburger & Konnerth, 1992; Borst et al., 1994), unipolar brush cells (Rossi et al., 1995) or neurons in the auditory pathway (Forsythe & Barnes-Davies, 1993; Zhang & Trussell, 1994; Borst et al., 1995), this method can give a reliable estimate of the conductance time course. Alternatively, one can select for somatic synapses on the basis of cable model predictions (Finkel & Redman, 1983; Nelson et al., 1986). However, in most neurons the large majority of synapses are located at a considerable electrotonic distance from the soma, and therefore somatic voltage clamp of these synapses is associated with substantial attenuation and distortion of the synaptic current (Rall, 1967; Johnston & Brown, 1983; Rall & Segev, 1985; Major, 1993; Spruston et al., 1993; Roth & Häusser, 2001). This problem has proved to be rather intractable, and although several solutions have been proposed before (see section 2.4.1), none are completely satisfactory.

Pearce (1993) introduced an experimental technique which uses somatic voltage jumps at various times during the synaptic conductance to determine how long after the onset of the synaptic current the synaptic conductance is still active. The principle of the technique is that a voltage jump which increases the synaptic driving force will only recover additional synaptic charge if the jump is made while the conductance is still active. The technique was used to show that the GABAergic synaptic conductance generated by activation of distal synapses in hippocampal CA1

neurons has a prominent slow component; however, a quantitative determination of the time course of the conductance was not made. The same technique was subsequently applied to excitatory synapses in various neuronal types, also to demonstrate that the synaptic conductance at these synapses has a prolonged component (Barbour et al., 1994; Mennerick & Zorumski, 1995; Rossi et al., 1995; Kirson & Yaari, 1996).

Here I show using simulations in a variety of reconstructed model neurons that by measuring the time course of recovered *charge* this experimental technique can be used to determine the decay time course of the synaptic conductance with a high degree of accuracy. A simple analytical function providing a quantitative description of the results is presented, and limitations and potential applications of the method are explored.

## 2.2 Methods

All simulations were carried out using NEURON (Hines & Carnevale, 1997) running on SUN Sparcstations (Sun Microsystems, Mountain View, CA, USA). The integration time step was  $10 \mu\text{s}$ . The synaptic conductance consisted of a sum of two or three exponentials, one for the rise (always 0.2 ms, unless otherwise indicated), and one or two for the decay. A "brief pulse" synaptic conductance was simulated using a 1 nS conductance with duration of 0.1 ms. Except for the equivalent cylinder simulations and the simulations shown in Fig. 2.10, synaptic contacts were placed at the head of explicitly modeled spines. The series resistance of the recording pipette was always  $0.5 \text{ M}\Omega$  (except for the simulation in Fig. 2.9A–C), which is achievable in experiments using the neuronal types shown here (e.g.  $5 \text{ M}\Omega$  compensated by 90%). Unless otherwise indicated, the decay time constant of synaptic currents recorded at the soma was fitted using a single exponential function, starting at the time point where the current had decayed to about 90% of the peak amplitude.

### 2.2.1 Equivalent cylinder model

The geometry used in the equivalent cylinder simulation was as follows (see Fig. 2.1): soma  $10 \mu\text{m}$  long,  $10 \mu\text{m}$  diameter, 10 segments; dendrite  $500 \mu\text{m}$  long,  $1.2 \mu\text{m}$  diameter, 100 segments. Electrical parameters were:  $R_i = 150 \Omega \text{ cm}$ ,  $R_m = 50 \text{ k}\Omega \text{ cm}^2$ ,  $C_m = 1.0 \mu\text{F cm}^{-2}$ , giving an electrotonic length of the dendrite of  $L = 0.5$ . The passive reversal potential was  $-65 \text{ mV}$ .



**Fig. 2.1.** Equivalent cylinder model (soma not to scale), with electrotonic length  $L = 0.5$ . The locations of three synapses on the cable (electrotonic location  $X = 0, 0.15$  and  $0.5$ ) are indicated by arrows.

### 2.2.2 CA3 pyramidal cell model

The CA3 pyramidal cell model was based on cell CA3\_15 in Major et al. (1994), which is from a 19-day-old rat. The morphology was converted from the

native format to that of NEURON using a program written in Mathematica (Wolfram Research, Champaign, IL, USA). The electrotonic length of each segment was  $< 0.01$ . The electrical parameters were  $R_i = 250 \Omega \text{ cm}$ ,  $R_m = 180 \text{ k}\Omega \text{ cm}^2$ ,  $C_m = 0.66 \mu\text{F cm}^{-2}$  (Major et al., 1994), with a passive reversal potential of  $-65 \text{ mV}$ . Spine corrections were carried out as described by Major et al. (1994), and the axon was not included in the simulations. The spine at the excitatory synaptic contact had a neck length of  $0.66 \mu\text{m}$ , a neck diameter of  $0.2 \mu\text{m}$ , a head length of  $0.5 \mu\text{m}$ , and a head diameter of  $0.45 \mu\text{m}$ .

### 2.2.3 Neocortical pyramidal cell model

The morphology of the layer 5 pyramidal cell was taken from Markram et al. (1997) and comes from a postnatal day 14 rat (same neuron as shown in red in Figure 13 of that paper). The electrotonic length of each segment was  $< 0.02$ . The values for passive cable properties were  $R_i = 150 \Omega \text{ cm}$ ,  $R_m = 30 \text{ k}\Omega \text{ cm}^2$ ,  $C_m = 0.75 \mu\text{F cm}^{-2}$ , and the passive reversal potential was set to  $-70 \text{ mV}$  (Mainen & Sejnowski, 1996). The measured dendritic membrane area was doubled to account for spines. The axon was included, but axon collaterals were omitted. The neck length of the explicitly modeled spines was  $1.0 \mu\text{m}$ , neck diameter was  $0.35 \mu\text{m}$ , and head length and diameter were both  $0.7 \mu\text{m}$  (Peters & Kaiserman-Abramof, 1970).

Active conductances were added to the model as described in Mainen & Sejnowski (1996), based on the parameters in their original NEURON files (available at <http://www.cnl.salk.edu/CNL/simulations.html>). Two changes were made with respect to the original files of Mainen & Sejnowski: 1) the reversal potential for  $\text{Ca}^{2+}$  was not constant at  $+140 \text{ mV}$ , but updated according to the Nernst equation assuming  $[\text{Ca}^{2+}]_o = 2 \text{ mM}$ ; 2) the time step was  $10 \mu\text{s}$  instead of  $25 \mu\text{s}$ .

## 2.3 Results

### 2.3.1 Attenuation and filtering of synaptic currents under poor space-clamp conditions

The nature of the problem faced when attempting to voltage clamp dendritic synaptic currents via a somatic electrode is illustrated in Fig. 2.2 using the simple equivalent cylinder model shown in Fig. 2.1. There are two closely related components of inadequate space clamp that must be considered: attenuation of the signal along the cable, and the reduction in driving force at the synapse caused by local depolarization or hyperpolarization (also known as "voltage escape"). The outcome of these two effects is that the current recorded at the soma from synapses

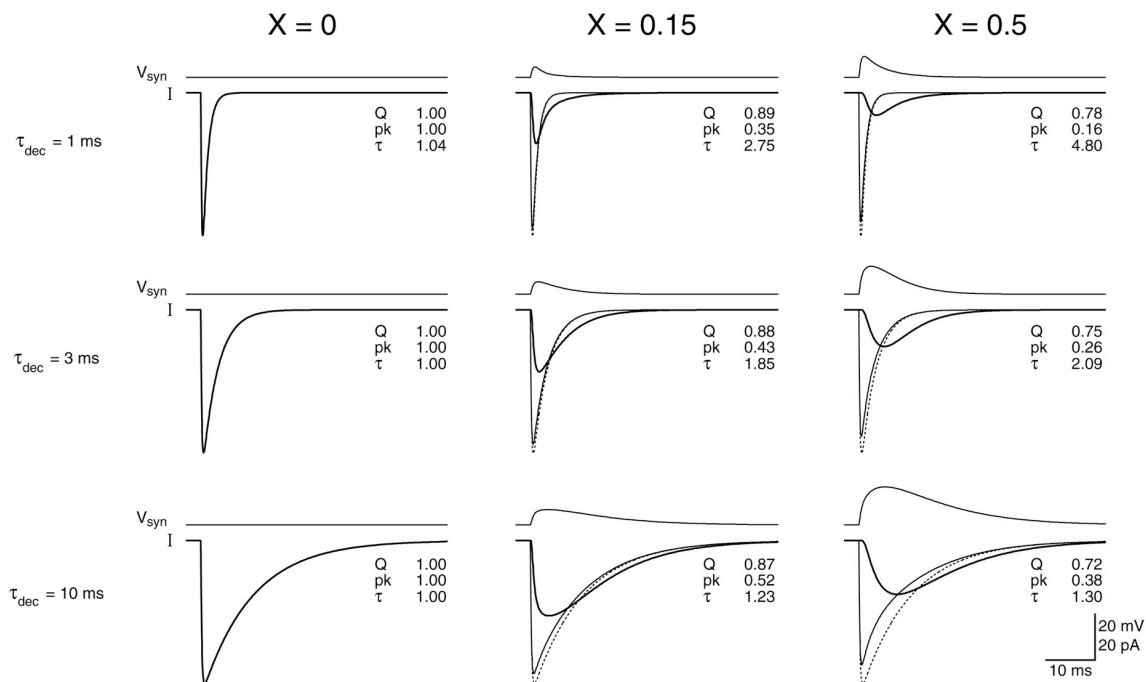


**Fig. 2.2.** Space-clamp errors affecting the measurement of dendritic synaptic conductances. All traces from the same equivalent cylinder shown schematically in Fig. 2.1. The peak synaptic conductance was 1 nS in each case, consisting of the sum of a rising ( $\tau = 0.2$  ms) and a decaying ( $\tau =$  either 1, 3 or 10 ms) exponential. For each panel the voltage at the synaptic location is shown as the top trace. The lower traces show the current recorded at the soma (thick line), the current actually flowing at the synapse (thin line), and the synaptic current expected under perfect voltage clamp conditions (dashed line). The figures at the right of each panel show the relative magnitude of the peak ("pk"), the decay time constant (" $\tau$ ") and the charge ("Q") of the somatic current versus the perfectly clamped synaptic current. The scale bar at the bottom right of the figure applies to all panels.

located on the dendrites is a substantially filtered version of the synaptic current expected under perfect clamp conditions, with the risetime, peak and decay being subject to considerable distortion, dependent on the electrotonic distance of the

synapse from the soma and the kinetics of the conductance. These features have been previously described in detail (Johnston & Brown, 1983; Rall & Segev, 1985; Major, 1993; Major et al., 1993; Spruston et al., 1993), but there are several aspects of particular relevance to the method which deserve special emphasis. First, the current flowing at the synapse during somatic voltage clamp is not identical to the current which would be flowing during perfect clamp of the synapse. This difference is attributable to the voltage escape at the synapse, which reduces the driving force of the synaptic current and distorts its shape. Second, for a given location and peak conductance the voltage escape, and thus the distortion of the synaptic current, is greatest for the synaptic conductances with the slowest kinetics, since they continue to charge the membrane capacitance for a longer period of time. The magnitude of this effect on the current recorded at the soma will be mitigated by the fact that slow conductances suffer less attenuation by the cable, since attenuation is frequency-dependent in a passive system (Rall, 1967; Jack et al., 1983; Spruston et al., 1994). Third, while the kinetics and the peak of the synaptic current suffer the most distortion, the attenuation of synaptic charge is much less severe. Furthermore, the attenuation of charge at a given location is relatively independent of the kinetics of the current: in these simulations, there was <10% difference in the recovered charge for conductances with different kinetics even for the most distal synapses. This residual difference is attributable to the greater voltage escape caused by slower conductances: when the voltage escape converges towards zero, the attenuation of synaptic charge becomes independent of the kinetics of the synaptic conductance (Rall & Segev, 1985; Major et al., 1993).

The voltage jump method described in this chapter circumvents the filtering of the synaptic current by the cable and provides a reliable estimate of the synaptic conductance time course for even the most electrotonically distal synapses. The method is particularly concerned with (and is most effective for) fast synaptic conductances, which suffer the most severe distortions under conditions of inadequate space clamp.

### **2.3.2 Measuring charge recovery**

The experimental procedure for recovering synaptic charge, following the method introduced by Pearce (1993), is demonstrated using a simple equivalent cylinder simulation in Fig. 2.3. According to this procedure the somatic voltage is held at the apparent synaptic reversal potential and a hyperpolarizing voltage jump is made, providing a driving force to generate synaptic current. The voltage jump is repeated in the presence and absence of synaptic activation and the resulting

somatic currents are subtracted, thus eliminating the capacitive transient which accompanies the voltage jump. This procedure gives a residual synaptic current with a time course and amplitude which depends on the relative time of the jump and the onset of the synaptic conductance (see Fig. 2.4A). If the jump occurs sufficiently long before the onset of the conductance, then the residual current will approach identity

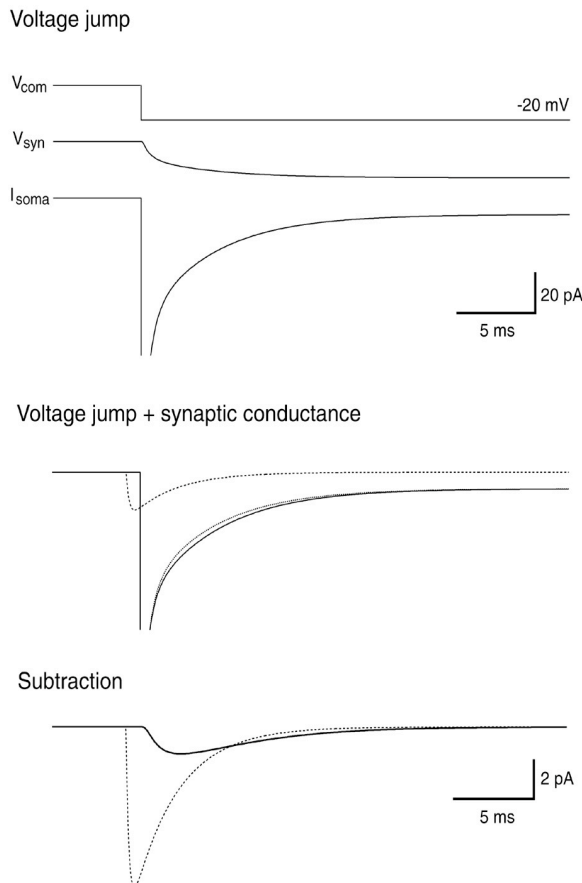


**Fig. 2.3.** Experimental protocol for measuring charge recovery. Same equivalent cylinder as in Fig. 2.2; synapse at  $X = 0.15$ , peak conductance 1 nS, rise and decay time constants 0.2 and 3.0 ms respectively. Top panel,  $-20$  mV voltage jump applied at the soma via the somatic electrode. The somatic holding potential is set to 4.10 mV, making the voltage at the synapse equal to the reversal potential (0 mV). The somatic voltage clamp command is shown in the top trace, the voltage at the synapse is shown in the second trace, and the (truncated) somatic clamp current is shown in the lower trace. Second panel, the synaptic conductance is activated 1 ms before the same voltage jump. The time course of the synaptic conductance is shown by the dashed line, with the amplitude equal to that of the perfectly clamped synaptic current. The somatic clamp current in the presence (solid line) and absence (dotted line) of the synaptic conductance is shown. Bottom panel, residual synaptic current (thick trace) following subtraction of somatic clamp current under the two conditions. The synaptic current expected under perfect voltage clamp at a constant holding potential of  $-20$  mV is superimposed as a dashed line.

with the synaptic current recorded at that potential under steady-state conditions. On the other hand, if the jump occurs a sufficiently long time after the onset of the synaptic conductance then it will eventually recover no current at all, since the synaptic conductance will have terminated. The current resulting from each jump therefore results from an interaction between the time course of the increase in driving force at the synapse and the kinetics of the conductance itself.

The synaptic charge associated with each residual current is plotted against the time of the respective jump in Fig. 2.4B. The resulting "charge recovery curve" has a sigmoidal shape consisting of an exponential "onset" and "offset" with a transition around 0 ms, i.e. at the beginning of the synaptic conductance. This is made more clear when the charge recovery curve is differentiated with respect to the time of the somatic voltage jump (Fig. 2.4C), revealing a sharp peak near 0 ms, with

an exponential rolloff on either side. The determinants of the two components of the curve will be examined in the following section.

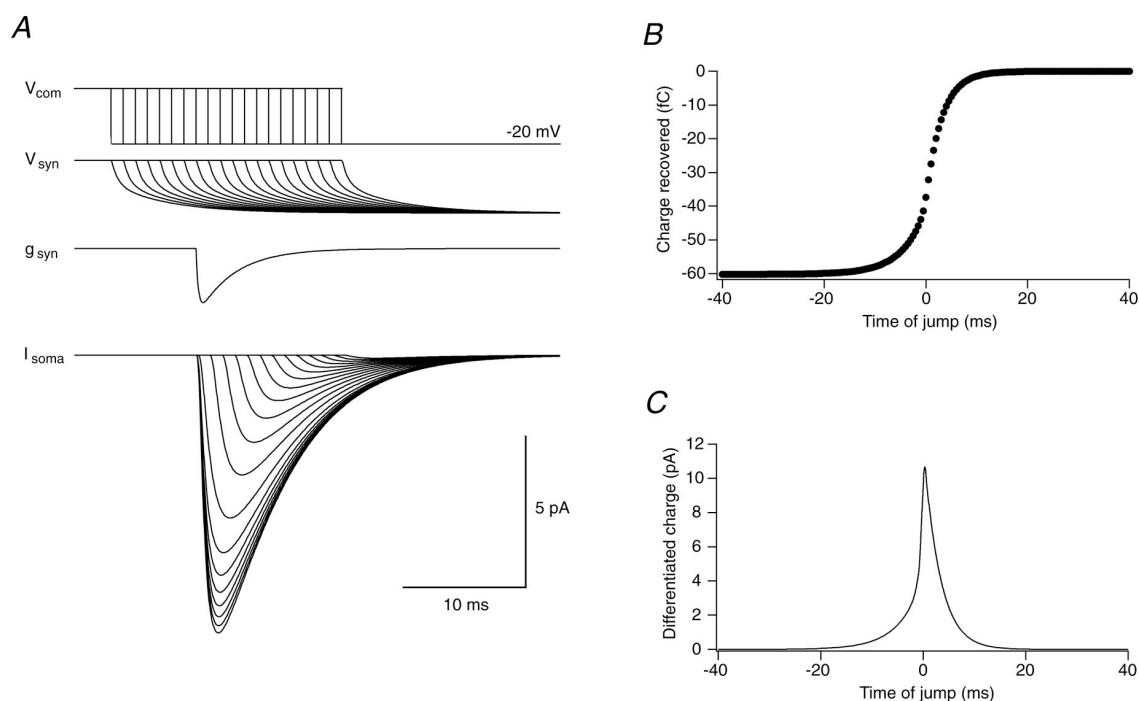


**Fig. 2.4.** Charge recovery depends on the time of the voltage jump. Same conditions as in Fig. 2.3. *A*, 20 superimposed sweeps of somatic voltage jumps ( $V_{com}$ , top traces) at different times relative to the onset of the synaptic conductance. The interval between jump traces is 1 ms; the earliest jump is 7 ms before the onset of the synaptic conductance, and the latest is 12 ms after onset of the conductance. Also shown are the voltage at the synapse ( $V_{syn}$ ), the time course of the synaptic conductance ( $g_{syn}$ ), and the "recovered" somatic currents ( $I_{soma}$ ) obtained by subtracting the somatic clamp current in the presence and absence of the synaptic current for each jump. *B*, plot of the charge associated with the "recovered" somatic synaptic currents ( $I_{soma}$ ) versus time of the somatic voltage jump; 0.5 ms jump intervals. *C*, differentiation (with respect to time of jump) of the charge recovery curve shown in *B*. A cubic spline interpolation was performed before the differentiation.

### 2.3.3 Charge recovery after the onset of the synaptic conductance is determined by the conductance time course

Figure 2.5 shows several charge recovery curves from a synapse at the same location as in Figs. 2.3 and 2.4 with a range of kinetics for the synaptic conductance. It is clear from the Figure that the portion of the charge recovery curve which follows the onset of the synaptic conductance is determined by the decay time constant of the synaptic conductance: when the decay of the conductance is effectively instantaneous, as with the brief (0.1 ms) pulse, then the charge recovered after  $t = 0$  ms is effectively zero. For the more realistic synaptic conductances in Fig. 2.5*B–D*, the decay of the charge recovery closely matches the actual decay time



course of the synaptic conductance. This finding holds for the condition  $\tau_{\text{rise}} \ll \tau_{\text{decay}}$  of the conductance, as is true for most synaptic conductances found to date. Note that the interval chosen to fit the recovery curve in order to extract the synaptic

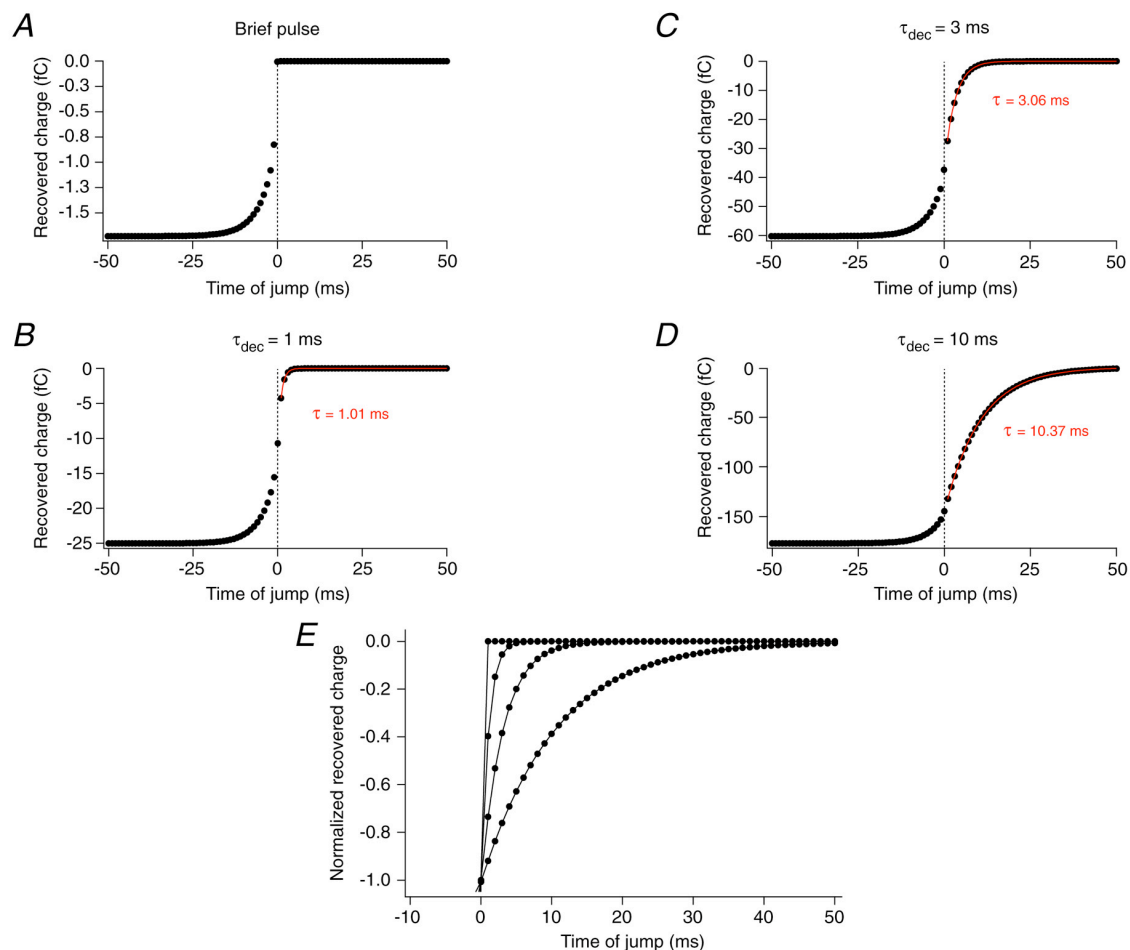


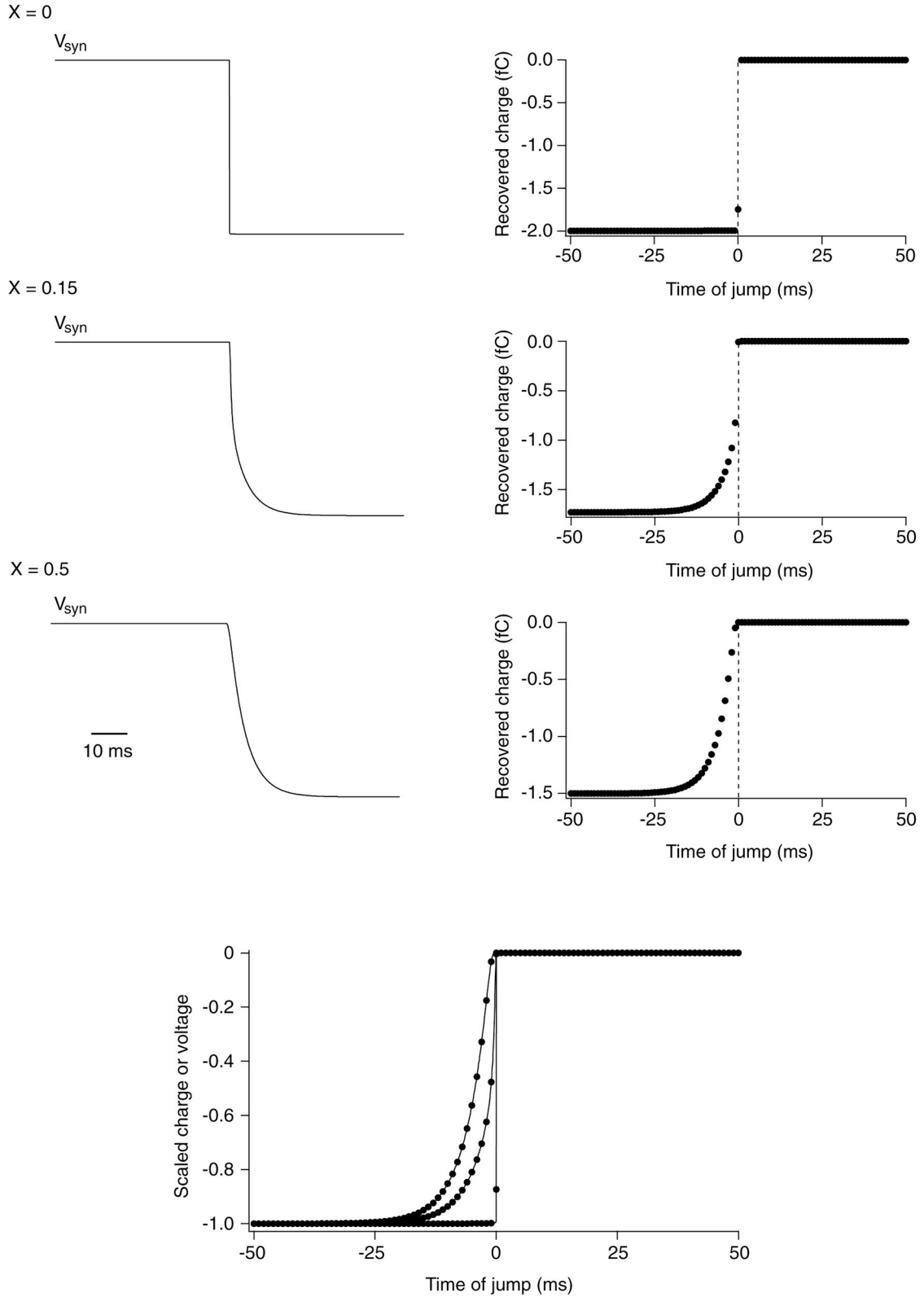
**Fig. 2.5.** Charge recovery after the onset of the synaptic conductance is determined by the synaptic decay. *A–D*, charge recovery plots for synaptic conductances with different kinetics: a brief pulse (*A*), or a double-exponential function with the same rising exponential (0.2 ms) and different decay time constants (1, 3 and 10 ms in *B*, *C* and *D*, respectively). Peak conductance 1 nS in each case; all synapses located at  $X = 0.15$  using the same equivalent cylinder as in Fig. 2.1. A single-exponential decay has been fit to the decay of the charge recovery in *B–D*; note the close correspondence with the decay time constant of the original synaptic conductance in each case. *E*, each charge recovery curve has been normalized by its value at the onset of the synaptic conductance and superimposed. The individual points of each curve have been joined by a line for clarity.

decay time constant can be optimized by examining the differentiated charge recovery (Fig. 2.4C), which helps to separate the curve into its two components. Generally, it was found that for a monoexponentially-decaying synaptic conductance the later the start time of the fit, the better the correspondence between the fit decay and actual decay, since starting the fit at later times helps to avoid potential distortions due to voltage escape (see section 2.3.7). Of course, when the synaptic

conductance time course is unknown it may be an oversimplification to assume that it has a single exponential decay (e.g. Pearce, 1993).

### Somatic voltage step

### Brief pulse of conductance



← **Fig. 2.6.** Charge recovery before the onset of the synaptic conductance reflects the voltage change at the synapse caused by the somatic voltage command. All simulations from the same equivalent cylinder as in Fig. 2.1. The left-hand panels show the synaptic voltage in response to a somatic voltage clamp step (of arbitrary amplitude) at three different locations. The right-hand panels show the charge recovery curves for a synaptic delta pulse (1 nS peak conductance) at the same three locations. The bottom panel shows a superposition of the synaptic voltage responses on the respective charge recoveries; both the charge recoveries and the voltage responses have been normalized by their respective maxima, and the time axis of the voltage response has been inverted. Note the exact correspondence of the voltage time course and the charge recovery in each case.

### 2.3.4 Charge recovery before the onset of the synaptic conductance is determined by the electrotonic distance of the synapse

Figure 2.6 demonstrates that the early component of the charge recovery, before the onset of the synaptic conductance, reflects the time course of the voltage change at the synapse produced by the somatic voltage command. This was shown by placing a brief pulse synaptic conductance at various distances from the recording site, thereby eliminating the influence of synaptic kinetics on the charge recovery. Under these conditions, the charge recovery curve for a synapse located at the soma was essentially a step function, while the curve for more distal synapses became progressively more rounded (Fig. 2.6, right panels). The same was true for the voltage responses to a somatic voltage jump measured at the corresponding locations (Fig. 2.6, left panels). The symmetry between the time courses of the two families of curves is demonstrated by overlaying the scaled voltage response on top of the charge recovery, as shown in the bottom panel of Fig. 2.6.

### 2.3.5 A simple analytical function describes the charge recovery curve

In a linear system, the voltage response at the synapse to a somatic voltage step can always be described by a sum of exponentials (Rall, 1969; Major et al., 1993; we follow the convention of Major et al. in setting resting membrane potential and the reversal potential of the synaptic conductance to zero). This sum is often dominated by a single exponential, with time constant  $\tau_v$  (see Fig. 2.4A),

$$V_{\text{syn}}(s,t) = \alpha V_{\text{com}} \Theta(t-s) \left( 1 - e^{-(t-s)/\tau_v} \right) \quad (2.1)$$

where  $\alpha$  is the steady-state attenuation factor of the voltage command  $V_{\text{com}}$  at the soma,  $\Theta$  is the Heaviside step function,  $\Theta(x) = \begin{cases} 1 & (x \geq 0) \\ 0 & (x < 0) \end{cases}$ , and  $s$  is the time of the voltage step with respect to the onset ( $t = 0$ ) of the synaptic conductance,  $g(t)$ . For simplicity, we first choose a "delta function" synaptic conductance

$$g(t) = g_0 \delta(t). \quad (2.2)$$

The resulting current flowing at the synapse

$$I_{\text{syn}}(s, t) = V_{\text{syn}}(s, t) g(t) \quad (2.3)$$

can be integrated over time to give the synaptic charge

$$Q_{\text{syn}}(s) = \int_{-\infty}^{\infty} I_{\text{syn}}(s, t) dt = \alpha V_{\text{com}} g_0 \Theta(-s) (1 - e^{s/\tau_v}), \quad (2.4)$$

which of course depends on the time of jump,  $s$  (see Fig. 2.4B). As long as voltage escape at the synapse can be neglected, the charge recovered at the somatic voltage clamp electrode

$$Q_{\text{soma}}(s) = \alpha^2 V_{\text{com}} g_0 \Theta(-s) (1 - e^{s/\tau_v}) \quad (2.5)$$

is a constant fraction  $\alpha$  of the total synaptic charge (Redman, 1973; Rinzel & Rall, 1974; Carnevale & Johnston, 1982; Jack et al., 1983; Rall and Segev, 1985; Major et al., 1993).

The assumption of a "delta function" synaptic conductance is unrealistic, and therefore we repeat the calculation in Eq. 2.4 with a synaptic conductance that rises instantaneously to a peak at  $t = 0$  and then decays exponentially with time constant  $\tau_{\text{dec}}$ ,

$$g(t) = \bar{g} \Theta(t) e^{-t/\tau_{\text{dec}}} \quad (2.6)$$

which yields a recovered charge

$$Q_{\text{soma}}(s) = \begin{cases} \frac{\alpha^2 V_{\text{com}} \bar{g} \tau_{\text{dec}} (\tau_{\text{dec}} + \tau_v (1 - e^{s/\tau_v}))}{\tau_{\text{dec}} + \tau_v} & (s \leq 0) \\ \frac{\alpha^2 V_{\text{com}} \bar{g} \tau_{\text{dec}}^2 e^{-s/\tau_{\text{dec}}}}{\tau_{\text{dec}} + \tau_v} & (s > 0) \end{cases} \quad (2.7)$$

that changes exponentially with a single time constant equal to  $\tau_v$  for voltage jumps occurring before the onset of the synaptic conductance, and a single time constant equal to  $\tau_{\text{dec}}$  afterwards (compare Figs. 2.6 and 2.5). The ratio of the amplitudes of the onset and offset phases of the charge recovery is equal to  $\tau_v / \tau_{\text{dec}}$ . As integration is a linear operation, the integral in Eq. 2.4 can still be evaluated if both the voltage response at the synapse and the synaptic conductance are described by sums of exponentials. The time constants of the charge recovery for  $s \leq 0$  are given by the time constants of the voltage response, and the time constants of the charge recovery for  $s > 0$  are given by the time constants of the synaptic conductance. We illustrate this for the case that the voltage response at the synapse is a sum of 2 exponentials

$$V_{\text{syn}}(s, t) = \alpha V_{\text{com}} \Theta(t - s) \left( a_{v_1} + a_{v_2} - a_{v_1} e^{-(t-s)/\tau_{v_1}} - a_{v_2} e^{-(t-s)/\tau_{v_2}} \right) \quad (2.8)$$

and the synaptic conductance is represented by 3 exponentials (1 for the rise and 2 for the decay)

$$g(t) = \Theta(t) \left( -(\bar{g}_1 + \bar{g}_2) e^{-t/\tau_{\text{rise}}} + \bar{g}_1 e^{-t/\tau_{\text{dec}_1}} + \bar{g}_2 e^{-t/\tau_{\text{dec}_2}} \right). \quad (2.9)$$

In this case the recovered charge is

$$Q_{\text{soma}}(s \leq 0) = \alpha^2 V_{\text{com}} \left( (a_{v_1} + a_{v_2}) \left( -(\bar{g}_1 + \bar{g}_2) \tau_{\text{rise}} + \bar{g}_1 \tau_{\text{dec}_1} + \bar{g}_2 \tau_{\text{dec}_2} \right) + a_{v_1} \tau_{v_1} e^{s/\tau_{v_1}} \left( \frac{(\bar{g}_1 + \bar{g}_2) \tau_{\text{rise}}}{\tau_{\text{rise}} + \tau_{v_1}} - \frac{\bar{g}_1 \tau_{\text{dec}_1}}{\tau_{\text{dec}_1} + \tau_{v_1}} - \frac{\bar{g}_2 \tau_{\text{dec}_2}}{\tau_{\text{dec}_2} + \tau_{v_1}} \right) + a_{v_2} \tau_{v_2} e^{s/\tau_{v_2}} \left( \frac{(\bar{g}_1 + \bar{g}_2) \tau_{\text{rise}}}{\tau_{\text{rise}} + \tau_{v_2}} - \frac{\bar{g}_1 \tau_{\text{dec}_1}}{\tau_{\text{dec}_1} + \tau_{v_2}} - \frac{\bar{g}_2 \tau_{\text{dec}_2}}{\tau_{\text{dec}_2} + \tau_{v_2}} \right) \right) \quad (2.10)$$

$$\begin{aligned}
Q_{\text{soma}}(s > 0) = & \alpha^2 V_{\text{com}} \left( (a_{v_1} + a_{v_2}) \left( -(\bar{g}_1 + \bar{g}_2) \tau_{\text{rise}} e^{-s/\tau_{\text{rise}}} + \right. \right. \\
& \left. \left. \bar{g}_1 \tau_{\text{dec}_1} e^{-s/\tau_{\text{dec}_1}} + \bar{g}_2 \tau_{\text{dec}_2} e^{-s/\tau_{\text{dec}_2}} \right) \right) + \\
& a_{v_1} \tau_{v_1} \left( \frac{(\bar{g}_1 + \bar{g}_2) \tau_{\text{rise}} e^{-s/\tau_{\text{rise}}}}{\tau_{\text{rise}} + \tau_{v_1}} - \frac{\bar{g}_1 \tau_{\text{dec}_1} e^{-s/\tau_{\text{dec}_1}}}{\tau_{\text{dec}_1} + \tau_{v_1}} - \frac{\bar{g}_2 \tau_{\text{dec}_2} e^{-s/\tau_{\text{dec}_2}}}{\tau_{\text{dec}_2} + \tau_{v_1}} \right) + \\
& a_{v_2} \tau_{v_2} \left( \frac{(\bar{g}_1 + \bar{g}_2) \tau_{\text{rise}} e^{-s/\tau_{\text{rise}}}}{\tau_{\text{rise}} + \tau_{v_2}} - \frac{\bar{g}_1 \tau_{\text{dec}_1} e^{-s/\tau_{\text{dec}_1}}}{\tau_{\text{dec}_1} + \tau_{v_2}} - \frac{\bar{g}_2 \tau_{\text{dec}_2} e^{-s/\tau_{\text{dec}_2}}}{\tau_{\text{dec}_2} + \tau_{v_2}} \right) \Bigg)
\end{aligned}$$

In order to allow well-conditioned fits of charge recovery data, the amplitudes  $a_{v_1}$  and  $a_{v_2}$  in Eq. 2.10 were normalized according to  $a_{v_1} + a_{v_2} = 1$ . The factors  $\alpha^2$ ,  $V_{\text{com}}$ ,  $\bar{g}_1$  and  $\bar{g}_2$  were combined in two overall amplitudes of the fit function,  $g_1^* = \alpha^2 V_{\text{com}} \bar{g}_1$  and  $g_2^* = \alpha^2 V_{\text{com}} \bar{g}_2$ , which were free parameters of the fit. Constant offsets in  $s$  and  $Q_{\text{soma}}(s)$  can also be introduced to allow latency variations and jumps from other potentials than the apparent reversal potential of the synaptic conductance.

In practice it may not always be necessary (or possible) to fit the entire analytical function. As demonstrated above, the charge recovery can be separated into two components, with the second determined by the kinetics of the conductance (see Fig. 2.5 and Eqs. 2.7 and 2.10). This can be exploited experimentally in situations where the time of recording is limited, or where only the decay of the synaptic conductance is of interest. By making a series of jumps at different times following the onset of the synaptic conductance and then fitting the decay of the recovered charge with an exponential function, an estimate can be made of the decay of the conductance (assuming that  $\tau_{\text{rise}} \ll \tau_{\text{decay}}$ ). It is also possible to fit multiple exponential functions to the decay; in this case, the time constants will be extracted faithfully, but the relative amplitudes of the faster components will be underestimated; accuracy can be improved by fitting the differentiated charge recovery.

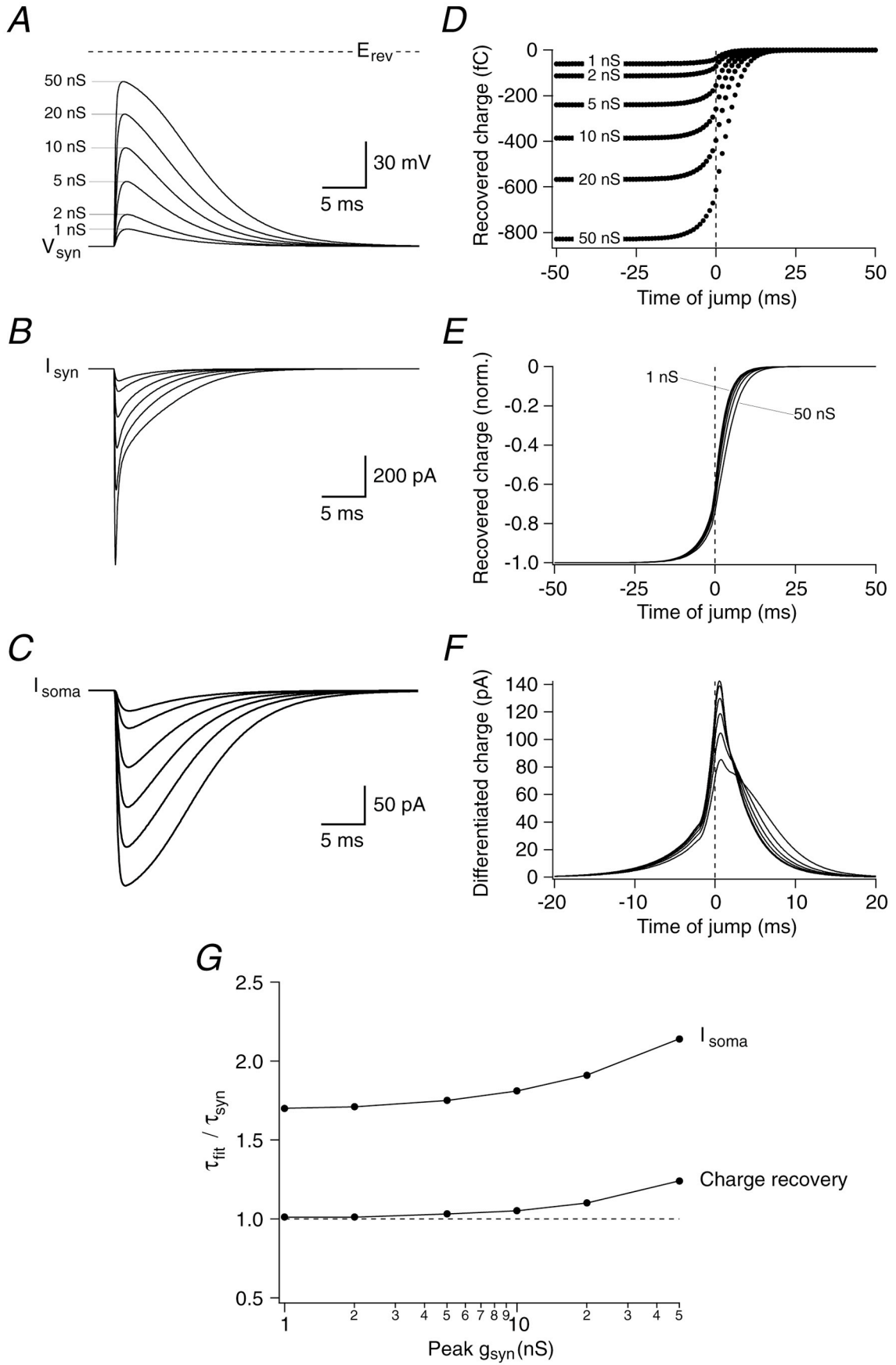
This "shortcut" also allows the voltage jump method to be applied to spontaneous synaptic currents, by triggering voltage jumps (using a software or hardware trigger) with a variable delay after the synaptic current crosses a threshold amplitude. Some jitter will be introduced in the time of the jump if the spontaneous currents have widely different amplitudes and/or risetimes; this can be corrected for by later normalizing the time of each jump to a reference point on the rise. As with evoked synaptic conductances, the mean decay time course of the underlying conductances can then be estimated from the charge recovery curve.

### 2.3.6 The voltage jump method also works in current-clamp mode

In principle, a change in driving force at the synapse can be generated either with a voltage command under voltage clamp, or by injecting a fixed amount of current to generate a reproducible voltage change in current-clamp mode. Since the analytical solutions for both the time integral of synaptic potentials and the synaptic charge in voltage clamp depend only on the charge flowing at the synapse (Major et al., 1993), one can fit the curve of the time integral of the synaptic potentials obtained following a series of identical square current pulses with Eqs. 2.7 or 2.10. In this case, the measured  $\tau_v$  will be determined by the membrane time constant  $\tau_m$ , since  $\tau_m$  determines the dendritic voltage response to a square current step (neglecting the faster equalization time constants, which generally have much smaller amplitudes for a long current step). Although the kinetics of the synaptic conductance can be extracted reliably as described above, since  $\tau_m \gg \tau_{\text{decay}}$  for most neurons and synaptic conductances the amplitude of the time integral curve will be dominated by the component attributable to  $\tau_m$  (the "onset"). Therefore, for determining the time course of the synaptic conductance it is always preferable to use voltage clamp rather than current clamp, since  $\tau_v$  for voltage clamp will always be smaller than  $\tau_m$  (except in the limiting case, where they are identical; Major et al., 1993) and thus provide better signal-to-noise for extracting  $\tau_{\text{rise}}$  and  $\tau_{\text{decay}}$ . Voltage clamp will also reduce the voltage excursion at the synapse (although only slightly for some synapses; see Roth & Häusser, 2001) and thus also distortion in the synaptic current. For these reasons all subsequent simulations were done in voltage clamp mode.

### 2.3.7 Effect of voltage escape at the synapse

The analytical function derived in section 2.3.5 assumes that the voltage escape associated with the synaptic current at the synaptic site is negligible. Since some voltage escape will inevitably be associated with somatic voltage clamp of dendritic synapses, it is therefore necessary to test how voltage escape affects the accuracy of the method. This was done using the equivalent cylinder model by progressively increasing the magnitude of the peak synaptic conductance at a given location. The results of such simulations are shown in Fig. 2.7. As the synaptic conductance is increased, the voltage escape at the synapse progressively approaches the synaptic reversal potential (Fig. 2.7A), causing substantial distortions both in the current flowing at the synapse (Fig. 2.7B) as well as in the current recorded at the soma (Fig. 2.7C). The charge recovery curves obtained from the same synapses (Fig. 2.7D–E) show a progressive distortion and slowing after





← **Fig. 2.7.** Effects of local depolarization ("voltage escape") on the reliability of the charge recovery method. *A–C*, simulations from the same equivalent cylinder as in Fig. 2.1, with the synapse at a constant location ( $X = 0.15$ ), and with a range of peak synaptic conductances as indicated (rising and decaying time constant 0.2 and 3.0 ms respectively). *A* shows the voltage at the synapse, *B* the current flowing at the synapse, and *C* the current recorded at the soma. The charge recovery plots from the various conductances are shown unscaled in *D*, scaled by the peak charge in *E*, and scaled and differentiated in *F*. The bottom panel compares the decay time constant obtained by fitting either the somatic current or the charge recovery plot with the actual decay of the synaptic conductance (fit beginning 7 ms after onset of the conductance in each case). Note that the time constant estimated by the charge recovery is relatively faithful to the input time constant except at very high values of peak conductance.

$t = 0$  (made clearer by differentiation in Fig. 2.7*F*). When comparing the decay time constant fit to the charge recovery curve with the actual time course of decay of the conductance (Fig. 2.7*G*), serious errors (>10%) were found only for the largest conductances ( $\geq 20$  nS). These errors could be further reduced by changing the fit range: fits with a later onset produced greater accuracy (although, as pointed out in section 2.3.3, this is not feasible for conductances which may contain a slow component). By contrast, the time constants fit to the decay of the current measured at the soma were seriously in error for all conductance values chosen; delaying the onset of the fit produced little improvement in accuracy.

These findings suggest that the voltage jump method can reliably extract the decay time course of the synaptic conductance over a wide range of magnitudes of the conductance, but that the substantial voltage escape associated with very large, highly localized synaptic conductances may reduce its accuracy. The amplitude of the voltage escape will depend not only on the magnitude of the conductance, but also on the geometry of the cell as well as its electrical properties. To rigorously test the method it is therefore of great importance to carry out simulations in compartmental models of reconstructed neurons, with realistic values for the membrane parameters and the synaptic conductance.

### 2.3.8 Application to realistic neuronal geometries: CA3 pyramidal cell

Figure 4.8 shows a test of the voltage jump method in a detailed compartmental model of a CA3 pyramidal cell (Major et al., 1994). As shown previously (Major et al., 1994), a synaptic input placed on the distal apical dendrites (Fig. 2.8*A*) is substantially filtered and attenuated by space-clamp errors (Fig. 2.8*B*). The voltage jump protocol was carried out at a holding potential of  $-65$  mV. Since the analytical function assumes that the system is passive, it should not matter from which holding potential the jumps are made, nor which voltage is jumped to, as long as there is a change in synaptic driving force; the charge recovery curve is simply

shifted downwards on the y-axis by the difference in synaptic charge at the two holding potentials. By fitting the charge recovery with Eq. 2.10 it was possible to

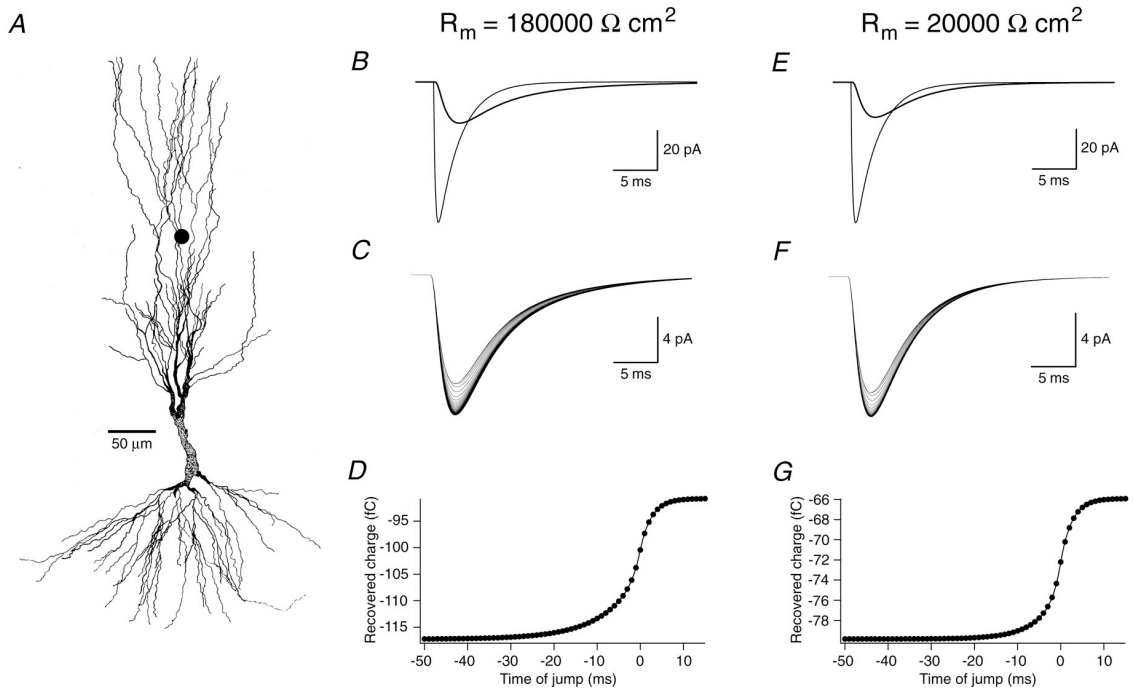


**Fig. 2.8.** The voltage jump method is successful in a CA3 pyramidal cell model even under conditions of high membrane conductance. A shows the morphology of the CA3 pyramidal cell with which the simulations were carried out. A synaptic conductance (peak 0.5 nS) consisting of a double-exponential function ( $\tau_{\text{rise}} = 0.2$  ms;  $\tau_{\text{dec}} = 2.5$  ms) was placed on a spine head with the location indicated by the filled circle. The parameters for B–D and E–G were identical except that  $R_m$  was decreased from 180 k $\Omega$  cm $^2$  in B to 20 k $\Omega$  cm $^2$  in E; this reduced the input resistance from 305 M $\Omega$  to 43.4 M $\Omega$ . In B and E, the somatic clamp current resulting from activation of the synaptic conductance is shown (thick trace), as well as the synaptic current expected under conditions of perfect space clamp. Note the slightly greater peak attenuation under the low- $R_m$  condition. The 20–80% risetimes of the currents were 1.00 ms in B and 0.94 ms in E. The decay time course of the somatic clamp current could be fit with a single exponential function with  $\tau = 6.44$  ms in B and 4.92 ms in E. In C and F the currents recovered by a series of  $-20$  mV voltage jumps from  $-65$  mV are shown (1 ms interval between jumps). In D and G the charge recovery curves measured from the traces in C and F are shown together with the best fit of the analytical function. Note the different onset of the two curves. For the high- $R_m$  condition the best fit was with the following parameters:  $\tau_{v1} = 1.58$  ms (40%),  $\tau_{v2} = 8.53$  ms (60%),  $\tau_{\text{rise}} = 0.22$  ms;  $\tau_{\text{dec}} = 2.55$  ms. For the low- $R_m$  condition the best fit was with:  $\tau_{v1} = 1.43$  ms (48%),  $\tau_{v2} = 5.42$  ms (52%),  $\tau_{\text{rise}} = 0.23$  ms;  $\tau_{\text{dec}} = 2.55$  ms. A single-exponential fit to the decay of the charge recovery curve gave  $\tau_{\text{dec}} = 2.55$  and 2.53 ms respectively.

extract the decay of the synaptic conductance with high accuracy (< 5% error; see legend to Fig. 2.8 for details). To determine the effect of high membrane conductance on the accuracy of the method,  $R_m$  was decreased from 180 k $\Omega$  cm $^2$  to 20 k $\Omega$  cm $^2$  (resulting in a reduction of the somatic input resistance from 305 M $\Omega$  to 43.4 M $\Omega$ ). Under these conditions, as might be expected to occur *in vivo* due to tonic

synaptic background activity, the method extracted the decay time course of the conductance to within 2% error (Fig. 2.8E–G). The method also maintained high

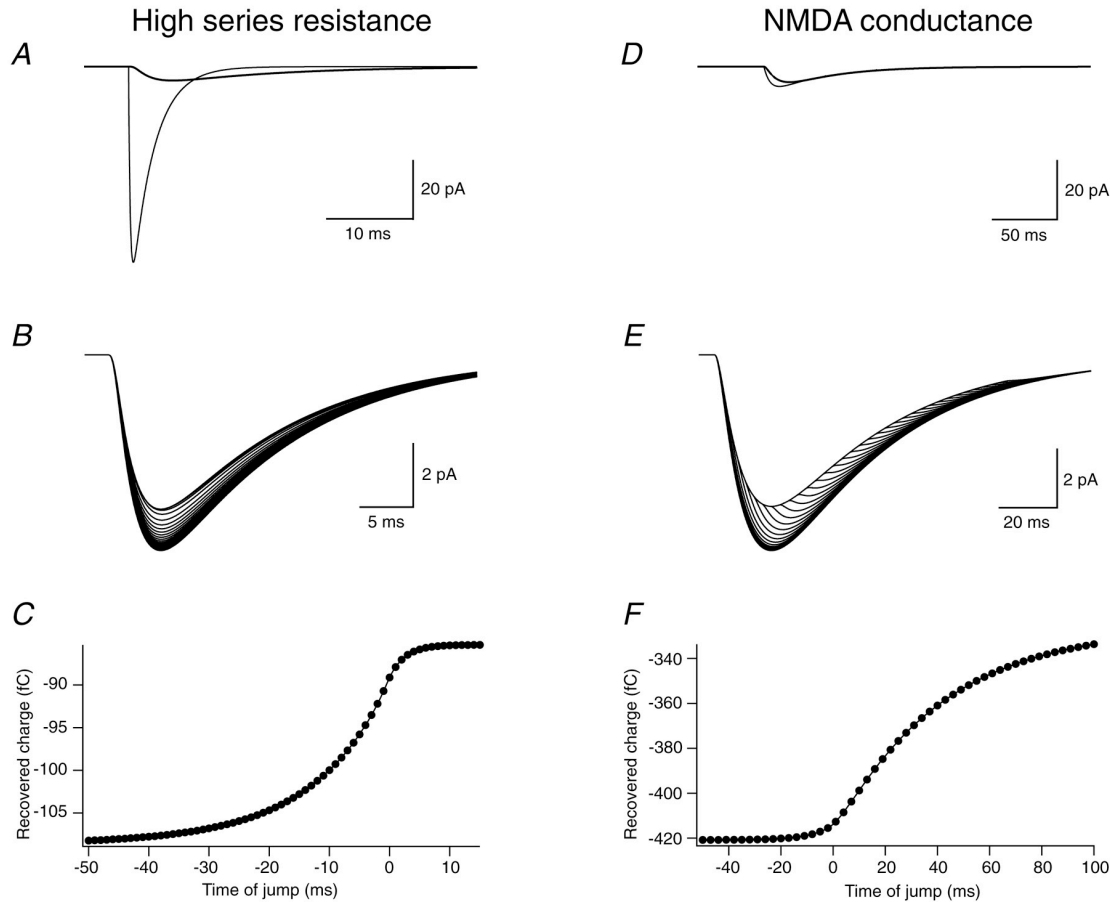


**Fig. 2.9.** The method can be used with high series resistance and to extract slow risetimes. Simulations carried out using the CA3 pyramidal cell model with the same synaptic location as in Fig. 2.8. In A–C, a fast double-exponential synaptic conductance (peak 0.5 nS,  $\tau_{\text{rise}} = 0.2$  ms,  $\tau_{\text{dec}} = 2.5$  ms; same as in Fig. 2.8) was simulated with the series resistance of the somatic pipette being 20 MΩ. In D–E a NMDA receptor-mediated synaptic conductance was simulated (peak 0.1 nS,  $\tau_{\text{rise}} = 5.0$  ms,  $\tau_{\text{dec}} = 40$  ms), with a 0.5 MΩ series resistance, assuming zero external  $\text{Mg}^{2+}$ . A and D compare the perfectly clamped synaptic current with the measured somatic current. The 20–80% risetimes of the currents were 1.71 ms in A and 7.17 ms in D. The decay of the somatic current in A could be fit with a single exponential with  $\tau = 12.90$  ms. The somatic NMDA current in D was fit with a double-exponential function, with  $\tau_{\text{rise}} = 9.6$  ms and  $\tau_{\text{dec}} = 39.8$  ms. The currents recovered by voltage jumps from  $-65$  to  $-85$  mV are shown in B and E; for clarity, only every second jump is shown in B. The respective charge recovery curves are shown in C and F. In C the values of the best fit of the analytical function were  $\tau_{v1} = 2.15$  ms (5%),  $\tau_{v2} = 12.75$  ms (95%),  $\tau_{\text{rise}} = 0.19$  ms;  $\tau_{\text{dec}} = 2.56$  ms, while in F the values were  $\tau_{v1} = 1.45$  ms (41%),  $\tau_{v2} = 8.58$  ms (59%),  $\tau_{\text{rise}} = 5.15$  ms;  $\tau_{\text{dec}} = 40.4$  ms. A single-exponential fit to the decay of the charge recovery curves in C and F gave  $\tau_{\text{dec}} = 2.53$  and 41.2 ms respectively.

accuracy under conditions of high uncompensated series resistance (20 MΩ; Fig. 2.9A–C). Note that in these simulations, the time course of the initial phase of the charge recovery (and the  $\tau_v$  values extracted by fitting the analytical function)

were much slower than with low series resistance, consistent with the greater effective electrotonic distance of the synapse in the high series resistance condition.

To test whether it is also possible to extract accurately the risetime of a slow synaptic conductance, an NMDA receptor-mediated EPSC (Kirson & Yaari, 1996)

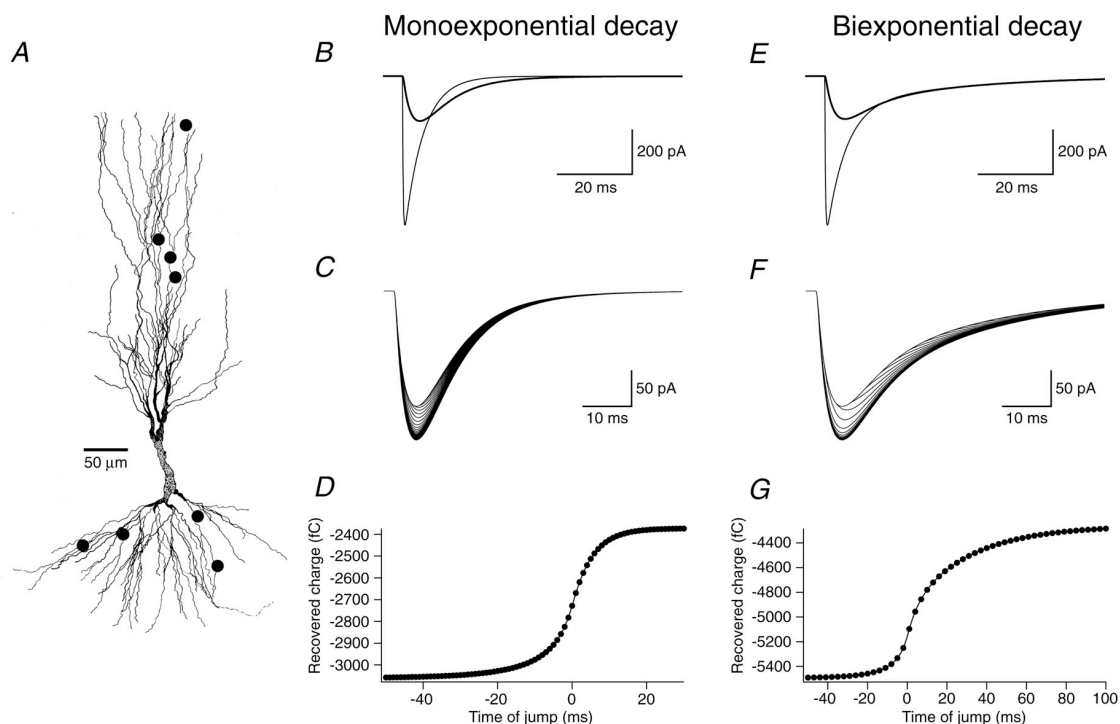


**Fig. 2.10.** Simulation of a distributed inhibitory conductance in a CA3 pyramidal cell. A unitary connection made by a presynaptic "bitufted" inhibitory neuron is modeled, based on Figure 2 of Miles et al. (1996). The locations of the 8 individual contacts on apical and basal dendritic shafts are shown using dots in A. Each synaptic contact had an identical synaptic conductance, with a peak conductance of 1 nS. The rising time constant was 0.2 ms in all cases, and the decay time constant was either a single exponential of 5 ms (B–D) or a double exponential of 5 ms (80%) and 30 ms (20%). B and E compare the somatic clamp current with the perfectly clamped EPSC. The 20–80% risetimes of the currents were 1.66 ms in A and 1.89 ms in B. The decay of the somatic clamp current could be fit by a single exponential with  $\tau = 9.5$  ms and 22.2 ms respectively. C and F show the recovered currents from successive voltage jumps from  $-65$  mV. D and G show the charge recovery curves, which have been fit with the analytical function. For the monoexponentially decaying conductance, the best fit of the analytical function was with the following parameters:  $\tau_{v1} = 3.24$  ms (57%),  $\tau_{v2} = 10.93$  ms (43%),  $\tau_{rise} = 0.66$  ms;  $\tau_{dec} = 5.22$  ms; fitting the decay of the charge recovery curve with a single exponential gave  $\tau_{dec} = 5.16$  ms. For the conductance with a biexponential decay the best fit was with the following parameters:  $\tau_{v1} = 3.26$  ms (59%),  $\tau_{v2} = 11.11$  ms (41%),  $\tau_{rise} = 0.48$  ms;  $\tau_{dec1} = 5.17$  ms (77%);  $\tau_{dec2} = 30.54$  ms (23%). A double-exponential fit to the decay of the charge recovery gave  $\tau_{dec1} = 5.02$  ms (66%);  $\tau_{dec2} = 30.48$  ms (34%).

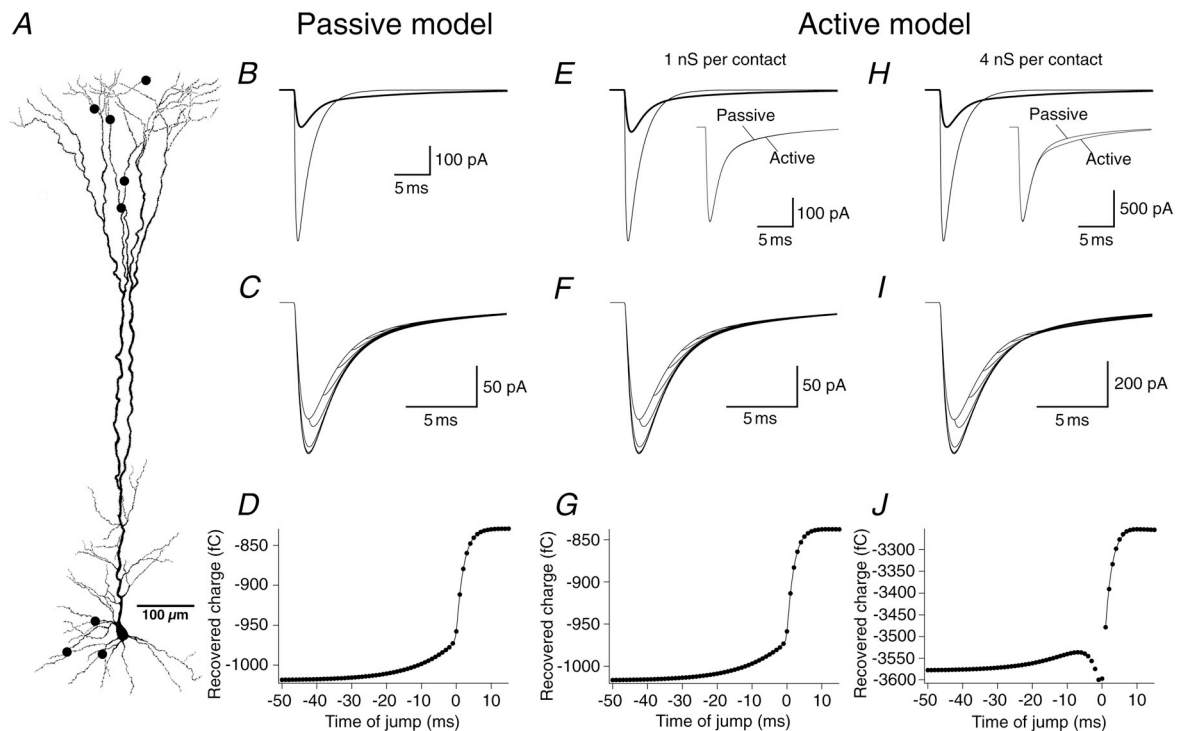
was simulated at the same synaptic location indicated in Fig. 2.8A. Although the decay of this synaptic current was not significantly distorted due to its slow time course, the risetime was slowed substantially (from  $\tau_{rise} = 5.0$  to 9.6 ms; Fig. 2.9D). From the charge recovery (Fig. 2.9E–F), the analytical function was able to extract

the risetime (as well as the decay) to within 3% of its original value, indicating that the method may also be useful for this purpose.

To examine the effectiveness of the method for distributed conductances in the CA3 pyramidal cell an inhibitory connection was simulated (Fig. 2.10), with the location of the contacts based on a reconstructed connection between an interneuron and a simultaneously recorded CA3 pyramidal cell (Fig. 2 in Miles et al., 1996). Either single- or double-exponentially decaying conductances were simulated at each contact (Pearce, 1993). When the decay of the synaptic conductance was double-exponential the fast component of the decay was filtered more heavily than the slow component, such that the synaptic current measured at the soma could be fit with a single exponential with a time constant intermediate to the two time constants of the conductance decay. Since the synapses in this simulation were at widely distributed electrotonic locations, when applying a somatic voltage jump each synapse experienced voltage transients with a different time course. This caused slight distortions of the risetime extracted with the analytical function. The decay appeared to be relatively little affected by this non-uniformity, as with both the single- and double-exponentially decaying conductances it was possible to extract the time constants and their relative amplitudes to a high degree of accuracy (< 5% error). To test the effect of the synaptic conductance kinetics on the accuracy of the method, I also performed simulations under the same conditions with a conductance decay time constant of 1 ms. The decay time constant extracted by the method was 1.01 ms (data not shown), confirming that high accuracy could be maintained even with rapid input kinetics.

### **2.3.9 Application to realistic neuronal geometries: Neocortical pyramidal cell**

Simulations were also done using a detailed compartmental model of a layer 5 pyramidal cell (Markram et al., 1997), a cell type which has one of the most extensive dendritic trees of any neuron in the brain. A morphologically reconstructed unitary input made by an adjacent, simultaneously recorded layer 5 pyramidal cell was simulated, which made 8 contacts at widely dispersed electrotonic locations (mean  $X = 0.71$ , range 0.063–1.4, for the passive parameters chosen here). Of particular interest was the possibility to test the voltage jump method using an active membrane model of neocortical layer 5 pyramidal cells, which contains a variety of voltage-gated conductances and reproduces the firing pattern of these neurons (Mainen & Sejnowski, 1996). When activating the distributed input under passive conditions, the analytical function extracted the decay time constant of the synaptic conductance to within 5% error, despite substantial filtering of the synaptic current



waveform (Fig. 2.11B–D). When active conductances were included in the model, simulations with 1 nS peak conductance per contact produced results which were very similar to those found with the passive model, consistent with the lack of distortion in the synaptic current (Fig. 2.11E, inset). When the peak synaptic conductance was increased to 4 nS per contact, however, an obvious "boosting" component could be observed in the decay of the synaptic current (Fig. 2.11H, inset). The "boosting" current arose almost exclusively via activation of sodium and calcium conductances in the apical tuft branches (not shown); virtually no boosting was observed at the peak of the synaptic current, primarily because the measured peak is dominated by current from basal inputs, which are better clamped.

The extra charge contributed by the active conductances caused clear distortions in the charge recovery curve, with an extra component emerging in the onset of the charge recovery, representing jumps made just before the beginning of the synaptic conductance. The shape of this extra component results from a highly non-linear process involving the increase in the driving force caused by the hyperpolarization, which is still weak enough at "late" times to permit activation of voltage-gated channels. Despite this distortion, the charge recovery after  $t = 0$  ms remained dominated by the decay of the synaptic conductance: when a single exponential was fit to this component, the decay was estimated to within 10%. In this model, therefore, the errors caused by active conductances depend on various factors, particularly the size of the synaptic conductance (Fig. 2.11E,H) and the holding potential. These findings demonstrate that care must be taken to choose the

← **Fig. 2.11.** Simulation of a distributed synaptic connection in an active layer 5 pyramidal cell model. A reconstructed synaptic connection made by a single presynaptic layer 5 pyramidal neuron is simulated, with 8 contacts (marked by dots in *A*) distributed on apical and basal dendritic spines (Markram et al., 1997). All synaptic conductances are identical ( $\tau_{\text{rise}} = 0.20$  ms;  $\tau_{\text{dec}} = 2$  ms). The model was either passive (*B–D*) or contained active conductances (*E–J*) as described in section 2.2.3. The peak synaptic conductance at each contact was either 1 nS or 4 nS; the kinetics of the currents and charge recoveries obtained from the 1 nS and 4 nS passive simulations were nearly identical, and therefore only the results from the 1 nS simulation are shown. *B*, *E* and *H* compare the somatic clamp current at a holding potential of  $-65$  mV with the perfectly clamped EPSC for the passive and active model. The insets in *E* and *H* compare the clamp current in the active model with that of the corresponding simulation in the passive model (same time period as in the main panels; scale bars apply to the larger traces). Note that in the simulations with 1 nS peak conductance, the active and passive models produce a virtually identical EPSC, while in the 4 nS simulation the EPSC in the active model clearly shows an additional current component in the tail of the EPSC. The 20-80% risetimes of the somatic EPSCs were 0.36 ms in each case. The decay of the somatic EPSCs could be fit by a single exponential with  $\tau = 3.3$  ms in the passive simulations as well as in the active 1 nS simulation, and with  $\tau = 3.7$  ms in the 4 nS active simulation. *C*, *F*, and *I* show the recovered currents from successive  $-20$  mV hyperpolarizing voltage jumps from a holding potential of  $-65$  mV. The respective charge recovery curves measured from the recovered currents are shown in *D*, *G* and *J*. In *D* and *G*, the curves have been fit with the analytical function. The best fit in the passive model gave  $\tau_{v1} = 0.36$  ms (69%),  $\tau_{v2} = 11.3$  ms (31%),  $\tau_{\text{rise}} = 0.22$  ms;  $\tau_{\text{dec}} = 2.02$  ms, whereas in the active model the values were  $\tau_{v1} = 0.23$  ms (69%),  $\tau_{v2} = 11.6$  ms (31%),  $\tau_{\text{rise}} = 0.34$  ms;  $\tau_{\text{dec}} = 1.90$  ms. A single-exponential fit to the decay of the charge recovery gave  $\tau_{\text{dec}} = 2.00$  ms in both cases. Due to the distortion of the charge recovery in the 4 nS active simulation, a fit of the analytical function was not possible. However, the decay phase of the charge recovery was fit with a single exponential of 1.90 ms.

appropriate voltage range over which to carry out the voltage jumps, and that tests must be done to evaluate the possible contribution of voltage-gated conductances.

### 2.3.10 Estimating synaptic conductance time course with a train of brief voltage jumps

One potential drawback of the voltage jump method described so far is that many trials are necessary to build up a charge recovery curve. This can be time-consuming, and also does not allow measurement of fluctuations in the decay of the synaptic conductance from trial to trial. To overcome this problem an alternative method was developed to allow measurement of the time course of the conductance each time it was activated. This method relies on the fact that the peak amplitude of the current recovered by a voltage jump made during the decay of the conductance is proportional to the additional charge associated with the jump (assuming a monoexponential decay of the conductance). In other words, the decrease in the peak of the recovered current with successive jumps will be determined by the decay of the underlying conductance (see Fig. 2.4A): under perfect clamp conditions, the recovered current will rise instantaneously to merge with the synaptic current decay. The same relationship should also hold for the peak current in response to a brief voltage pulse, which is limited by the risetime of the recovered current during the

voltage pulse. A train of identical brief voltage pulses should therefore be able map the time course of the conductance (cf. Smith et al., 1967). For brief synaptic conductances the accuracy of the method can be improved by increasing the

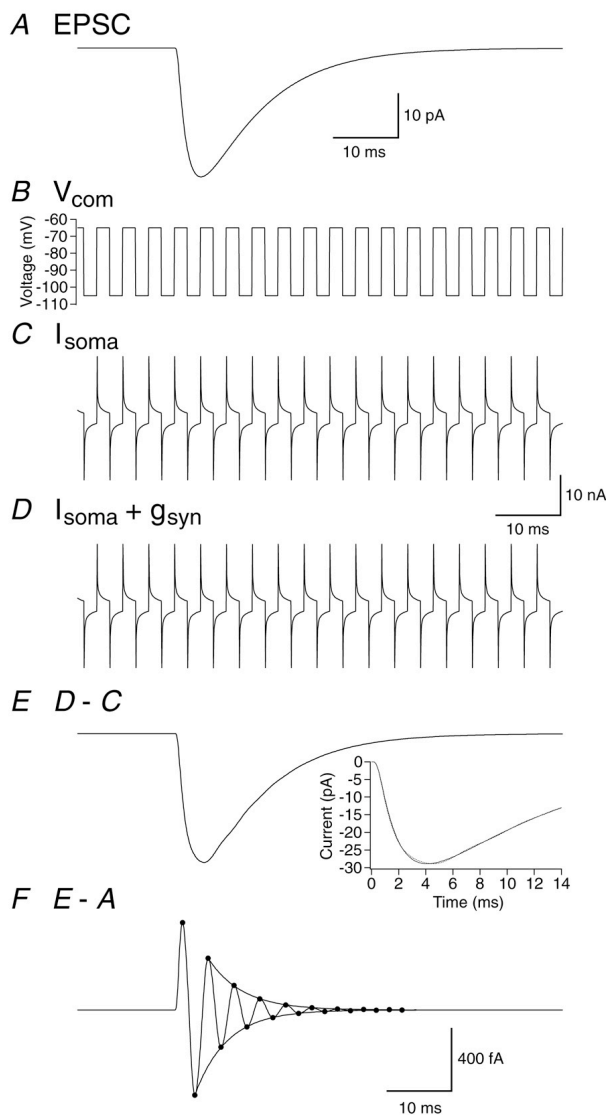


**Fig. 2.12.** Estimating the decay time course of the synaptic conductance with a train of brief voltage steps. The simulations were carried out using the CA3 pyramidal cell model with the same synaptic location as shown in Fig. 2.8. The synaptic conductance consisted of a sum of exponentials (peak 1.0 nS,  $\tau_{\text{rise}} = 0.2$  ms,  $\tau_{\text{dec}} = 5.0$  ms). *A*, the EPSC recorded by the somatic voltage clamp at a holding potential of  $-85$  mV. The decay time course of the current could be fit with a single exponential with  $\tau_{\text{dec}} = 10.0$  ms. *B*, the voltage clamp command applied via the somatic pipette, consisting of a series of 2 ms jumps from  $-65$  mV to  $-105$  mV, with 50% duty cycle. The resulting voltage at the synapse is also shown (jagged trace). *C* and *D*, the somatic clamp currents in the absence (*C*) and during (*D*) activation of the synaptic conductance (the difference between the two currents is undetectable at this scale). *E*, the difference current recovered by subtracting trace *D* from trace *C* (same scale bar as in *A*). The inset overlaps trace *A* and trace *E* (dotted line) at a higher magnification to demonstrate more clearly the distortion present in trace *E* due to the somatic voltage jumps. *F*, subtraction of the EPSC recorded at  $-85$  mV (trace *A*) from trace *E*. The maxima and minima of the curve have been calculated and are shown as dots superimposed on the curve (up to 35 ms from the conductance onset). A single-exponential fit to both the maxima and the minima is also shown, starting at the second maximum and the first minimum, and giving  $\tau_{\text{dec}}$  of 5.24 ms and 4.96 ms respectively. More accurate fits could be achieved by starting the fit at later times; e.g. by starting at the 4th maximum,  $\tau_{\text{dec}}$  was constrained to 5.00 ms.

frequency of the voltage pulses.

This procedure was tested (Fig. 2.12) in the CA3 pyramidal cell model, with the same excitatory synapse as in Fig. 2.8. A series of voltage pulses of 2 ms duration was applied via the somatic clamp electrode, once in the presence and once



in the absence of the synaptic conductance. The two somatic clamp currents resulting from this procedure were subtracted to obtain the difference current. This difference current contains a component which results from the increase in driving force caused by the voltage transients, superimposed on top of the synaptic current waveform. To isolate the transients, the synaptic current measured at a voltage intermediate to the two jump potentials (in this case, at  $-85$  mV) was subtracted from the difference current, giving the waveform shown in Fig. 2.12F. By fitting the maxima of this waveform (or the minima, or a combination of the two), it is theoretically possible to estimate the decay time course of the synaptic conductance. It should be pointed out, however, that this method suffers from very serious signal-to-noise problems, due to strong attenuation of the brief voltage transients in the dendritic tree (cf. Rall, 1967; Smith et al., 1967). In order to make a reliable estimate of the decay time course of the synaptic conductance at distal synapses using this method it may therefore be necessary to average many sweeps, which defeats its purpose. For this reason, the "train-of-brief-jumps" variant of the voltage jump method was not pursued further.

### 2.3.11 Estimating the attenuation of synaptic charge

Although the voltage jump method provides the kinetics of the synaptic conductance under conditions of inadequate space-clamp, it offers no direct information about its magnitude, which is also difficult to measure experimentally. The peak amplitude of the conductance can be calculated, however, if the total synaptic charge is known in addition to the kinetics of the conductance. Determining the total synaptic charge from the somatically recorded current is possible given the attenuation of synaptic charge,  $\alpha$  (introduced in Eqs. 2.1 and 2.5). Analytical solutions demonstrate that in a linear system the attenuation of synaptic charge from the synapse to the soma is equivalent to the attenuation of steady-state voltage from the soma to the synapse (Redman, 1973; Rinzel & Rall, 1974; Carnevale & Johnston, 1982; Jack et al., 1983; Rall & Segev, 1985; Major et al., 1993). If the reversal potential of the synaptic conductance is known, it is possible in principle to estimate the attenuation of steady-state voltage between the soma and the synapse in any arbitrary geometry by comparing the apparent synaptic reversal potential measured at the soma with the expected value (Carnevale & Johnston, 1982; Jack et al., 1983; Rall & Segev, 1985). Here I demonstrate how to estimate the attenuation factor  $\alpha$  using the layer 5 pyramidal cell model, and provide quantitative predictions of the magnitude of errors in  $\alpha$  resulting from the voltage escape caused by having a finite synaptic conductance.

Figure 2.13 shows the attenuation of the synaptic current, the voltage escape at the synapse, and the resulting distortion of the current flowing at the synapse for five identical synapses at different locations (indicated by horizontal arrows in Fig. 2.13A) in the layer 5 pyramidal cell model. Synaptic charge under perfect clamp will differ from the charge measured by somatic voltage clamp for the following reasons:

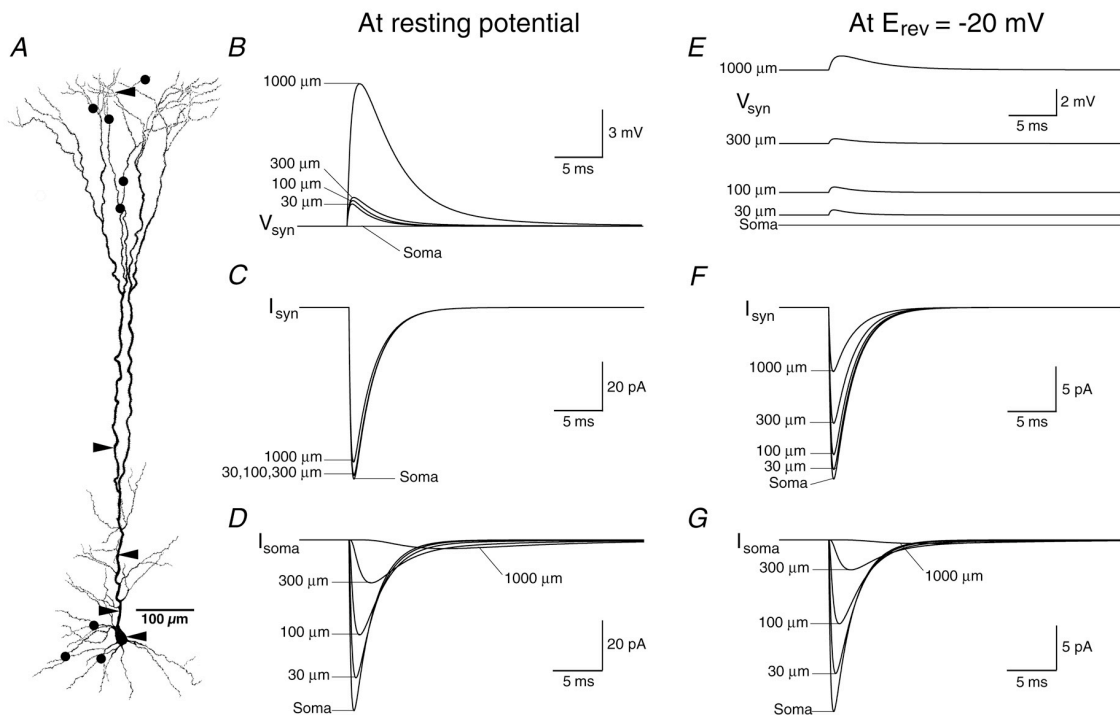


**Fig. 2.13.** Attenuation of synaptic currents in layer 5 pyramidal cells. The location of the 5 synapses used in the simulation is shown using arrowheads in *A*. All synapses had identical conductances (peak  $g_{\text{syn}} = 1.0 \text{ nS}$ ;  $\tau_{\text{rise}} = 0.20 \text{ ms}$ ;  $\tau_{\text{dec}} = 2 \text{ ms}$ ), and each synapse was activated individually. The somatic holding potential in *B–D* was at the resting potential ( $-70 \text{ mV}$ ), and in *E–F* it was at  $20 \text{ mV}$  hyperpolarized to the apparent reversal potential. *B* and *E* show the voltage escape at the synapse. Note the difference in steady-state synaptic voltage in *E*; as a consequence, the voltage escape is no longer a monotonic function of synaptic distance. *C* and *F* show the synaptic current flowing at the synapse. Note that the reduction in driving force as a consequence of the voltage escape causes a corresponding reduction in the amplitude of the synaptic current. In *F*, there is an additional reduction in the current at the synapse caused by the difference in steady-state driving force at the different synapses. *D* and *G* show the synaptic current measured at the soma following activation of synapses at different locations. Note the striking distortion and reduction in peak amplitude of the currents originating at progressively more distal locations. The 20–80% risetimes of the synaptic currents measured at the soma were: soma synapse,  $0.18 \text{ ms}$ ;  $30 \mu\text{m}$ ,  $0.25 \text{ ms}$ ;  $100 \mu\text{m}$ ,  $0.37 \text{ ms}$ ;  $300 \mu\text{m}$ ,  $0.78 \text{ ms}$ ;  $1000 \mu\text{m}$ ,  $3.12 \text{ ms}$ . The decay time constant for somatic currents originating at the different locations was: soma synapse,  $2.00 \text{ ms}$ ;  $30 \mu\text{m}$ ,  $2.24 \text{ ms}$ ;  $100 \mu\text{m}$ ,  $2.62 \text{ ms}$ ;  $300 \mu\text{m}$ ,  $4.14 \text{ ms}$ ;  $1000 \mu\text{m}$ ,  $12.6 \text{ ms}$ .

a) the attenuation of synaptic charge between synapse and soma,  $\alpha$ ; b) the reduction in synaptic driving force caused by voltage escape, and c) the difference in driving force at the synapse and the soma when the neuron is not isopotential in the steady-state. At the resting potential (Fig. 2.13*B–D*), the neuron is isopotential (assuming the passive reversal potential is uniform), and thus only a) and b) will have an effect.

Whenever the neuron is held away from the resting potential (Fig. 2.13E–G), all three effects will contribute to deviations from the expected synaptic charge.

The attenuation of voltage in the dendritic tree during a somatic voltage step at five synaptic locations is shown in Fig. 2.14A. This attenuation causes a

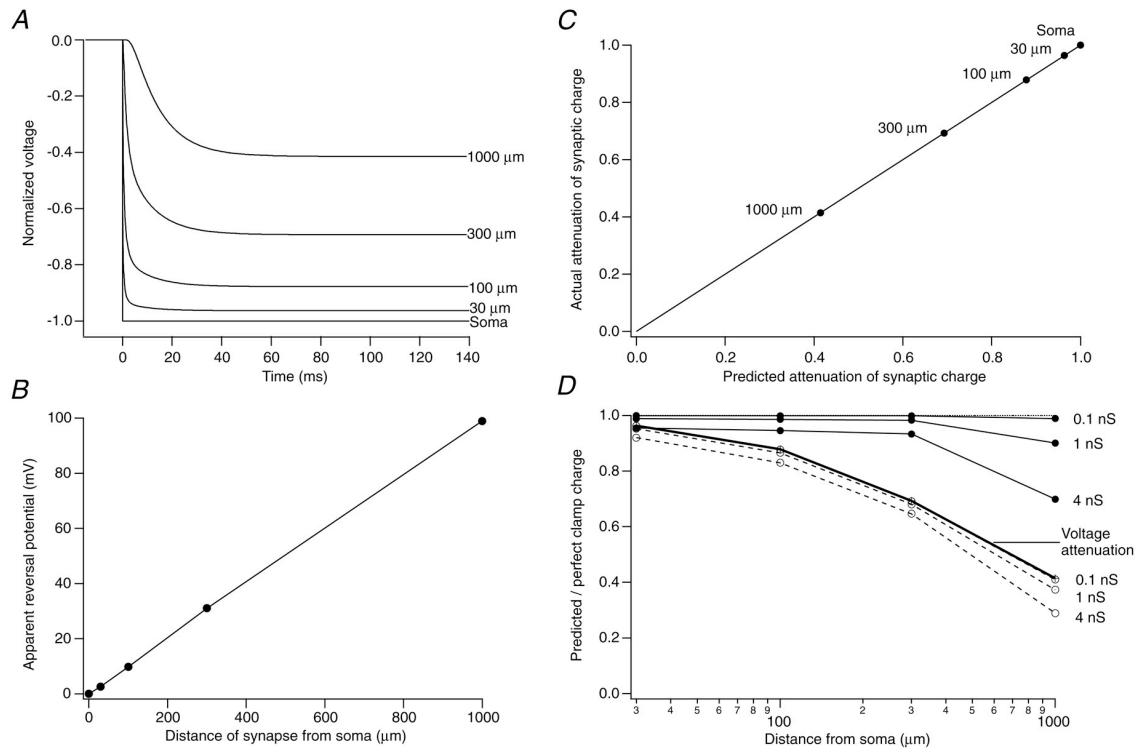


**Fig. 2.14.** Estimating the attenuation of synaptic charge. *A*, attenuation of voltage in response to a somatic voltage step at different locations in the synaptic tree. Same conditions and synapse locations as in Fig. 2.13. *B*, shift of apparent synaptic reversal potential with increasing distance of the synapse from the somatic recording site. The resting membrane potential of the neuron was  $-70$  mV, and the reversal potential of the synapse was set to 0 mV. *C* compares the attenuation of synaptic charge predicted from reversal potential shifts with the actual attenuation of the synaptic charge. The attenuation was predicted according to Eq. 2.11, and the actual charge attenuation was calculated by dividing the integral of current recorded at the soma by the integral of the current flowing at the synapse. Note that for synapses at all distances the predicted and actual values fall along the unity line. *D*, comparing predicted charge with charge associated with the perfectly-clamped EPSC. Each point represents the actual charge divided by the synaptic charge expected with perfect clamp for synapses at different locations, and for three different synaptic conductance amplitudes (0.1, 1.0, and 4.0 nS). The neuron was either held at the resting membrane potential, such that all synapses were isopotential ( $\bullet$ , solid lines), or the neuron was held 20 mV hyperpolarized to the apparent reversal potential for each synapse ( $\circ$ , dotted lines). The attenuation of steady-state voltage at the different synaptic locations is also shown (thick solid line).

corresponding shift in the apparent reversal potential of the synaptic current, shown in Fig. 2.14B. The steady-state attenuation factor  $\alpha$ , representing the attenuation of voltage from soma to synapse, can then be calculated according to the following equation (cf. Carnevale & Johnston, 1982; Rall & Segev, 1985)

$$\alpha = \frac{V_{\text{rest}} + E_{\text{rev}}}{V_{\text{rest}} + E_{\text{rev}} + \Delta E_{\text{rev}}} \quad (2.11)$$

where  $E_{\text{rev}}$  is the reversal potential of the synaptic conductance,  $\Delta E_{\text{rev}}$  is the shift in reversal potential from the expected value, and  $V_{\text{rest}}$  is the resting potential of the cell. Confirmation that the value of  $\alpha$  is identical to the attenuation of the charge associated with the synaptic current as it spreads from the synapse to the soma is provided in Fig. 2.14C, where at each synaptic location the attenuation predicted from the reversal potential shift is indistinguishable from the actual attenuation of the charge flowing at the synapse, as expected from cable theory.

As pointed out above, the synaptic charge predicted from reversal potential shifts will not be identical to the charge expected under perfect voltage clamp conditions because the voltage escape distorts the current flowing at the synapse by reducing its driving force (Fig. 2.13B,E). The magnitude of this error will depend on the size of the synaptic conductance and the electrotonic location of the synapse. This is shown in Fig. 2.14D, which compares the synaptic charge predicted from Eq. 2.11 with the synaptic charge expected under perfect voltage clamp, with synapses at different distances and with different peak conductances. If the synaptic current is recorded at the resting potential of the cell (see top traces), where the neuron is isopotential, then the predicted charge generally corresponds closely to the actual synaptic charge ( $\leq 10\%$  error for the most distal 1 nS synapses). As expected, the error depends on the magnitude of the synaptic conductance: as the conductance becomes smaller, the error converges towards zero. By contrast, when the neuron is not isopotential, then errors in the predicted charge can be considerable (see lower traces). This is because the voltage at the synapse deviates from the somatic voltage by a factor corresponding to  $\alpha$  (see thick trace for the expected voltage attenuation). Therefore, if the synaptic currents are recorded at voltages different from the holding potential, then the holding potential must also be corrected for  $\alpha$ . Note that remaining deviations from the voltage attenuation are attributable solely to the voltage escape.

The procedure described here, based on Eq. 2.11, provides a relatively accurate measure of synaptic charge in any neuronal geometry. Several assumptions must be met: 1) the neuron behaves passively; 2) the reversal potential of the synaptic current is known; 3) the resting potential is known; 4) the voltage escape must be relatively small. If these conditions hold, and the time course of the conductance is determined using the voltage jump method, then it is possible to provide an estimate of the peak amplitude of the conductance.

## 2.4 Discussion

Measuring the recovery of synaptic charge with a series of voltage jumps can provide several important pieces of information: charge recovered by jumps made before the onset of the synaptic conductance reveals the voltage change at the synapse in response to the voltage step, and charge recovered by jumps made after the onset of the synaptic conductance reveals the kinetics of the conductance. A simple analytical function is described which makes it possible to extract these features directly from experimental data, independent of the neuronal geometry and without the need to construct a compartmental model of the cell. This approach therefore circumvents the serious distortions in the kinetics of the synaptic current caused by space-clamp errors, and provides an index of the electrotonic location of the synapse. By combining the method with an estimate of charge attenuation it is possible in principle to reconstruct all aspects of the synaptic conductance waveform.

### 2.4.1 Comparison with previous approaches

Smith et al. (1967) used phase changes in a carrier sine wave applied at the soma to detect membrane impedance changes during EPSPs and IPSPs in motoneurons. Although this technique resolved the time course of conductance changes at proximal synapses, it was incapable of detecting distal conductance changes (as predicted theoretically by Rall, 1967). This is because the frequency of the carrier signal must be high to achieve sufficient time resolution, and consequently it rapidly attenuates as it spreads into the dendrites. An analogous method using a train of brief voltage jumps (see section 2.3.10) suffers from similar problems. In contrast, the present method uses a voltage transient with predominantly low-frequency components (the voltage step response) as a "windowing function" which is shifted in small steps over the synaptic conductance, conserving both high sensitivity to distal conductance changes and arbitrarily high time resolution. As a consequence of the need for multiple sweeps, the method cannot measure sweep-to-sweep fluctuations in conductance kinetics (see section 2.3.10), but instead reports the mean conductance time course of the active synapses.

Another approach (Johnston & Brown, 1983; Jonas et al., 1993; Spruston et al., 1993; Ulrich & Lüscher, 1993; Soltesz et al., 1995; see also Hestrin et al., 1990), is to estimate the filtering of synaptic currents using compartmental models of neurons. Given such estimates, it is possible in principle to determine the synaptic conductance time course by "working backwards" from the measured current with a compartmental model of the same neuron. Aside from the considerable time and effort which must be invested to construct such models, even the most carefully

conditioned models still suffer from problems of non-uniqueness in the model parameters (Major et al., 1994; Roth & Häusser, 2001). Furthermore, the location of the active synapses is usually unknown and is difficult to determine. Consequently the range of error estimates is relatively broad, even for synaptic connections where good estimates exist for the location of active synapses (Jonas et al., 1993). By contrast, the present method is independent of neuronal geometry, and thus requires no knowledge of the electrotonic structure of the neuron being recorded from (as long as care is taken to rule out major sources of error). However, combining the voltage jump approach with compartmental modelling may be very powerful, as discussed below.

Several groups have used the response to single voltage jumps at the soma, either alone (Llano et al., 1991) or interacting with a synaptic conductance (Hestrin et al., 1990; Isaacson & Walmsley, 1995; Sah & Bekkers, 1996) to estimate the filtering of synaptic currents (see also Silver et al., 1995). Llano et al. (1991) proposed that decay time constants of synaptic currents which were slower than the characteristic charging time constant of the distal compartment of juvenile Purkinje cells could be considered to be well clamped. Their two-compartment model is not, however, useful for synaptic conductances with decay kinetics similarly rapid to or faster than the charging time constant, and although it may be adequate for describing Purkinje cells at a particular developmental stage (see Roth & Häusser, 2001), it is unlikely to be applicable to other cell types. Somatic voltage jumps have also been used to either eliminate the driving force at the synapse (Isaacson & Walmsley, 1995; Sah & Bekkers, 1996) or activate  $Mg^{2+}$  block of NMDA receptors (Hestrin et al., 1990). The rate of the resulting relaxation in the somatic synaptic current ("switchoff") provides a measure of the electrotonic location of the synapse. However, to make quantitative predictions about the filtering of the synaptic current based on the switchoff, a compartmental model of the same cell is required (Sah & Bekkers, 1996).

Finally, it is possible to circumvent space-clamp problems using a direct approach: dendritic recording of synaptic currents (Häusser, 1994). As the clamp remains at a point, however, only synapses close to the dendritic recording site will be well-clamped. It is therefore necessary to activate synapses close to the recording electrode, or to select events based on their electrotonic proximity (Häusser, 1994). In principle one could combine dendritic voltage clamp recording with the voltage jump method to improve resolution of the most distal synaptic conductances.

## 2.4.2 Sources of error

The voltage jump method assumes that the synaptic conductance is identical from one jump to the next. Real synapses, however, display trial-to-trial variability in

amplitude and time course. This variability, along with other sources of experimental noise, introduces noise into the charge recovery curve. The cortical synapses studied here show considerable variability (Markram et al., 1997) and therefore averages of many individual sweeps are necessary to construct charge recovery curves with acceptable noise levels. A tradeoff is expected between noise in the charge recovery and problems associated with voltage escape: the larger the synaptic signal, the better the resolution of the method, but also the greater the risk that voltage escape may distort the synaptic current. If noise is a problem, then increasing the number of active synapses is not always the best solution; collecting more sweeps or increasing voltage jump amplitude are preferable.

When fitting charge recovery curves contaminated by noise several issues must be considered. First, deciding the number of exponential components required may be a problem, since separation of closely-spaced exponentials can be difficult even if the data are free of noise (Provencher, 1976). Changing the number of exponential components for one part of the curve can affect the relative amplitudes of other exponential components (cf. Eq. 2.10). Also, by assuming a monoexponential decay of the synaptic conductance when it is in fact biexponential, the "effective" single  $\tau_{\text{dec}}$  (see Major, 1993) may be overestimated. Second, estimates of  $\tau_{\text{rise}}$  may be associated with considerable uncertainty, especially if it is fast, since information about the risetime is contained in only a few points of the charge recovery curve. If the risetime is an important unknown parameter, then greater time resolution is needed around  $t = 0$  ms (i.e. more closely spaced jumps).

Even under the noise-free conditions of the simulations, the voltage jump method does not extract the time course of the synaptic conductance with perfect accuracy. The reason for this discrepancy is that the method measures the kinetics not of the synaptic current expected under perfect voltage clamp conditions, but rather of the actual current flowing at the synapse, which will be distorted due to voltage escape. The extent of voltage escape will therefore determine how well the kinetic parameters extracted by the method reflect those of the actual synaptic conductance. In simulations using models of neurons with realistic synaptic conductances, errors caused by voltage escape were relatively small (<10%). Nevertheless, voltage escape may represent a greater problem under certain conditions (see Fig. 2.7), for example when activating a large number of closely-spaced synapses. This can be assessed by applying a non-saturating dose of a non-competitive antagonist (or a competitive antagonist with slow dissociation kinetics) to reduce the size of the synaptic conductance. If the shape of the measured synaptic current does not differ after this treatment, then the effects of voltage escape can be safely neglected.

Active membrane conductances may also cause distortions in the charge recovery. The contribution of active conductances will depend primarily on their I-V relation; also if their activation kinetics are slow relative to the synaptic conductance kinetics, or if the channels are located distant from the synapses (e.g. in the axon), then their contribution will be less important. Interestingly, despite the distortions in the charge recovery observed in the neocortical pyramidal cell model, the synaptic conductance decay was relatively faithfully reported, indicating that under these conditions the decay of the synaptic conductance predominates. Nevertheless, to reliably fit Eq. 2.10 both the jumps and the synaptic current should demonstrate passive behavior. Non-linearities can be prevented or reduced either by inactivation, "washout" (e.g. of calcium conductances) or by applying intracellular blockers via the recording pipette; alternatively, non-saturating concentrations of antagonist can be used to reduce the size of the conductance (and thereby also the voltage escape).

### 2.4.3 Application to neocortical pyramidal cells

The voltage jump method was used to determine experimentally the time course of excitatory synaptic conductances in layer 5 neocortical pyramidal cells (Häusser & Roth, 1997). This was the first application of the method, and may serve as an example to show which experimental steps are involved. Whole-cell patch-clamp recordings were made from the soma of visually identified thick tufted layer 5 pyramidal cells in slices of rat neocortex as previously described (Stuart et al., 1993; Markram et al., 1997). Excitatory synaptic currents were evoked by a stimulation pipette filled with extracellular solution located 100 – 300  $\mu\text{m}$  from the soma of the neuron being recorded from, usually near its primary apical dendrite. Care was taken to select inputs without detectable polysynaptic contributions and with minimal "jitter" in the timing of individual currents. The evoked EPSCs resulted from the activation of only one or a few presynaptic fibres (peak amplitude,  $546 \pm 50$  pA at  $-70$  mV; mean  $\pm$  S.E.M.;  $n = 25$ ). EPSCs had an average 20–80% rise time of  $0.89 \pm 0.03$  ms (range, 0.55 – 1.20 ms) at  $-70$  mV, and their decay could be fit well using a single exponential function with a time constant of  $3.83 \pm 0.24$  ms (range, 2.1 – 6.3 ms). The linearity of the membrane between  $-70$  and  $-90$  mV was examined by recording the membrane currents in response to a series of depolarizing and hyperpolarizing voltage jumps of different amplitude starting from a holding potential of  $-80$  mV (Fig. 2.15A). When scaled by the jump amplitude, these currents superimposed well for jumps of different amplitude (Fig. 2.15B). To check for distortions in the EPSC caused by activation of voltage-gated conductances, the time course of the EPSC was compared at  $-70$  mV and  $-90$  mV. At  $-90$  mV, the 20–80% rise time was  $0.86 \pm$



0.04 ms ( $P = 0.07$ , paired  $t$ -test) and the decay time constant was  $3.74 \pm 0.22$  ms ( $P = 0.06$ ; see Fig. 2.15C–D). To confirm that activation of voltage-gated conductances did not affect the synaptic current, and to assess possible distortions caused by voltage escape, the synaptic conductance was reduced by application of a

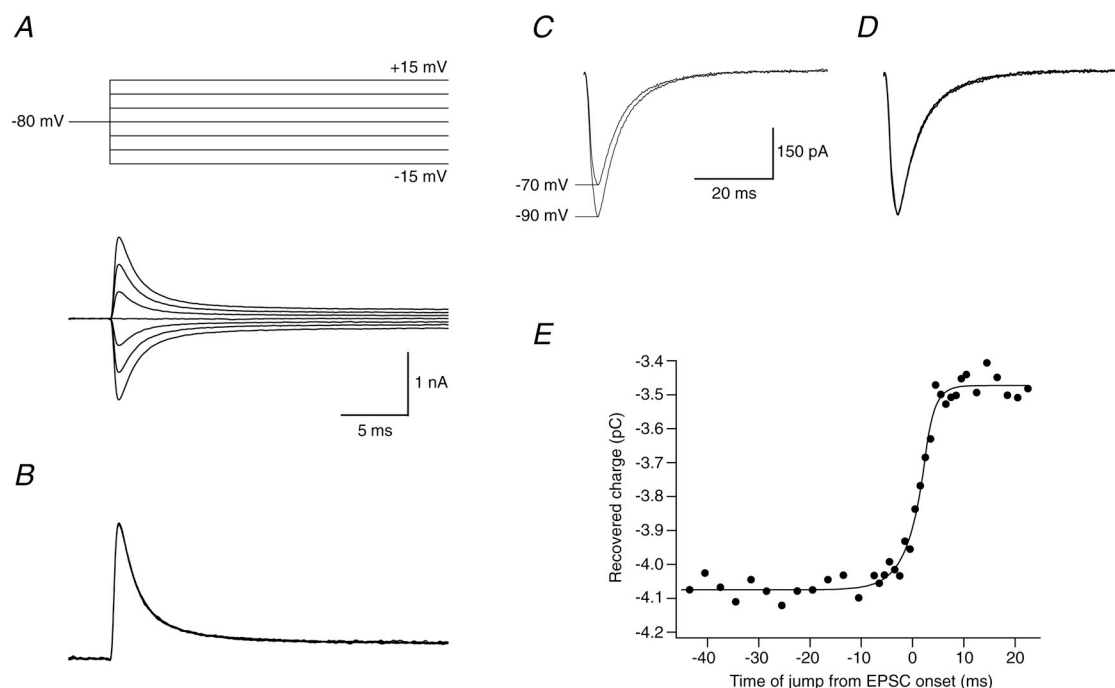


**Fig. 2.15.** Determining the time course of excitatory synaptic conductances in neocortical pyramidal neurons using the voltage jump method. All traces taken from a somatic whole-cell recording of a layer 5 neocortical pyramidal neuron at 35 °C; the internal solution contained 1 mM QX-314 and 0.5 mM ZD 7288. NMDA and GABA<sub>A</sub> receptors were blocked by bath application of 30  $\mu$ M D-APV, 50  $\mu$ M picrotoxin and 50  $\mu$ M bicuculline methiodide, and CaCl<sub>2</sub> and MgCl<sub>2</sub> were increased to 3 mM to reduce polysynaptic activity. In *A*, the neuron was held at  $-80$  mV and a series of voltage jumps (from  $-95$  mV to  $-65$  mV in steps of 5 mV) was given to test for membrane linearity, bracketing the voltage range used for determining the charge recovery. The resulting currents are shown below the voltage commands (average of 5 traces each; the series resistance of 6.0 M $\Omega$  was compensated by 90%). In *B* the currents were scaled by the command voltage and superimposed to demonstrate linearity. An EPSC was evoked by stimulation of afferent fibres near the apical dendrite and is shown at two different holding potentials in *C* (averages of 25 traces each). In *D* the traces in *C* have been scaled by their peak amplitudes and superimposed. The 20–80% rise times of the currents were 1.15 ms and 1.13 ms at  $-70$  mV and  $-90$  mV respectively, and the decay time constants were 6.2 and 6.1 ms respectively. The charge recovery curve obtained for this EPSC with jumps from  $-70$  mV to  $-90$  mV is shown in *E*. Each point represents the average of 21 – 26 separate trials. The values of the best fit using the analytical function (thick line) were  $\tau_v = 3.36$  ms,  $\tau_{rise} = 0.54$  ms and  $\tau_{dec} = 1.47$  ms. Fitting the decay of the charge recovery with a single exponential function gave  $\tau_{dec} = 1.59$  ms.

submaximal concentration (40  $\mu$ M) of the noncompetitive AMPA receptor antagonist GYKI 52466 (Paternain et al., 1995). While the peak amplitude of the EPSC at  $-70$  mV was reduced to  $24 \pm 3$  % ( $n = 3$ ) compared to control, the 20–80% rise time and decay time constant of the EPSC were  $106 \pm 2$  % ( $P = 0.08$ ) and  $108 \pm 9$  % ( $P = 0.4$ )

of the control values, respectively. These findings indicate that the EPSCs were not substantially distorted by voltage escape or by the activation of voltage-gated conductances.

The voltage jump protocol was applied using jumps between  $-70$  mV and  $-90$  mV. Jumps at different times relative to synaptic stimulation were interleaved, and a large number of individual sweeps were averaged for each jump time to reduce the contribution of noise associated with synaptic variability. The resulting charge recovery curves were fit with Eq. 2.10, as shown in Fig. 2.15E. Single-exponential functions provided a good fit to both the onset and the offset of the curve. Therefore, a single decay time constant of the synaptic conductance,  $\tau_{\text{dec}} = \tau_{\text{dec1}} = \tau_{\text{dec2}}$  was fitted, and it was usually necessary to constrain  $\tau_{\text{rise}}$  to  $0.1 - 0.6$  ms. The time constant of the voltage at the synapse was  $\tau_v = 2.93 \pm 0.44$  ms, and the decay time constant of the synaptic conductance was  $\tau_{\text{dec}} = 1.74 \pm 0.18$  ms ( $n = 8$ ). The S.E.M. predicted by Monte Carlo error analysis (Press et al., 1992; Gaussian noise was added to the charge recovery with mean experimental parameters and the resulting simulated charge recovery curves were fit by the same procedure as the experimental charge recovery curves) was  $0.24$  ms for  $\tau_v$  and  $0.28$  ms for  $\tau_{\text{dec}}$ .

The relatively rapid decay time course of the excitatory synaptic conductance in neocortical pyramidal cells estimated using the voltage jump method is consistent with recordings of selected spontaneous EPSCs (Stuart and Sakmann, 1995), assuming residual space clamp error in the latter measurements, as well as with the deactivation kinetics of AMPA-type glutamate receptor channels in these neurons (Hestrin, 1993; Jonas et al., 1994), correcting for temperature using a  $Q_{10}$  of  $\sim 2$  (Silver et al., 1996).

This result has important physiological implications. The decay of the EPSC largely determines the decay of the EPSP at its site of generation (Rall, 1967; Jack et al., 1983; Softky, 1994). The rapid decay of the conductance ensures that the time window for local synaptic integration in the dendritic tree remains brief, consistent with the proposed role of cortical pyramidal cells as coincidence detectors of synaptic input (Abeles, 1982; Softky, 1994; König et al., 1996; Brecht et al., 2003). It is also an important factor setting the level of background synaptic conductance *in vivo*. Neglecting the rising phase of the synaptic conductance, which is usually short compared to the decay phase, this is given by the number of synaptic contacts made onto a cell \* mean firing frequency of presynaptic axons \* mean release probability at a single synaptic contact \* decay time constant of the synaptic conductance \* peak synaptic conductance at a single contact. Assuming typical values for a layer 2/3 pyramidal neuron, this would be  $20000 * 1 \text{ Hz} * 0.3 * 1.7 \text{ ms} * 1 \text{ nS} = 10.2 \text{ nS}$  for

presynaptic axons firing at an average rate of 1 Hz, or 1.02 nS for a presynaptic firing rate of 0.1 Hz.

#### 2.4.4 Application to Bergmann glia cells

An important aim of synaptic physiology is to characterize the spatiotemporal profile of neurotransmitter concentration in and outside the synaptic cleft and its action on synaptic and extrasynaptic receptors. Dzubay & Jahr (1999) used AMPA receptors on Bergmann glia cells as sensors to measure the concentration of glutamate outside the synaptic cleft of the climbing fibre-Purkinje cell synapse. The stem fibre processes of Bergmann glia cells span the entire molecular layer of the cerebellum, giving rise to a large number of leaflike extensions which fill the space between neuronal dendrites and axons, and encapsulate synapses (Grosche et al., 2002). Thus, when using somatic recording to measure currents flowing through AMPA receptors located on a leaflike extension, close to a synapse but far from the soma of the Bergmann glia cell, one is faced with the same kind of space clamp problem as in neurons (see section 2.3.1). Dzubay & Jahr (1999) solved this problem by using the voltage jump method. In their experiments, the average decay time constant of the AMPA receptor-mediated current in Bergmann glia cells calculated by fitting the charge recovery curve with Eq. 2.10 was  $\tau_{\text{dec}} = 5.9 \pm 1.6$  ms (mean  $\pm$  S.D.;  $n = 7$ ). As expected, this was not significantly different from single exponential fits to the charge recovery curves starting 4 ms after the synaptic stimulation ( $5.8 \pm 1.4$  ms;  $P = 0.657$ , paired  $t$ -test;  $n = 7$ ). However, it was significantly faster than the decay time constant of the current recorded at the soma of the Bergmann glia cells ( $8.4 \pm 1.0$  ms;  $P = 0.004$ ;  $n = 7$ ), demonstrating that there is substantial filtering (42% slowing of the decay) as the current passes from the thin Bergmann glia processes to the soma. The time constant of the voltage response at the location of the activated AMPA receptors to a voltage clamp step at the soma was  $\tau_v = 4.4 \pm 1.9$  ms. Dzubay and Jahr then used the information obtained using the voltage jump method (i.e. the value of  $\tau_v$ , and the slowing of the decay of the current by 42%) to constrain a compartmental model of their Bergmann glial cells (see section 2.4.3), and corrected the space clamp error in their measured AMPA receptor responses using this compartmental model. They concluded that the extrasynaptic transmitter concentration seen by the glial processes reaches 160–190  $\mu\text{M}$ . Wadiche & Jahr (2001), in a study that also used the voltage jump method, estimated that the concentration of transmitter *within* the synaptic cleft of the same synapse peaks at 9.2 – 11.3 mM.

### 2.4.5 Application to hippocampal interneurons

Inhibitory interneurons of the CA3 stratum lucidum in the hippocampus receive excitatory synaptic input from two major sources: feedforward excitation from mossy fibres and feedback excitation from CA3 pyramidal cell axon collaterals. These two types of synapses are located across the entire dendritic tree of stratum lucidum interneurons, being only weakly segregated along the somatodendritic axis of the postsynaptic cells. Thus, it is not possible to distinguish them exclusively based on the rise time of the EPSC recorded at the soma. To characterize the kinetics of these two types of synaptic conductances, Walker et al. (2002) used the voltage jump method. First, they tested whether the voltage jump method was sensitive to changes in the kinetics of synaptic conductances in these cells by pharmacologically slowing the glutamate receptor-mediated synaptic conductance by aniracetam (5 mM). Indeed the decay time constant of the synaptic conductance extracted by fitting Eq. 2.10 to charge recovery curves collected before and after application of aniracetam increased by 336% ( $\tau_{\text{dec}} = 2.8 \pm 0.3$  ms (mean  $\pm$  S.E.M.;  $n = 12$ ) before versus  $\tau_{\text{dec}} = 12.2 \pm 1.5$  ms ( $n = 11$ ) after application of the drug;  $P < 0.0001$ , unpaired  $t$ -test). This experiment directly shows that the voltage jump method as applied in these cells was able to extract differences in the synaptic conductance time courses.

Next, Walker et al. (2002) measured the decay time course of the synaptic conductance at mossy fibre and CA3 pyramidal cell collateral synapses by stimulating them separately and fitting each charge recovery curve with Eq. 2.10. The average synaptic conductance time courses were  $\tau_{\text{dec}} = 1.57 \pm 0.18$  ms ( $n = 9$ ) and  $\tau_{\text{dec}} = 2.72 \pm 0.13$  ms ( $n = 16$ ;  $P < 0.0001$ , unpaired  $t$ -test), respectively. On the other hand, when proximal and distal CA3 pyramidal cell collateral synapses were evoked in alternation on the same neuron, the time constant of the voltage response at the location of the activated synapses was  $\tau_v = 0.6$  ms for proximal synapses and 3.5 ms for the distal input, while the decay time constants of the synaptic conductances were similar ( $\tau_{\text{dec}} = 2.6$  ms for proximal and 3.0 ms for distal synapses). Walker et al. (2002) concluded that these two types of afferent inputs to the same postsynaptic neuron show an overlap in the electrotonic location of the synaptic contacts they make, and that spatial segregation of synapses to different dendritic domains is not required for synapse-specific differential targeting of glutamate receptor subunits (for review see also Bischofberger & Jonas, 2002).

## 2.4.6 Application in cerebellar granule cells

In some happy dispositions the full analysis of the charge recovery curve is not even necessary. In small neurons such as cerebellar granule cells it is usually sufficient to plot the EPSC for different times of the somatic voltage jump with respect to the time of synaptic stimulation. If the (shifted) onset of the EPSC waveform after the voltage jump is much faster than the decay of the EPSC waveform, then the decay kinetics of the EPSC can be considered to be faithfully recorded, as is the case in granule cells (DiGregorio et al., 2002).

## 2.4.7 Future applications of the voltage jump method

The voltage jump method should be useful for determining the time course of synaptic conductances lacking appreciable voltage-dependence in any neuron where space-clamp is not guaranteed. The relative insensitivity of the method to membrane conductance and series resistance means that it could be used to measure the time course of synaptic conductances *in vivo*, where membrane conductance is higher (due to tonic synaptic activity) and where good space-clamp conditions are especially difficult to achieve. The method should also be useful for monitoring changes in synaptic conductance time course when space-clamp conditions are not constant, such as during development (cf. Kirson & Yaari, 1996) or during experiments on synaptic plasticity, where the series resistance usually increases over the course of the experiment. The method allows a direct test of the proposal that distal synaptic currents may have slower kinetics than proximal ones (Pearce, 1993), a mechanism which may compensate for electrotonic attenuation of distal inputs (Jack et al., 1981; Stricker et al., 1996).

The method is not restricted to examining synaptic conductances. The kinetics of any conductance which lacks appreciable voltage dependence, such as certain sodium-activated (Koh et al., 1994) or calcium-activated (Sah & Bekkers, 1996) potassium conductances, can also be determined. If the kinetics of the conductance are slightly voltage-dependent, then the measured values will be a blend of the time constants at the holding and jump voltages.

The ability of the method to estimate the time course of the voltage change at the conductance location in response to a somatic voltage step should be particularly useful, since it offers an index of the electrotonic distance of the conductance. This allows one to compare the relative electrotonic distance of different synapses (cf. Sah & Bekkers, 1996). Furthermore, since the time course of the voltage change at the synapse is known, one can estimate the physical distance of the synapses from

the recording site with a compartmental model of the same cell. Another possibility is to use arbitrary conductance changes to map the electrotonic structure of the dendritic tree. For example, focal application of neurotransmitter (to generate a conductance) could be combined with the voltage jump protocol to map the electrotonic geometry of the neuron in regions which may be inaccessible to direct recording, providing important constraints for compartmental models of such neurons. Finally, the method could also be used with arbitrary voltage command waveforms (as long as the response can be described by sums of exponentials). This may allow experimental measurements of the filtering experienced by physiologically relevant signals, such as action potentials and synaptic potentials, as they propagate in the dendritic tree.

## 3 Propagation of action potentials in dendrites depends on dendritic geometry

### 3.1 Introduction

The propagation of action potentials in the dendritic tree has been the subject of great interest for over a century, beginning with the speculations of Cajal (1904) on the directional flow of signals in neurites. Over the past few decades, evidence has accumulated to suggest that under most conditions, the sodium action potential (AP), the output signal of the neuron, is initiated in the axon and retrogradely invades the dendritic tree, a process known as backpropagation (reviewed by Stuart et al., 1997b). Backpropagation of APs has been demonstrated in a variety of different cell types *in vitro*, and evidence for backpropagation *in vivo* has been provided by recordings in both anaesthetized (Svoboda et al., 1997; Helmchen et al., 1999; Svoboda et al., 1999; Waters et al., 2003) and awake animals (Buzsaki & Kandel, 1998). APs can also be initiated in the dendrites under conditions of intense synaptic stimulation (Turner et al., 1991; Chen et al., 1997; Stuart et al., 1997a; Golding & Spruston, 1998; Kamondi et al., 1998; Martina et al., 2000; Larkum et al., 2001; Golding et al., 2002), and the spread of these dendritic APs towards the soma is known as forward propagation. Understanding the factors that determine the efficacy of AP propagation in dendrites is important since AP propagation has key consequences for the integration of synaptic input and the induction of synaptic plasticity (Johnston et al., 1996; Linden, 1999; Sjöström & Nelson, 2002). In particular, backpropagation of the AP provides a mechanism whereby information about neuronal output is signalled backwards to active synapses to trigger changes in synaptic strength (Markram et al., 1997b; Stuart et al., 1997b; Sjöström & Nelson, 2002).

A striking finding that has emerged from recent studies is that, under similar experimental conditions, systematic differences in backpropagation exist between neuronal types (reviewed by Stuart et al., 1997b; Fig. 3.1). The somatic AP propagates non-decrementally into the dendrites of dopamine neurons (Häusser et al., 1995) and the primary dendrites of mitral cells (Bischofberger & Jonas, 1997; Chen et al., 1997). On the other hand, many neuronal types show decremental conduction, with the most extreme example being cerebellar Purkinje cells, where the AP is reduced to a few millivolts in amplitude at 100  $\mu\text{m}$  from the soma (Llinas & Sugimori, 1980; Stuart & Häusser, 1994). A comparable diversity has also been observed for the efficacy of forward propagation of dendritically initiated APs towards

the soma (Llinas & Sugimori, 1980; Chen et al., 1997; Stuart et al., 1997a; Golding & Spruston, 1998; Kamondi et al., 1998; Martina et al., 2000; Larkum et al., 2001; Golding et al., 2002).

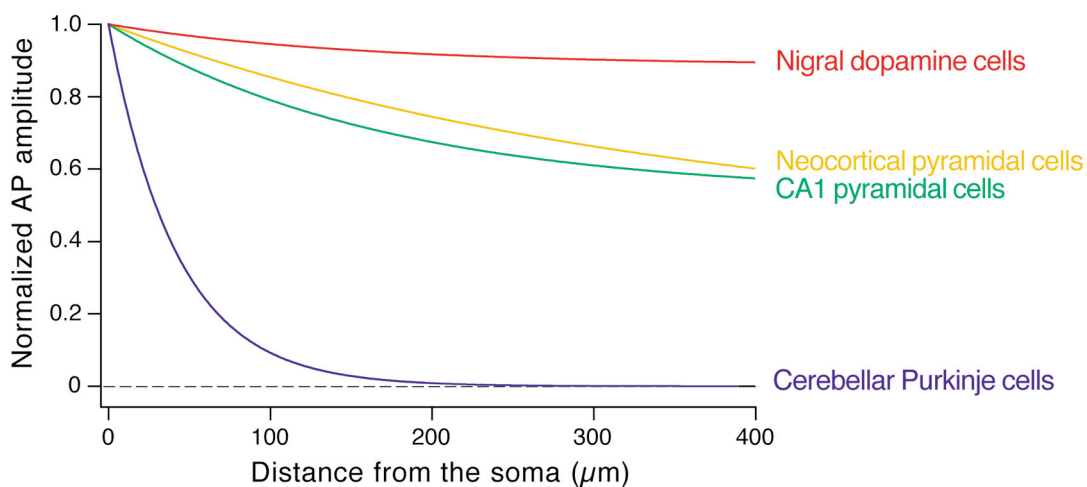


**Fig. 3.1.** Backpropagation of APs in dendrites depends on cell type. Dendritic action potential amplitude, normalized to the amplitude of action potentials at the soma, is plotted against the distance from the soma for neocortical layer 5 and hippocampal CA1 pyramidal neurons, cerebellar Purkinje cells and substantia nigra dopamine neurons. The best fit by a single exponential function to the experimental data in the different neuronal types is shown. Adapted from Stuart et al., 1997b.

Explanations for these systematic differences in the efficacy of propagation have concentrated on differences in the densities of dendritic voltage-gated channels (Stuart et al., 1997b; Magee et al., 1998). Theoretical work on AP propagation in axons has demonstrated that propagation is dependent on axonal geometry (Goldstein & Rall, 1974; Ramon et al., 1975; Parnas & Segev, 1979; Joyner et al., 1980; Lüscher & Shiner, 1990; Manor et al., 1991). The wide variety of dendritic arborizations among different neuronal types suggests that differences in dendritic geometry contribute to determining the extent of backpropagation and forward propagation of APs in dendrites. This is a difficult issue to address quantitatively, as cable theory does not provide an analytical solution describing action potential propagation in arbitrarily branched cable structures, and systematic experimental manipulations of dendritic geometry are not yet possible. Therefore I examined this question with simulations of AP propagation in a wide range of realistic dendritic geometries. By inserting the same set of passive and active, voltage-dependent conductances into compartmental models based on morphological reconstructions of each cell type, I isolated the effect of differences in dendritic geometry alone (Mainen & Sejnowski, 1996). I show that dendritic geometry is a key determinant of the efficacy of both forward and backpropagation of APs. These results have important implications for modulation of backpropagation and for the role of the dendritic AP as an associative signal in different neurons.



## 3.2 Methods

### 3.2.1 Dendritic geometries

Detailed three-dimensional reconstructions of 42 neurons were used. Two rat Purkinje cells, two rat neocortical layer 5 pyramidal neurons, and four rat substantia nigra dopamine neurons were filled with biocytin and digitally reconstructed using a 100X oil immersion objective (1.4 NA) on a Zeiss Axioplan (Zeiss, Oberkochen, Germany) in conjunction with NeuroLucida software (MicroBrightField, Colchester, VT, USA). Three rat layer 5 pyramidal neurons were from G. Stuart and N. Spruston, and one from D. Smetters; three guinea pig Purkinje cells were from M. Rapp and I. Segev; rat CA1/CA3 pyramidal cells, and DG interneurons and granule cells were obtained from the Duke-Southampton Neuronal Morphology Archive ([www.neuro.soton.ac.uk](http://www.neuro.soton.ac.uk)). Reconstructions were inspected carefully, and only those without apparent errors in connectivity or dendritic diameters were used. All dendrites were divided into compartments with a maximum length of  $7 \mu\text{m}$ . Spines were incorporated where appropriate by scaling membrane capacitance and conductances (Shelton, 1985; Holmes, 1989).

### 3.2.2 Compartmental models

Simulations were performed using the NEURON simulation environment (Hines & Carnevale, 1997) on a Silicon Graphics Origin 2000 server. The time step for the simulations was  $25 \mu\text{s}$ . The structure of the model of active conductances was based on recent modelling studies (Mainen et al., 1995; Mainen & Sejnowski, 1996; Rapp et al., 1996). Two Hodgkin–Huxley-type conductances ( $g_{\text{Na}}$  and  $g_{\text{K}}$ ) were inserted into the soma, dendrites and spines at uniform densities. For simplicity, the consequences of using spines with different excitability from dendritic shafts (see Baer & Rinzel, 1991) were not explored. The model was tuned by attaching a synthetic axon (Fig. 3.2; Mainen et al., 1995) to five neocortical pyramidal cell geometries, in which backpropagating APs were initiated by somatic current injection. Active and passive membrane parameters were then optimized to reproduce experimental data on AP backpropagation from these neurons in slices taken from rats aged P26–30 (Stuart et al., 1997a). The uniform passive parameters of the model were  $R_i = 150 \Omega \text{ cm}$ ,  $C_m = 1 \mu\text{F cm}^{-2}$ ,  $R_m = 12 \text{ k}\Omega \text{ cm}^2$ , which reproduced experimental values for membrane time constant and input resistance to within 10% (Stuart et al., 1997a; Stuart & Spruston, 1998). The standard values for  $g_{\text{Na}}$  and  $g_{\text{K}}$  were 35 and 30 pS  $\mu\text{m}^{-2}$ , respectively, and the channel models were identical to

those used by Mainen & Sejnowski (1996; available from [www.cnl.salk.edu/CNL/simulations.html](http://www.cnl.salk.edu/CNL/simulations.html)). Channel kinetics and densities were adjusted for a nominal temperature of 37°C using a  $Q_{10}$  of 2.3. All results shown in the figures and tables were obtained using this standard model. In some cases the standard  $g_{Na}$  and  $g_K$  were replaced by corresponding channel models from a different study (Paré et al., 1997). Simulations using a non-uniform distribution of the A-type  $K^+$  channel were based on previous studies (Hoffman et al., 1997; Migliore et al., 1999). The A-type  $K^+$  channel replaced the  $K^+$  channel used in the standard model, and its density was scaled to increase linearly 5-fold from the soma to the most distal dendrites of each neuron, with the initial density being 480  $\text{pS } \mu\text{m}^{-2}$  (Hoffman et al., 1997; Migliore et al., 1999).

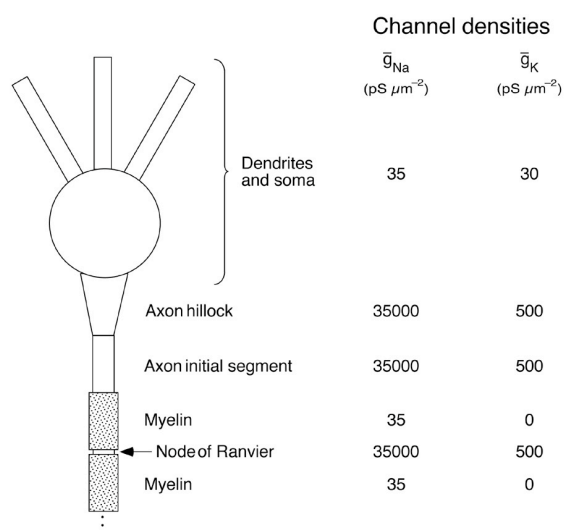


**Fig. 3.2.** Standard densities of voltage-gated conductances used in the simulations of AP propagation. A synthetic axon (Mainen et al., 1995) with high densities of voltage-gated channels ensuring axonal initiation of APs was attached to the soma in some initial simulations (see section 3.2.2). However, the axon was removed in subsequent simulations (Figs. 3.3–3.10) in which a somatic or dendritic AP waveform was imposed on the cell by voltage clamp, to ensure equal initial conditions for action potential propagation in each cell.

The geometry of the soma and proximal dendrites may itself affect the invasion of the soma by the axonally initiated AP. Therefore, a somatic AP waveform (amplitude, 96 mV; half-width, 0.6 ms) obtained from one of the pyramidal neuron reconstructions with the standard model was used as a voltage clamp command at the soma of all other neurons to simulate backpropagation. This ensured a fair comparison across all neurons, so that backpropagation in the dendrites starts from the same initial conditions in the soma in each reconstruction (simulations with a synthetic axon attached to all morphological reconstructions, allowing each to generate its own AP, produced very similar results). The dendritically initiated AP was generated using a biexponential synaptic conductance ( $\tau_{\text{rise}} = 0.2$  ms,  $\tau_{\text{dec}} = 1.7$  ms,  $g_{\text{max}} = 50$  nS) near the apical nexus of a neocortical pyramidal cell (622  $\mu\text{m}$  from the soma; see Fig. 3.8). This waveform was used as a voltage clamp command to examine propagation of a dendritic AP, again in order to ensure that propagation begins from the same initial conditions. In this way, AP propagation was isolated from

AP initiation, conditions for which also depend on dendritic geometry (Segev & Rall, 1998). Similar results were obtained using a somatic AP waveform, or a backpropagating dendritic AP waveform.

### 3.2.3 Measurements

The rate of increase of membrane area as a function of distance from the soma ( $dA/dx$ ) was approximated by  $\Delta A/\Delta x$ , where  $\Delta A$  is the spine-adjusted total membrane area at a distance interval  $[x, x + \Delta x)$  from the soma. The discretization  $\Delta x$  was  $1 \mu\text{m}$  ( $\Delta x = 0.25 \mu\text{m}$  for Purkinje cells). All distances were measured along the dendrites. The somatodendritic  $\text{Na}^+$  channel density threshold for full AP propagation into all dendritic branches,  $g_{\text{Na},\text{thresh}}$ , was determined using the bisection algorithm (Press et al., 1992). The radius of equivalent cables was calculated according to the following equation,

$$r_{\text{eq}}(X) = \left( \sum_j r_j(X)^{3/2} \right)^{2/3} \quad (3.1)$$

where the sum is over all dendritic segments  $j$  located at a given electrotonic distance  $X$  from the soma (Fleshman et al., 1988; Clements & Redman, 1989; Ohme & Schierwagen, 1998), with discretization  $\Delta X = 0.004$ . Impedance mismatch at a given point in a reconstructed neuron was calculated by splitting the reconstruction into two subtrees at that point and measuring the input impedances (at a frequency of 200 Hz) of the two individual subtrees. Input impedances were calculated using the standard values of the passive parameters and  $g_{\text{Na}}$  and  $g_{\text{K}}$ . The impedance mismatch was then calculated as the ratio of the input impedance of the subtree where the AP originated over the input impedance of the subtree that the AP is propagating into. Correlations were assessed using the Pearson correlation coefficient  $r$ ; correlations mentioned in the text and shown in the figures are highly significant ( $P < 0.001$ ). Values are given as mean  $\pm$  S.E.M.

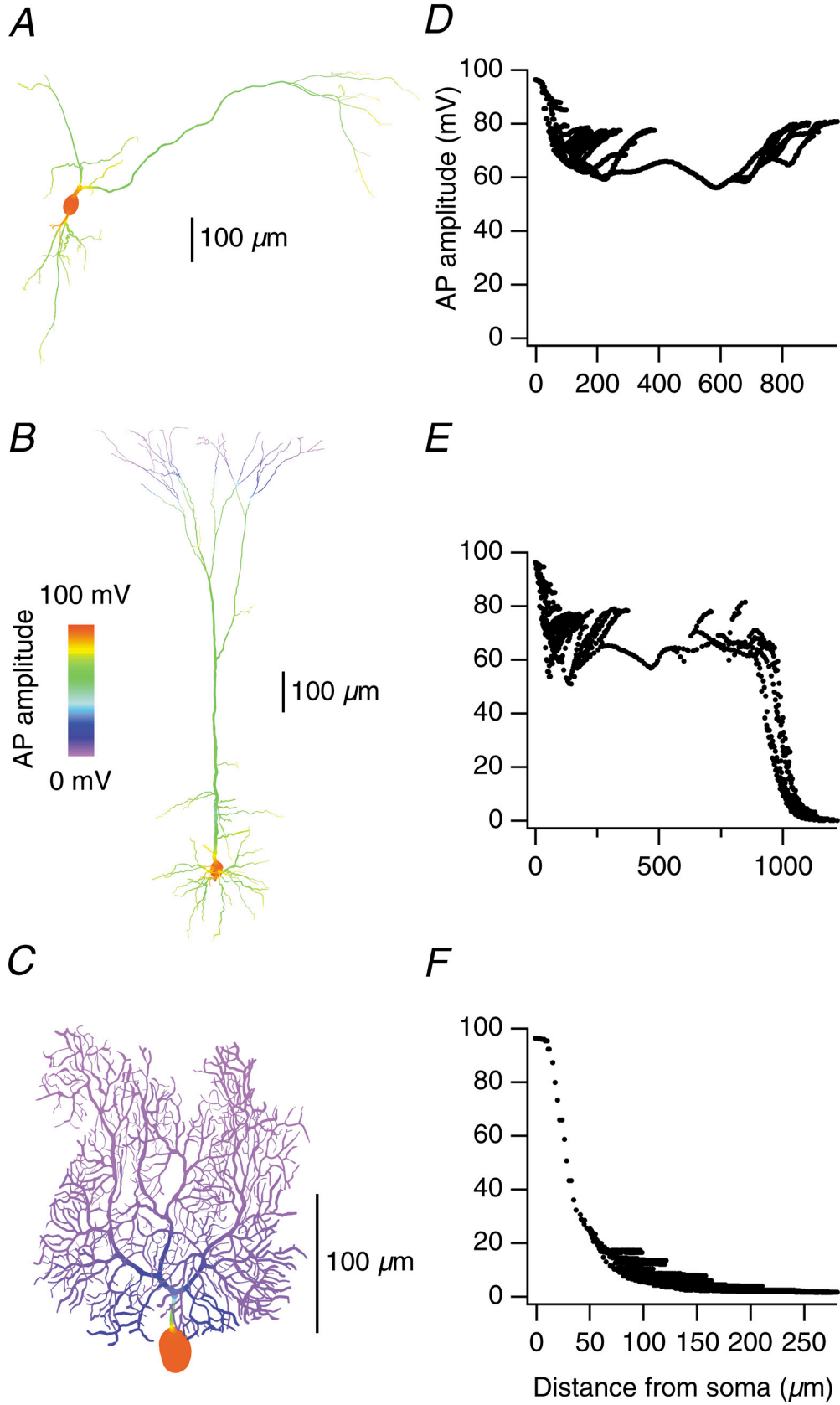
## 3.3 Results

### 3.3.1 Action potential backpropagation depends on dendritic geometry

A simple model of active conductances was designed to reproduce experimental data on AP backpropagation in a single cell type, in order to be then applied to a range of morphological reconstructions of different cell types. A model of neocortical pyramidal cells was chosen since extensive experimental data on backpropagation is available for this cell type. Furthermore, these neurons fall in the middle of the range of backpropagation efficacies (Stuart et al., 1997b; Fig. 3.1). The model was based on previous studies (Mainen et al., 1995; Mainen & Sejnowski, 1996; Rapp et al., 1996), and incorporated a uniform density of Na<sup>+</sup> and K<sup>+</sup> channels in the soma and dendrites, with a high density of Na<sup>+</sup> channels in the axon (Fig. 3.2) to ensure axonal initiation of the AP. This simple model is able to reproduce the experimental data in neocortical pyramidal cells remarkably well (cf. Fig. 1B and Fig. 2A of Stuart et al., 1997a).

To isolate the effect of dendritic geometry, the same model of active conductances was then inserted into morphological reconstructions of different cell types, and backpropagation of a somatic AP waveform was simulated. With identical channel types and densities, the different dendritic geometries produced very different patterns of backpropagation (Fig. 3.3), which reproduced the experimentally observed results in these neurons (Llinas & Sugimori, 1980; Stuart & Häusser, 1994; Stuart & Sakmann, 1994; Häusser et al., 1995; Stuart et al., 1997a). Thus, the AP spread effectively into all dendritic branches of substantia nigra dopamine neurons, while propagating decrementally in the apical dendrite of neocortical pyramidal cells, and failing to effectively invade the dendritic tree of Purkinje cells. Interestingly, even within the same neuron a wide range of AP amplitudes could be observed at the same geometric distances from the soma (Fig. 3.3B). As the density of Na<sup>+</sup> and K<sup>+</sup> channels is uniform in this model, the diversity of propagation into different dendritic branches must be a consequence of the dendritic geometry. Taken together, these findings indicate that dendritic geometry determines the functional relationship between Na<sup>+</sup> channel density and AP backpropagation.

**Fig. 3.3** → Backpropagation of APs in different dendritic geometries with identical channel types and distributions. *A-C*, Two-dimensional projections of three-dimensional morphological reconstructions of a substantia nigra dopamine neuron (*A*), a neocortical layer 5 pyramidal cell (*B*), and a cerebellar Purkinje cell (*C*). The local amplitude of a backpropagating AP elicited by voltage-clamping the soma with a standard somatic AP waveform is coded by color. *D-F*, Scatter plots of dendritic AP amplitude vs. distance from the soma for the cells shown in *A-C*. Each point represents the peak AP amplitude in each dendritic compartment.



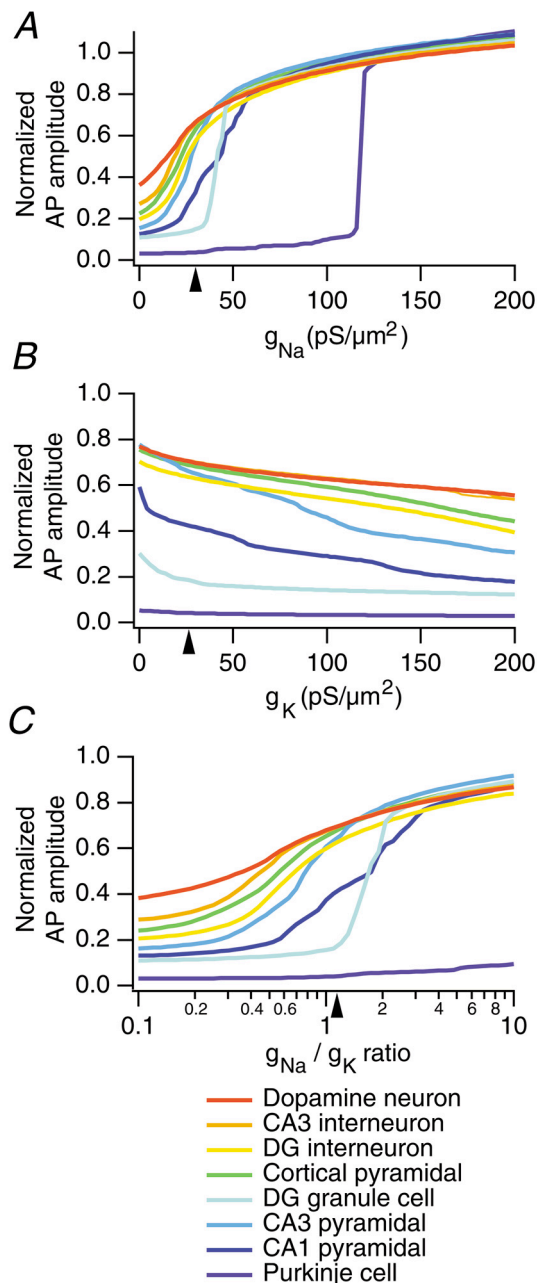


**Fig. 3.4.** Sensitivity of backpropagation to voltage-gated channel density in different cell types. *A*, Effect of varying  $Na^+$  channel density on backpropagation. The results of simulations in eight representative neurons from different cell types are shown, with cell type coded by color (legend below). The average dendritic AP amplitude at  $200 \mu m$  from the soma (normalized by the somatic AP amplitude) is plotted versus somatodendritic  $Na^+$  channel density. Somatodendritic  $K^+$  channel density was kept fixed at  $30 pS \mu m^{-2}$ . The arrowhead indicates the  $Na^+$  channel density used in the standard model (see section 3.2.2). *B*, Effect of varying  $K^+$  channel density. Simulations as in *A*, except somatodendritic  $K^+$  channel density was varied while keeping  $Na^+$  channel density constant at  $35 pS \mu m^{-2}$ . The arrowhead indicates the  $K^+$  channel density used in the standard model. *C*, Effect of varying the relative density of  $Na^+$  and  $K^+$  channels. Simulations as in *A*, except the ratio of somatodendritic  $K^+$  and  $Na^+$  channel density was varied, while keeping the sum of the channel densities constant at  $65 pS \mu m^{-2}$ . The arrowhead indicates the channel density ratio used in the standard model.

### 3.3.2 Sensitivity of backpropagation to modulation of channel densities in different dendritic geometries

To investigate the relationship between backpropagation and voltage-gated channel density in different dendritic geometries, backpropagation was simulated for a wide range of  $Na^+$  and  $K^+$  channel densities (from 0 to  $200 pS \mu m^{-2}$ ). These simulations were carried out in a large sample of morphological reconstructions of different neuronal types, including the neurons studied in section 3.3.1 above, as well as hippocampal CA1 and CA3 pyramidal neurons, dentate gyrus (DG) granule cells, and hippocampal interneurons. First, the  $Na^+$  channel density was varied while the

K<sup>+</sup> channel density was kept constant. Each neuronal type had a characteristic relation between dendritic Na<sup>+</sup> channel density and backpropagation (quantified by measuring the AP amplitude 200  $\mu\text{m}$  from the soma; Fig. 3.4A). With no dendritic Na<sup>+</sup> channels, the attenuation of the AP waveform was very different in different neuronal types (see Table 3.1). This indicates that the different dendritic trees filter the AP waveform to different extents even when backpropagation is passive. When Na<sup>+</sup> channel density was increased, an approximately sigmoid relationship was observed between density and propagation efficacy in most cell types. The half-maximum of these curves was typically around 20 – 40 pS  $\mu\text{m}^{-2}$  (see Table 3.1), within the physiological range of dendritic Na<sup>+</sup> channel densities (Johnston et al., 1996). In striking contrast, backpropagation in Purkinje cells was essentially insensitive to increases in Na<sup>+</sup> channel density over a wide range, with a sharp threshold leading to full backpropagation being reached only at very high densities (mean half-maximum  $92.8 \pm 23.3$  pS  $\mu\text{m}^{-2}$ ).

**Table 3.1.** Dependence of AP backpropagation on voltage-gated channel density in different neuronal types

| Cell type               | n | Passive AP backpropagation ratio <sup>a</sup> | Half-maximal $g_{\text{Na}}$ (pS $\mu\text{m}^{-2}$ ) <sup>b</sup> | Half-maximal $g_{\text{Na}}/g_{\text{K}}$ ratio <sup>c</sup> |
|-------------------------|---|---|--|--|
| Purkinje cell           | 5 | $0.06 \pm 0.01$                               | $92.8 \pm 23.3$  | $2.15 \pm 0.41$  |
| CA1 pyramidal cell      | 4 | $0.14 \pm 0.01$                               | $37.7 \pm 2.6$   | $1.30 \pm 0.18$  |
| CA3 pyramidal cell      | 5 | $0.16 \pm 0.01$                               | $31.6 \pm 1.8$   | $0.97 \pm 0.04$  |
| DG granule cell         | 6 | $0.14 \pm 0.02$                               | $33.5 \pm 2.1$   | $1.11 \pm 0.15$  |
| Cortical pyramidal cell | 5 | $0.21 \pm 0.01$                               | $21.4 \pm 2.6$   | $0.68 \pm 0.05$  |
| DG interneuron          | 6 | $0.25 \pm 0.03$                               | $22.4 \pm 1.5$   | $0.72 \pm 0.06$  |
| CA3 interneuron         | 5 | $0.30 \pm 0.03$                               | $20.9 \pm 3.1$   | $0.74 \pm 0.10$  |
| Dopamine neuron         | 4 | $0.27 \pm 0.04$                               | $19.2 \pm 1.2$   | $0.64 \pm 0.03$  |

<sup>a</sup> Amplitude of dendritic AP 200  $\mu\text{m}$  from the soma, normalized by somatic AP amplitude, with zero  $g_{\text{Na}}$  (conditions as in Fig. 3.4A).

<sup>b</sup> Density of somatodendritic Na<sup>+</sup> channels at which half-maximal AP backpropagation occurs (conditions as in Fig. 3.4A).

<sup>c</sup> Ratio  $g_{\text{Na}}/g_{\text{K}}$  at which half-maximal AP backpropagation occurs (conditions as in Fig. 3.4C).

Next, the density of dendritic K<sup>+</sup> channels was varied while maintaining a constant Na<sup>+</sup> channel density. As expected, when K<sup>+</sup> channel density was increased,

backpropagation became less effective. Although backpropagation was less sensitive to changes in dendritic  $K^+$  channel density than changes in  $Na^+$  channel density, there was a characteristic relationship between  $K^+$  channel density and backpropagation in each neuronal type (Fig. 3.4B). Over the range studied (from 0 to  $200 \text{ pS } \mu\text{m}^{-2}$ ) backpropagation in Purkinje cells and dopamine neurons showed little sensitivity to changes in  $K^+$  channel density, while backpropagation in pyramidal neurons and dentate gyrus granule cells was clearly affected (Fig. 3.4B).

In the same set of neurons, I also examined the sensitivity of backpropagation to changes in the *relative* densities of dendritic  $Na^+$  and  $K^+$  channels. This was done by systematically varying the ratio of densities over a wide range (0.1 to 10), while keeping the total voltage-gated channel density fixed. As shown in Fig. 3.4C, most neurons showed a sigmoid relationship with backpropagation efficacy as the density of  $Na^+$  channels relative to  $K^+$  channels was increased. However, the half-maximum of the curve depended strongly on dendritic geometry, and spanned a wide range (Table 3.1). Again, Purkinje cells were particularly insensitive to changes in dendritic channel densities. These findings demonstrate that, as expected, backpropagation depends on the relative density of dendritic voltage-gated  $Na^+$  and  $K^+$  channels. However, the same ratio of channel densities produces very different degrees of backpropagation in different dendritic geometries. Furthermore, the effect of changing the relative density depends critically on the dendritic geometry.

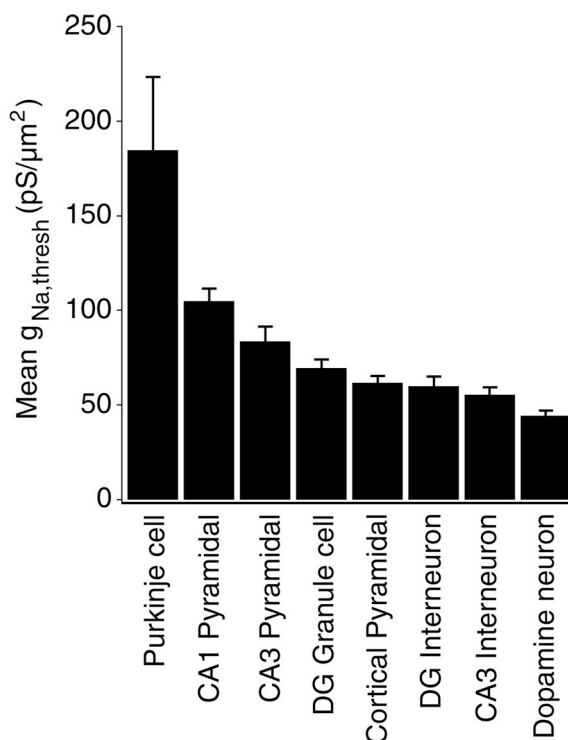


**Fig. 3.5.** Cell type-specific dependence of backpropagation on  $Na^+$  channel density. Bar chart of the minimum somatodendritic  $Na^+$  channel density required for full AP backpropagation (membrane potential  $> 0 \text{ mV}$ ) into all dendritic branches in different neuronal types. Each cell type is represented by at least 4 morphological reconstructions.



On the basis of these simulations, which single variable could serve as an index of the efficacy of backpropagation in the different dendritic geometries? As backpropagation is most sensitive to the Na<sup>+</sup> channel density (Fig. 3.4A), the minimum Na<sup>+</sup> channel density required for full backpropagation of the AP (peak membrane potential > 0 mV) into all dendritic branches appeared to be a good candidate. Indeed this threshold Na<sup>+</sup> channel density ( $g_{\text{Na,thresh}}$ ) varied widely across cell types (Fig. 3.5). Purkinje cells required nearly five times higher Na<sup>+</sup> channel density than dopamine neurons to sustain full backpropagation into all dendrites. Thus, in the following simulations  $g_{\text{Na,thresh}}$  is used as a measure of the efficacy of propagation in a given neuron.

### 3.3.3 Morphological determinants of backpropagation

Which morphological features are most important for determining the efficacy of backpropagation? Unfortunately, no analytical theory exists to predict whether propagation will be successful given a dendritic geometry and a set of realistic channel densities and kinetics (Jack et al., 1983). Attempts to formulate such a theory have so far succeeded only for simple geometries, using highly simplified models of excitability (Pastushenko et al., 1969; Pauwelussen, 1982). However, correlations between individual geometric parameters and our functional index of backpropagation,  $g_{\text{Na,thresh}}$ , or the amplitude of the AP 200  $\mu\text{m}$  from the soma ( $\text{AP}_{200}$ ) – using the standard parameters of the model – can be examined. The simplest morphological features, such as mean dendritic diameter, total geometric or electrotonic length of the dendrites, dendritic taper or flare, and total dendritic membrane area only correlated relatively weakly with  $g_{\text{Na,thresh}}$  or  $\text{AP}_{200}$  ( $|r| \leq 0.6$ ). The number of dendritic branchpoints, however, showed a strong relationship with the functional parameters across the population (Fig. 3.6A;  $r = 0.81$  and  $-0.73$  for  $g_{\text{Na,thresh}}$  and  $\text{AP}_{200}$  respectively). The range of branching densities was reflected in striking differences in the distribution of dendritic membrane area with distance  $x$  from the soma ( $dA/dx$ , Fig. 3.6B). Both  $g_{\text{Na,thresh}}$  and  $\text{AP}_{200}$  were strongly correlated with the maximum slope of  $dA/dx$  across the different morphological reconstructions (Fig. 3.6C). Combining features of the  $dA/dx$  distribution with another geometric parameter (e.g. the maximum slope normalized to the number of branchpoints or mean dendritic diameter) further strengthened correlations with  $g_{\text{Na,thresh}}$  and  $\text{AP}_{200}$ , such that correlation coefficients of  $|r| > 0.9$  were obtained.

The robustness of these correlations was tested in several ways. First, each of the passive parameters was changed over a wide range ( $R_i$ , 70 – 200  $\Omega\text{ cm}$ ;  $C_m$ , 0.7

–  $1.5 \mu\text{F cm}^{-2}$ ;  $R_m$ ,  $5 - 50 \text{ k}\Omega \text{ cm}^2$ ). Second, different models for the Hodgkin–Huxley-type  $g_{\text{Na}}$  and  $g_{\text{K}}$  conductances (taken from Paré et al., 1998) were incorporated. The qualitative behaviour of the models remained robust under these

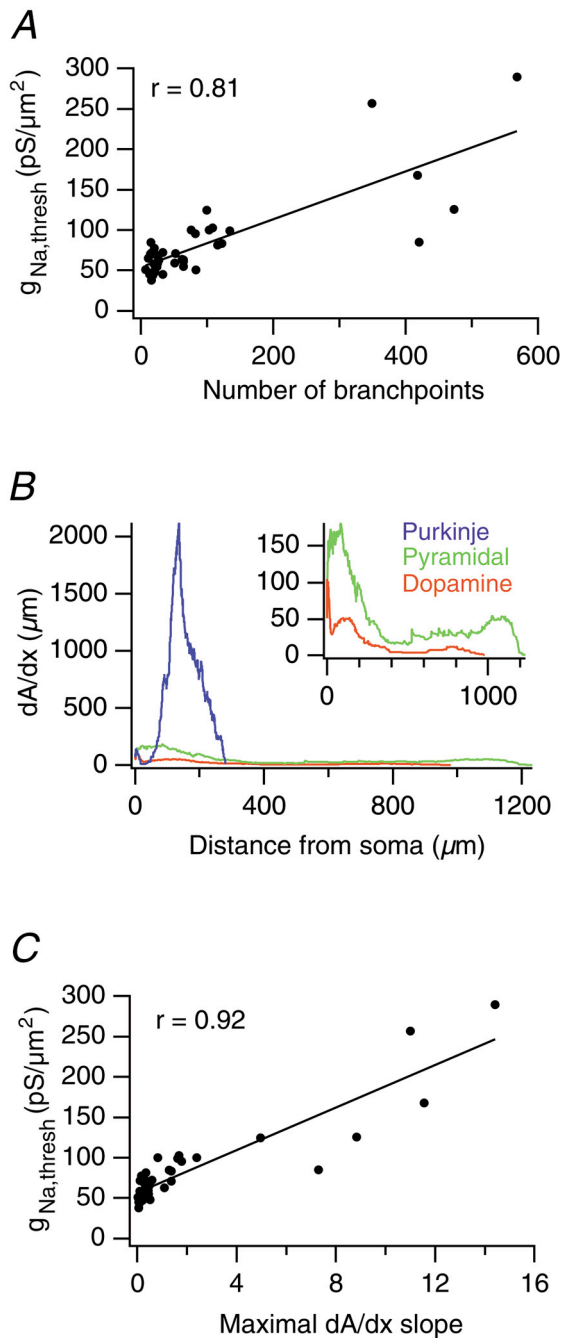


**Fig. 3.6.** Morphological determinants of backpropagation. *A*, Relationship between the number of dendritic branchpoints and  $g_{\text{Na,thresh}}$ . Each point represents one neuron ( $n = 42$  neurons). *B*, Rate of increase in membrane area with distance from the soma ( $dA/dx$ ) in a nigral dopamine neuron (red), a neocortical pyramidal cell (green), and a Purkinje cell (blue); same cells as in Figs. 3.3 and 3.4. The inset shows the data for the pyramidal cell and the dopamine cell on an expanded axis. *C*, Relationship between the maximum slope of the smoothed  $dA/dx$  distribution and  $g_{\text{Na,thresh}}$ .

different conditions, as did the ranking of correlations between dendritic geometry and backpropagation; values of individual correlations varied by less than 20%. Finally, as a non-uniform distribution of A-type  $\text{K}^+$  channels has recently been shown to be involved in regulating backpropagation in hippocampal pyramidal neurons (Hoffman et al., 1997) and mitral cells (Schoppa & Westbrook, 1999; Christie & Westbrook, 2003), a non-uniform distribution of an A-type  $\text{K}^+$  channel model (Migliore et al., 1999) was incorporated into the simulations based on experimental and

modelling studies (Hoffman et al., 1997; Migliore et al., 1999). Even with this non-uniform channel distribution, strong correlations were observed between dendritic geometry and backpropagation (e.g.  $r = 0.91$  for  $g_{Na,thresh}$  and the maximum slope of  $dA/dx$ ). Taken together, these findings suggest that geometric parameters alone can be used to estimate the relative efficacy of backpropagation in a given dendritic tree.

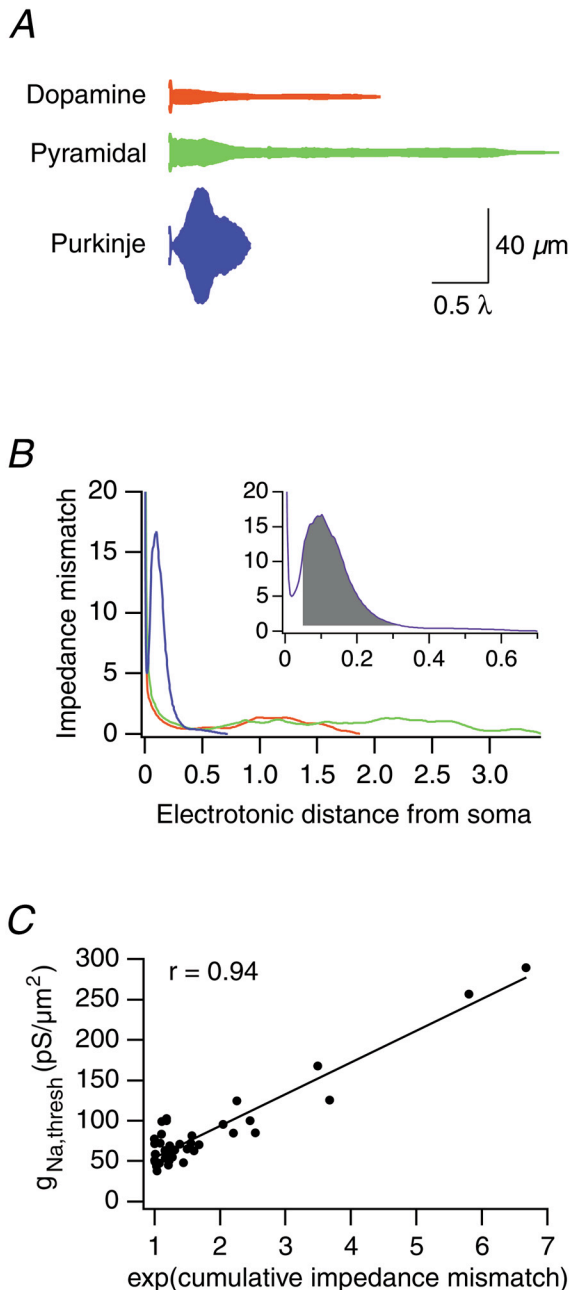


**Fig. 3.7.** A reduced model of dendritic geometry predicts the efficacy of backpropagation. **A**, Profiles of equivalent cables constructed from the cells shown in Fig. 3.3. The vertical axis corresponds to the radius of the equivalent cable, and the horizontal axis to the electrotonic distance ( $\lambda$ , electrotonic space constant). **B**, Impedance mismatch as a function of electrotonic distance from the soma for the equivalent cables shown in **A**. The cumulative impedance mismatch is defined by the area shown for the Purkinje cell in the inset (integral bounded by  $X = 0.05$  on the left to exclude the soma, and an impedance mismatch of 1.0 at the bottom). **C**, Relationship between the cumulative impedance mismatch in the equivalent cable (scaled exponentially) and  $g_{Na,thresh}$  in the respective original dendritic geometry.

Which measure provides the best functional link between the details of dendritic geometry and backpropagation efficacy? Simulations of AP propagation in axons (Goldstein & Rall, 1974; Lüscher & Shiner, 1990; Manor et al., 1991) have shown that propagation across a branchpoint depends on the ratio of the input impedances of the parent and daughter branches – the impedance mismatch (Goldstein & Rall, 1974). If this ratio equals one, there is no change in propagation of

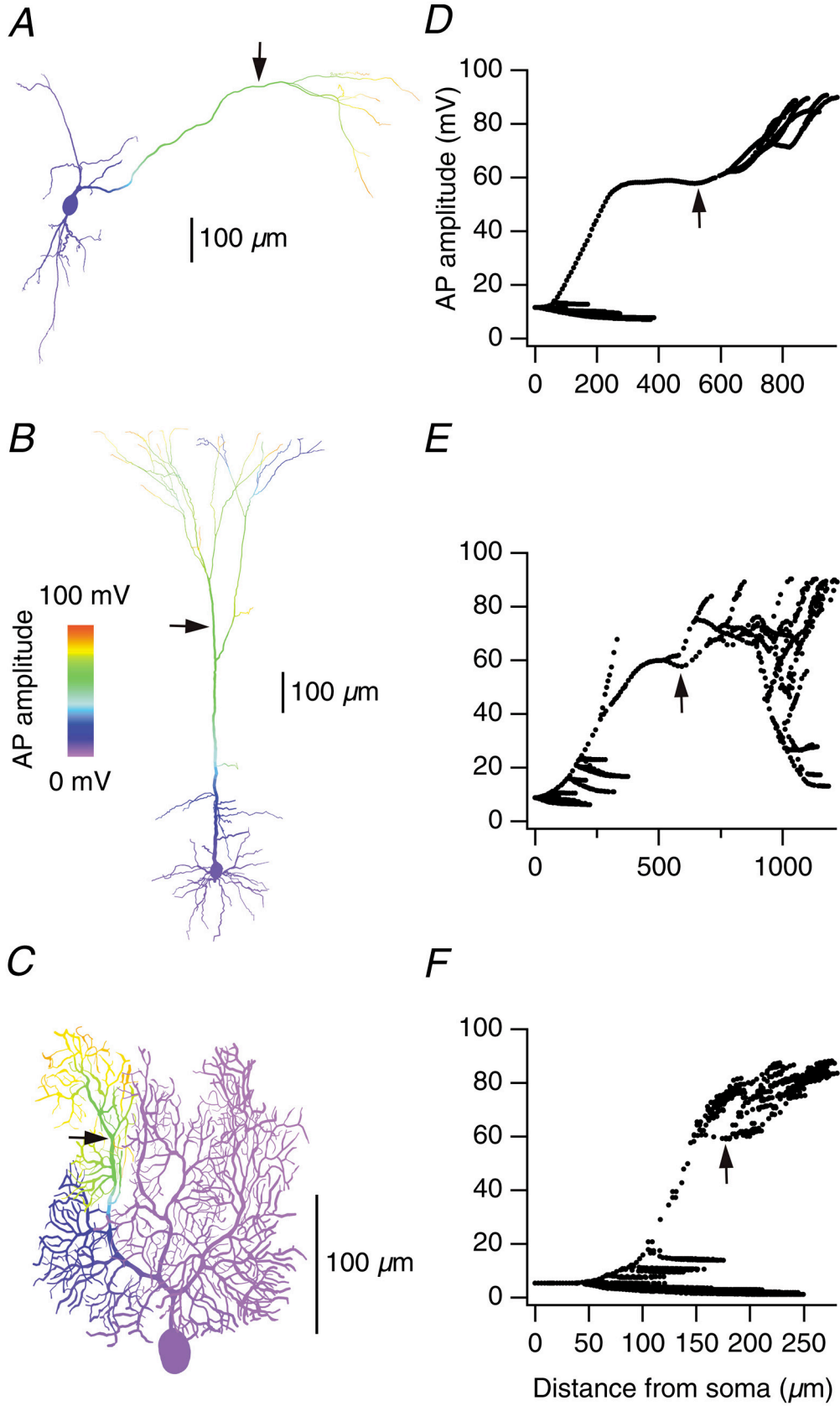
the AP as it approaches the branchpoint. However, if it is greater than one, i.e. if the combined input impedance of the daughter branches is lower than the input impedance of the parent branch, AP propagation may fail. For branches of uniform diameter and semi-infinite length, the impedance mismatch is given by Rall's geometric ratio ( $GR$ ),

$$GR = \sum_d r_d^{3/2} / r_p^{3/2}, \quad (3.2)$$

where  $r_d$  are the radii of the daughter branches and  $r_p$  is the radius of the parent branch. As the mean  $GR$  for all dendritic branchpoints in all 42 morphological reconstructions studied was  $2.4 \pm 0.08$ , this may explain the relatively strong correlation of  $g_{Na,thresh}$  with the number of branchpoints (Fig. 3.6A).

However, dendritic branches in realistic dendritic trees are finite in length, and the branchpoints are not the only sites contributing to the impedance mismatch along a dendrite. Usually, a succession of several branchpoints, connected by sections with taper or flare, lies within the spatial extent of a dendritic AP. Thus, it is difficult to predict the relative importance of various local maxima in the impedance mismatch in determining the fate of the AP except by explicit simulation of AP propagation (Figs. 3.3–3.5; Lüscher & Shiner, 1990; Manor et al., 1991). To obtain a better predictor of AP propagation, the analysis of impedance mismatches was simplified by constructing reduced models of the dendritic architecture (Segev, 1992), transforming each morphological reconstruction into a single unbranched equivalent cable (Fig. 3.7A; Fleshman et al., 1988; Clements & Redman, 1989; Ohme & Schierwagen, 1998). The impedance mismatch calculated in this cable approximates the mean impedance mismatch seen by an AP wavefront propagating in the original dendritic geometry. The shape of the impedance mismatch distribution (Fig. 3.7B) proved to be closely related to the efficacy of backpropagation. In particular, the cumulative impedance mismatch (Fig. 3.7B, inset) is a remarkably good predictor of both  $g_{Na,thresh}$  ( $r = 0.94$ ; Fig. 3.7C) and  $AP_{200}$  ( $r = -0.89$ ).

**Fig. 3.8** → Forward propagation of dendritically initiated APs. A-C, A dendritic AP was initiated in the neocortical pyramidal cell (B) using a synapse located at the arrowhead. The propagation of this AP in a nigral dopamine neuron (A) and a cerebellar Purkinje cell (C) was examined by applying it as a voltage clamp command at the location indicated by the arrowhead. The local amplitude of the propagating dendritic AP is coded by color. Propagation into the distal dendrites differs from that shown in Fig. 3.3 because the waveform of the dendritically initiated AP at its site of generation differs from the waveform of the backpropagating AP at the same site. (D-F) Scatter plots of dendritic AP amplitude vs. distance from the soma for the cells shown in A-C.

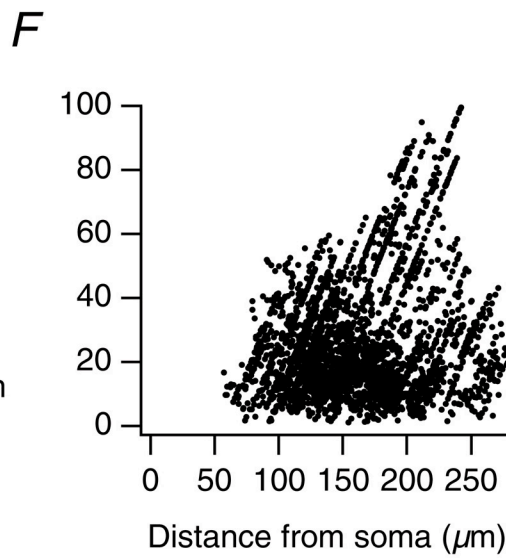
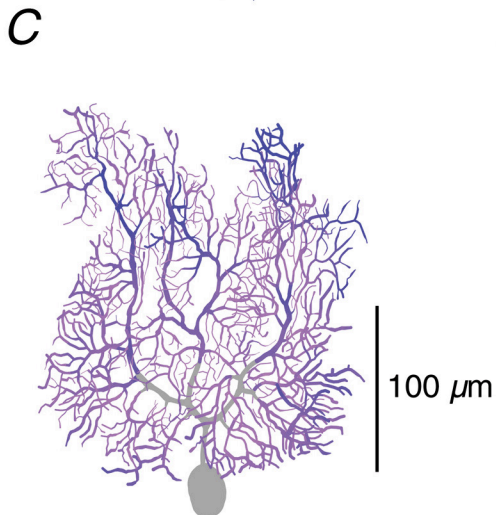
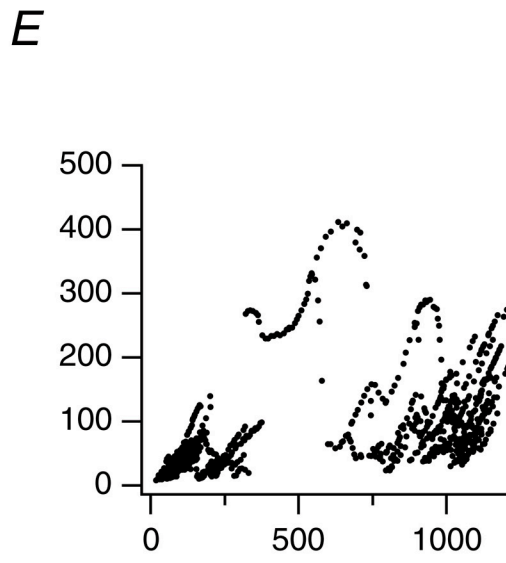
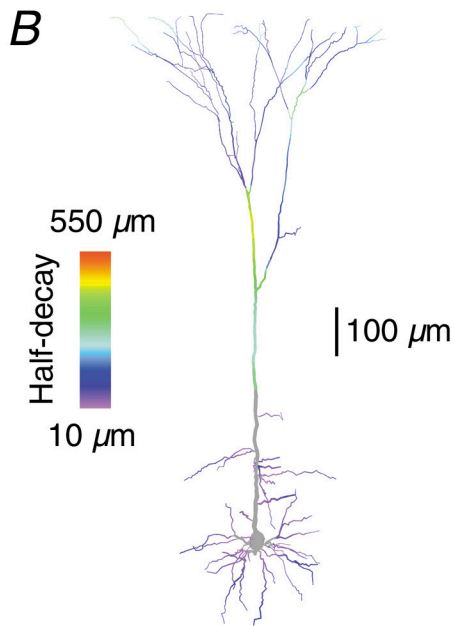
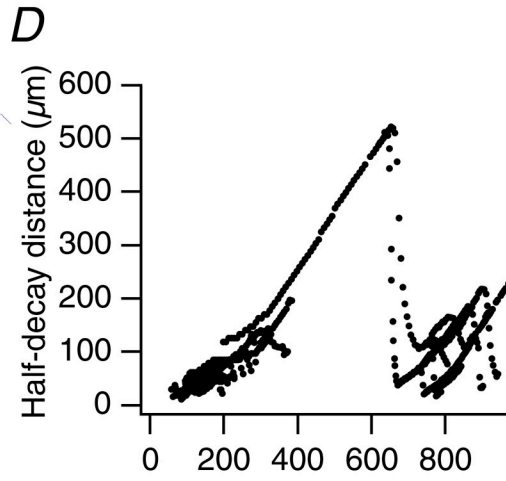
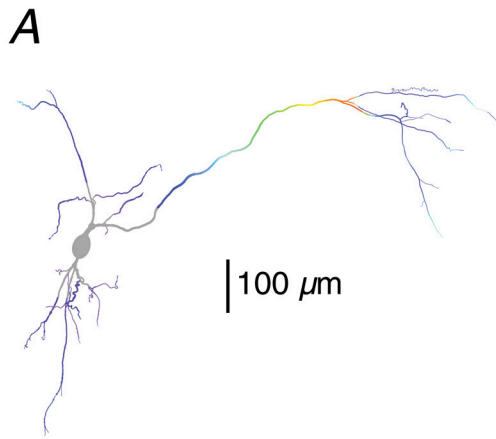


### 3.3.4 Forward propagation of dendritic APs depends on dendritic geometry

Under some circumstances it is possible to initiate Na<sup>+</sup> APs in dendrites. These dendritic APs propagate with variable efficacy to the soma in different cell types (Chen et al., 1997; Stuart et al., 1997a; Golding & Spruston, 1998; Kamondi et al., 1998; Schwindt & Crill, 1998; Martina et al., 2000; Larkum et al., 2001; Golding et al., 2002). The influence of dendritic geometry on the extent of forward propagation was investigated by comparing propagation of a dendritic AP in our set of neurons. The same dendritic AP waveform propagated to very different extents in different neurons with an identical distribution of voltage-gated channels (Fig. 3.8). In dopamine neurons and pyramidal neurons, propagation of the dendritic AP was very effective, while in Purkinje cells the dendritic AP was rapidly attenuated.

The spread of a dendritic AP is likely to depend on its site of origin in the dendritic tree, as previously shown for the spread of signals in passive dendrites (Rall, 1964; Zador et al., 1995; Roth & Häusser, 2001). The spread of the dendritic AP was therefore examined systematically from all locations in each dendritic tree, by simulating AP propagation starting successively from all compartments. To quantify the extent of forward propagation, the distance was measured at which the dendritic AP was reduced to half its original amplitude when travelling towards the soma. This "half-decay distance" depended strongly on the site of origin of the dendritic AP, and on the cell type (Fig. 3.9). The dendritic AP could propagate for hundreds of microns towards the soma from many dendritic locations in both dopamine and neocortical pyramidal neurons. In contrast, for nearly all locations in the cerebellar Purkinje cell, propagation was limited to  $< 50 \mu\text{m}$ , being restricted to the branchlets close to the initiation site. As shown in Table 3.2, the mean half-decay distance of the dendritic AP calculated over all sites of origin depended strongly on cell type. These findings indicate that both the local geometry, as well as the overall structure of the dendritic tree, are important determinants of forward propagation of dendritic APs.

**Fig. 3.9** → Forward propagation depends on dendritic geometry. *A-C*, Forward propagation of a dendritic AP was simulated successively at all dendritic locations in a nigral dopamine neuron (*A*), a layer 5 pyramidal cell (*B*), and a cerebellar Purkinje neuron (*C*). For each dendritic location, the distance at which the amplitude of the forward propagating dendritic AP was reduced to half of its amplitude was measured. This "half-decay distance" is coded by colour at the site of origin. For some input regions (i.e. those at or close to the soma), the AP never decays to half of its amplitude before reaching the soma. These regions are indicated in grey. The same data are plotted in *D-F* as a scatter plot, showing the half-decay distance of the dendritic AP initiated at a given location vs. distance of that location from the soma.



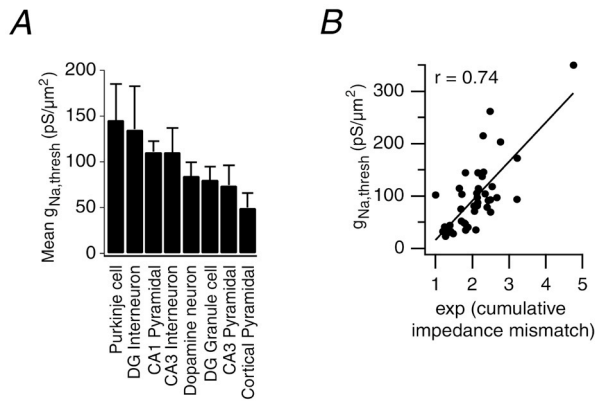


**Fig. 3.10.** Morphological determinants of forward propagation. *A*, Bar chart of the minimum somatodendritic  $Na^+$  channel density required for full AP propagation to the soma in different neuronal types. The origin of the dendritic AP was  $200 \mu m$  from the soma, on the longest dendritic path. Same dendritic geometries as in Fig. 3.5. *B*, Correlation between the cumulative impedance mismatch (scaled exponentially and measured as in Fig. 3.7B) in the equivalent cable constructed from the point of origin of the dendritic AP, and  $g_{Na,thresh}$  for forward propagation in the respective original dendritic geometry ( $n = 42$  morphological reconstructions).

**Table 3.2.** Extent of forward propagation of a dendritically initiated AP in different neurons

| Cell type <sup>a</sup>  | Mean half-decay distance ( $\mu m$ ) <sup>b</sup> | Maximal half-decay distance ( $\mu m$ ) <sup>c</sup> |
|-------------------------|---|--|
| Purkinje cell           | $29 \pm 3$  | $113 \pm 12$   |
| CA1 pyramidal cell      | $85 \pm 5$  | $323 \pm 58$   |
| CA3 pyramidal cell      | $138 \pm 12$                                      | $709 \pm 116$  |
| DG granule cell         | $128 \pm 10$                                      | $296 \pm 22$   |
| Cortical pyramidal cell | $80 \pm 6$  | $447 \pm 75$   |
| DG interneuron          | $99 \pm 10$                                       | $268 \pm 22$   |
| CA3 interneuron         | $130 \pm 12$                                      | $377 \pm 29$   |
| Dopamine neuron         | $143 \pm 16$                                      | $514 \pm 83$   |

<sup>a</sup> Same cells as in Table 3.1.

<sup>b</sup> Mean distance at which the dendritic AP is reduced to half its original amplitude during propagation to the soma for all sites of origin in the morphological reconstruction (conditions as in Fig. 3.9). Input regions from which the dendritic AP did not decay to half of its amplitude were excluded from the average.

<sup>c</sup> As in <sup>b</sup>, except the maximal distance measured is given.

To examine the relationship between dendritic  $Na^+$  channel density and forward propagation,  $g_{Na,thresh}$  (this time defined as the threshold  $g_{Na}$  for full propagation to the soma) was determined for forward propagating APs. As for



backpropagation,  $g_{\text{Na,thresh}}$  depended on cell type (Fig. 3.10A), with Purkinje cells again requiring the highest density of  $\text{Na}^+$  channels to ensure full propagation. The sequence of propagation efficacies was slightly different from that observed for backpropagation, consistent with the asymmetry of the dendritic architecture. To determine whether the underlying principles established for backpropagation also hold for propagation in the forward direction, equivalent cables were constructed from the point of view of the origin of the dendritic AP. Again, the cumulative impedance mismatch in the equivalent cable was an accurate predictor of propagation efficacy (Fig. 3.10B). Thus, as for backpropagation, a reduced model of dendritic geometry (Segev, 1992) is able to provide a functional link between the structure of a dendritic tree and the efficacy of forward propagation.

## 3.4 Discussion

Simulations in detailed compartmental models of a range of neurons show that dendritic geometry is an important factor determining both forward propagation and backpropagation of APs in dendrites. Recent work has highlighted the importance of dendritic voltage-gated channels in regulating the efficacy of AP propagation. The simulations described here complement this work and demonstrate that morphological features act in concert with dendritic voltage-gated channels to generate the observed diversity of AP propagation in dendritic trees of different neuronal types. Although there are clear differences in channel densities and properties between neurons (Llinas, 1988; Johnston et al., 1996), the simulations show that dendritic geometry determines how significant these differences are for neuronal function. These findings have important consequences for our understanding of how different neurons use dendritic APs as signalling mechanisms.

### 3.4.1 The link between dendritic geometry and propagation

Some dendritic geometries are remarkably resistant to AP propagation. Purkinje cells, for example, do not show effective propagation even with relatively high densities of voltage-gated Na<sup>+</sup> channels. This indicates that, as predicted by Rall (1964), the poor AP backpropagation observed experimentally in Purkinje cells is primarily due to their distinctive morphology, in conjunction with the relatively low channel densities (Stuart & Häusser, 1994) and narrow AP widths (Stuart et al., 1997b) found in these neurons. On the other hand, the simulations also identified dendritic geometries – such as those of dopamine neurons – which are very favourable for propagation, requiring only very low Na<sup>+</sup> channel densities for effective propagation into the distal dendrites. These findings suggest that the diversity in backpropagation efficacy observed experimentally (Stuart et al., 1997b) may be a consequence of the diversity in dendritic geometries in different neurons. Since forward propagation is also influenced by dendritic geometry in a similar manner, it is conceivable that the experimentally observed differences in forward propagation may also result in part from differences in dendritic structure. Although the present simulations have focused on APs mediated by Na<sup>+</sup> channels, it is likely that propagation of dendritic calcium spikes (Llinas & Sugimori, 1980; Amitai et al., 1993; Kim & Connors, 1993; Yuste et al., 1994; Schiller et al., 1997; Seamans et al., 1997; Schwindt & Crill, 1998; Helmchen et al., 1999; Larkum et al., 1999a,b; Larkum et al., 2001) is also regulated by dendritic geometry over a wide range.

Correlations of morphological features and the efficacy of AP propagation show that the number of dendritic branchpoints is a critical variable for determining propagation efficacy. An even more accurate predictor of propagation efficacy is the rate of increase in dendritic membrane area, which is determined by the number of branchpoints and the relationship between the diameter of parent and daughter dendrites at branchpoints. Based on this strong correlation, the present simulations make predictions about the relative efficacy of propagation for several cell types in which propagation has not been measured directly (e.g. granule cells and interneurons in the dentate gyrus). This measure should also permit similar predictions to be made for any dendritic geometry.

The link between the distribution of membrane area and propagation can be understood by noting that the functions describing the rate of increase in membrane area and the radius of the equivalent cable are closely related. For real dendrites this leads to distributions of similar shape (compare Figs. 3.6*B* and Fig. 3.7*A*). The profile of the equivalent cable, in turn, directly determines its impedance mismatch profile (Fig. 3.7*B*), which approximates the mean impedance mismatch at the same electrotonic location in the original morphological reconstruction (the impedance mismatch profile would be preserved exactly for branches of semi-infinite length: compare Eq. 3.2 and Eq. 3.1; Fleshman et al., 1988; Clements & Redman, 1989). Interestingly, the cumulative impedance mismatch in the equivalent cable provided the best predictor of backpropagation and forward propagation efficacy in 42 morphological reconstructions. This demonstrates that the equivalent cable transformation is a useful tool for predicting propagation of suprathreshold signals in active dendritic trees, which is remarkable given the fact that it involves numerous approximations (Fleshman et al., 1988; Clements & Redman, 1989). This result also suggests that the fate of a dendritic AP is usually not decided at a single branchpoint, but rather depends on the accumulation of unfavourable impedance mismatches over many branchpoints (Manor et al., 1991).

The finding that dendritic geometry has a significant impact on the propagation of APs in dendrites is in agreement with recent experimental evidence. Kim & Connors (1993) have shown that the efficacy of AP backpropagation in layer 5 pyramidal neurons is correlated with the number of apical oblique branches and the diameter of the apical trunk. In CA1 pyramidal neurons, a combination of calcium imaging and electrophysiological recordings has demonstrated that frequency-dependent attenuation of backpropagating APs is particularly effective in distal dendritic regions with extensive branching (Callaway & Ross, 1995; Spruston et al., 1995). Finally, backpropagation in thalamocortical relay neurons appears to be less effective in dendrites which exhibit branching (Williams & Stuart, 2000), again consistent with a key role for dendritic branching in determining propagation.

### 3.4.2 Modulation of AP propagation in dendrites

The densities of functional voltage-gated channels are subject to modulation by neurotransmitters, which can in turn affect backpropagation (Johnston et al., 1999). The simulations demonstrate that dendritic geometry places limits on the ability of backpropagation to be modulated in different neurons. As shown in Fig. 3.4, altering the density of dendritic Na<sup>+</sup> and K<sup>+</sup> channels over the same range can have strikingly diverse consequences on backpropagation in different dendritic geometries. Propagation of APs in different neurons, and in subregions of individual dendritic trees, will have different sensitivities to modulation of voltage-gated channels as a consequence of variations in dendritic geometry. In particular, neurons with an intermediate degree of dendritic branching, and dendritic regions exhibiting rapid increases in branching such as the apical tuft, should display the greatest sensitivity to modulation. This prediction is testable experimentally, as the functional density of different channel types can be varied pharmacologically to determine which dendritic geometries are most sensitive to modulation. The consequences of use-dependent activation and inactivation of voltage-gated channels should also depend on dendritic geometry. Consistent with this idea, frequency-dependent attenuation of APs in dendrites (Callaway & Ross, 1995; Spruston et al., 1995), which depends in part on a reduction in the effective Na<sup>+</sup> channel density (Colbert et al., 1997; Jung et al., 1997), is more pronounced in CA1 pyramidal neurons than in cortical pyramidal neurons (Stuart et al., 1997a), which exhibit less branching.

Dendritic geometry is not static, but can change dramatically both during development and in adulthood (Purves & Hadley, 1985; Bailey & Kandel, 1993). In particular, a substantial increase in dendritic branching has been shown to be associated with neuronal maturation (Altman, 1972; Berry & Bradley, 1976; Kasper et al., 1994; Wu et al., 1999), and with activation of messenger pathways known to be involved in synaptic plasticity (Nedivi et al., 1998; Wu & Cline, 1998; Yacoubian & Lo, 2000). The simulations suggest that this increase in dendritic complexity will reduce backpropagation unless compensated by increases in voltage-gated channel densities. Indeed there is substantial experimental evidence demonstrating that channel densities increase during development (MacDermott & Westbrook, 1986; Huguenard et al., 1988; O'Dowd et al., 1988; Zhu, 2000), in parallel with the changes in morphological complexity.

Finally, dendritic spine density could be involved in regulating AP propagation in dendrites (Baer & Rinzel, 1991; Jaslove, 1992). As spines can contribute over 50% of the dendritic membrane area, the relationship between membrane area and propagation efficacy (Fig. 3.6) indicates that the changes in spine density that can

occur during development (Gould et al., 1990; Harris et al., 1992) and synaptic plasticity (Engert & Bonhoeffer, 1999; Maletic-Savatic et al., 1999) will also modulate the extent of propagation. This effect should be particularly pronounced in neurons which also exhibit a high degree of dendritic branching. It is therefore interesting to note that neurons with minimal branching, such as dopamine neurons and interneurons, tend to be aspiny, while Purkinje cells, which exhibit a high degree of branching, have a very high spine density.

### 3.4.3 Implications for dendritic computation

Recent work has demonstrated that the backpropagating AP acts as a retrograde signal to dendritic synapses indicating that the axon has fired. This provides a coincidence detection mechanism which links postsynaptic APs and presynaptic activity to trigger synaptic plasticity (Markram et al., 1997; Stuart et al., 1997b; Linden, 1999). The present results show that since dendritic geometry limits the extent of propagation of dendritic APs, it defines the spatial range over which associations between synaptic inputs and APs can take place. In particular, the simulations demonstrate that highly branching dendritic geometries do not permit strong coupling between axonal output and distal synapses, and thus in these neurons the backpropagating AP cannot act as a global associative signal (Stuart et al., 1997b; Linden, 1999; Sjöström & Nelson, 2002). Since such geometries are also poor substrates for forward propagation of APs (Figs. 3.8–3.10), synaptic integration in these neurons is far more dependent on local associations between inputs. Indeed, such dendritic trees may be adapted to keep associations between inputs more localized in order to increase the number of independent sites of integration (Mel, 1993; Poirazi & Mel, 2001). On the other hand, dendritic geometries that favour propagation and are sensitive to modulation of propagation allow the associativity between output and input to be tuned over a wide range.

Dendritic geometry will also influence the interaction between backpropagating APs and dendritically initiated APs. The initiation of dendritic APs requires strong and temporally synchronous synaptic input (Schiller et al., 1997; Stuart et al., 1997a; Golding & Spruston, 1998), properties consistent with their role as coincidence detectors. However, in cortical pyramidal neurons pairing backpropagating APs with distal synaptic input can substantially lower the threshold for initiation of dendritic APs, which can in turn lead to burst firing in the axon (Helmchen et al., 1999; Larkum et al., 1999a,b; Larkum et al., 2001; Schaefer et al., 2003b). By limiting the spatial spread of backpropagating and forward propagating APs, dendritic geometry should therefore play an important role in determining the sensitivity of individual neurons to

coincident synaptic input, as well as in defining the relationship between dendritic APs and neuronal output via the axon. Taken together, these considerations indicate that the large diversity in dendritic geometry may have direct consequences for the computational strategies used by different neurons.

## 4 Comprehensive discussion

A new scientific method should not ultimately be a goal in and of itself. Its significance will depend on what has been (and will be) found out by applying it to open problems, how difficult or easy it is to use, and how reliable and accurate the results are. Therefore I would like to conclude this thesis with a perspective on present and future applications of the new experimental and simulation methods described in the preceding chapters.

### 4.1 Applications of the voltage jump method

The voltage jump method addresses a long-standing problem in cellular neuroscience. In most types of neurons it is not possible to voltage-clamp a dendritic synapse using an electrode at the soma (see section 2.3.1). Before the development of the voltage jump method, experimentalists had a choice among three options: First, they could ignore the problem. Arguably, this was the most popular choice and resulted in many erroneous results being published before papers by Spruston et al. (1993) and Major (1993) illustrated the problem in graphic detail, making it more difficult to publish such studies in respectable journals. Second, they could choose not to do the experiment they originally intended to do. It is often difficult to decide whether the second option is worse than the first. Finally, they could laboriously build a compartmental model of the cell recorded from and "work backwards" from the measured somatic clamp current waveform to the actual conductance waveform at the synapse (e.g. Jonas et al., 1993). This has rarely been done because of the amount of work involved.

It is clear from the third option that this is an attempt to solve a typical "inverse problem". That is, given the parameters of the synaptic conductance waveform (i.e. its amplitude and kinetics), the location of the synapse and the cable properties of the neuron, it is straightforward to compute the clamp current measured via the somatic recording pipette (see section 1.2). But it is very difficult, given the clamp current at the soma, to come up with a unique solution for the synaptic conductance waveform that gave rise to it, since knowledge of the location of the synapse(s) and in particular the cable properties of the neuron is often rather incomplete.

The voltage jump method was therefore developed to bypass this inverse problem. It is a combination of a specific experimental protocol and a new technique of data analysis. Unlike the method developed by Schaefer et al. (2003a) to recover the densities and kinetics of voltage gated conductances in non-space clamped structures, it is essentially model-free. No errors associated with a model influence its

results, and no model assumptions are made, except that the cell is passive in the voltage range in which it is tested, an assumption that can be verified experimentally (Fig. 2.15A–D).

A key ingredient of the voltage jump method is the use of causality: additional synaptic current elicited by an increase in the synaptic driving force can only flow after the increase in driving force happens. Thus, by varying the relative timing of the synaptic stimulation and the increase in synaptic driving force, a sliding window is moved step by step across the synaptic conductance, whose time course is then *reconstructed* by analyzing the synaptic charge as a function of this relative timing. In principle this works for every synapse in every neuron. A typical problem in the practical application of the voltage jump method, especially if the synapses are small and unreliable, is the low signal-to-noise ratio and thus the need to sample many sweeps (Fig. 2.15E). To collect the hundreds of sweeps that are sometimes necessary, sufficiently stable recordings are required. But this is achievable in practice in many cell types, as shown by the examples summarized in sections 2.4.3 – 2.4.6.

The sources of error in the voltage jump method and in compartmental models of neurons are thus complementary: the accuracy of the voltage jump method is limited by statistical errors, not systematic errors. Estimates of the time constant of decay of the synaptic conductance obtained via the voltage jump method are largely unbiased, and their accuracy can be increased simply by averaging more sweeps. In contrast, compartmental models suffer mostly from systematic errors, not statistical errors (Roth & Häusser, 2001). It is therefore tempting to combine the voltage jump method and the construction of a compartmental model of the cell recorded from to offset the two kinds of errors. Indeed, as shown by the example described in section 2.4.4 the voltage jump method can be used to calibrate a compartmental model of the same cell. In the future more studies are expected to combine the voltage jump method and compartmental models to validate estimates of the amplitude and time course of synaptic conductances in dendrites.

The most interesting future applications of the voltage jump method that can be suggested today can probably be found in the mapping of (subthreshold) receptive fields *in vivo*. The goal here is to take the mapping one step further from the soma (e.g. Brecht et al., 2003) to the synapses. Where on the dendritic tree of the cell recorded from are the synapses located which are activated in response to a sensory stimulus? What is the compound kinetics and the amplitude of the compound synaptic conductance? Little is known about the answers, and experiments of this type are feasible today, largely due to the advent of *in vivo* whole-cell recordings. They could be combined with two-photon uncaging of glutamate to mimic synaptic conductances in defined locations on the dendritic tree, to map both



the distribution of synaptic conductances as a function of distance from the soma as well as the electrotonic structure of the neuron recorded from.

## 4.2 Validation of compartmental models

To construct a passive compartmental model based on measurements of impulse responses at multiple locations in a neuron, as well as a morphological reconstruction of the same cell, also satisfies the characteristics of an inverse problem. But if the model itself is the goal, there is no free lunch and the only option available is to solve this inverse problem (Roth & Häusser, 2001). Only such a detailed and accurate compartmental model allows quantitative predictions (see section 4.3), and later, abstractions (see section 4.4) of the rules by which a neuron transforms synaptic input into spike output.

Construction of the compartmental models was accompanied by an extensive error analysis, which yielded quantitative estimates of the influence of various sources of error on the best-fit parameters and the predictions of the models (Roth & Häusser, 2001). One of the most surprising new results of the error analysis was the relatively small effect of statistical errors, i.e. the trial-to-trial variability of the impulse responses, which caused relative errors in the best-fit parameters of only a few percent. In contrast, systematic errors, mostly due to uncertainty in the reconstructed dendritic diameters, were responsible for large (up to 50%) relative errors in the "raw" model parameters such as  $C_m$  and  $R_m$ . However, the error analysis also showed that predictions of the models, such as the attenuation of EPSCs or EPSPs from their dendritic origin to the soma, may be more robust than suggested by the uncertainties in individual electrical and morphological parameters, which trade off against each other.

Future improvements of passive compartmental models are likely to depend on voltage-sensitive dye imaging using new, more sensitive dyes, allowing measurements of the membrane potential simultaneously at many points in the neuron. This should allow the unique identification of possible spatial inhomogeneities in the passive (and active) membrane parameters due to an even larger number of constraints for the compartmental models. Another important improvement will be provided by the automated reconstruction of neuronal morphology using novel image processing algorithms. Objective measurements of dendritic diameters will be particularly useful since they are expected to reduce the effect of a major source of error.

### 4.3 Functional compartments in dendritic trees

To understand how neurons transform synaptic inputs into action potential output we need to find out, firstly, what the functional compartments in dendritic trees are, and secondly, how they interact (see chapter 1). The focus of this thesis is on electrical, not chemical compartments. It is also necessary to distinguish between the spread of subthreshold synaptic potentials and the propagation of suprathreshold regenerative events. Conditions for the initiation of these events, and the subsequent propagation of spikes in the dendritic tree, but also the spread of subthreshold synaptic potentials depend both on the density and kinetics of voltage-gated conductances, as well as the dendritic branching pattern.

Only in models such as those employed in this thesis the influence of the dendritic branching pattern can be separated from the influence of the voltage-gated conductances, and only models allow for a clean separation of the initiation of regenerative events from their propagation in the dendritic tree once they have been initiated.

Simulations of the spread of subthreshold EPSPs show that Purkinje cells are "democratic", i.e. synapses of equal conductance evoke very similar somatic EPSP amplitudes regardless of their location on the dendritic tree. In the subthreshold regime, the dendritic tree of Purkinje cells could therefore be represented by a single compartment. In contrast, synapses on the apical tuft of neocortical pyramidal cells evoke much smaller somatic EPSPs than synapses near the soma. The simulations show that this difference is predictable already from the differences in the dendritic branching pattern of these cell types. It is mostly due to the absence of a long primary dendrite in Purkinje cells.

Simulations of the forward and backpropagation of action potentials in dendrites show that the structure of the Purkinje cell dendritic tree limits action potential propagation in both directions. Conditions for backpropagation are particularly poor, and even an upregulation of dendritic Na<sup>+</sup> channels to the highest levels found in the dendrites of other cell types would not overcome the very large impedance mismatch within the primary dendrite. In contrast, action potentials in neocortical pyramidal cells propagate in both directions over distances of several hundreds of micrometers, and propagation is easily regulated by modulation of the density of dendritic voltage-gated conductances and by changes in the branching pattern of the apical tree (Schaefer et al., 2003b). Thus, action potentials propagating in the dendrites of pyramidal cells provide a variable coupling of the somatic and dendritic spike initiation zones in these cells, which directly influences their input-output relation (Larkum et al., 1999a,b; Larkum et al., 2001; Schaefer et al., 2003b).

The pronounced differences between the subthreshold and suprathreshold simulation results in Purkinje cells (compare Roth & Häusser (2001) and chapter 3) may seem paradox at first glance, but they illustrate that the size, number and degree of interaction between functional compartments are strongly frequency-dependent. For high frequencies ( $> 100$  Hz) the impedance mismatch at a given point in a dendritic tree is dominated by the local membrane capacitance (proportional to the membrane area) "seen" from this point. The arrangement of functional compartments in the dendritic tree will therefore depend on the type of signals described, as well as on the background synaptic activity *in vivo*, which could transform the rules for synaptic integration on a millisecond time scale.

## 4.4 Simple versus complex models

Everything should be made as simple as possible, but not simpler. – Albert Einstein

Most of this thesis is concerned with an exploration of complex models of single neurons. To understand experiments on real neurons, and to represent their results it is necessary to work with these complicated models. However, to understand the principles of neural computation it is necessary to come up with reduced models (Segev, 1992) that capture as much as possible of the essential behaviour of the complex models. In this thesis, reduced models are used mostly as tools to understand structure-function relations in the complex models (equivalent cylinder in chapter 2, equivalent cable in chapter 3). Reduced models can also serve as a compact representation of our current knowledge of neurons, and to state hypotheses about their function, such as their input-output relations. Exactly which details of the complex models need to be preserved in the reduced models obviously depends on the question addressed. Equivalent cables that were built starting at the soma were well suited to represent action potential backpropagation in the original models, for example. Forward propagation of spikes initiated in the dendrites, however, was represented well only in equivalent cables that were constructed from the point of view of the spike initiation site in the dendrites. This suggests that perhaps the complexity is irreducible, and we need full morphological reconstructions and detailed models of voltage-dependent conductances in the dendrites in order to represent all relevant aspects of neuronal function. In any case it will be necessary to identify those mechanisms – found in experiments on brain slices or in models – that are really relevant for the behaviour of the animal. This will require the development of new experimental techniques, such as two-photon microscopy in awake, behaving animals (Helmchen et al., 2001) to test whether e.g. local spikes initiated in the dendrites are a common occurrence during certain behavioural tasks. The results of

experiments of this kind will serve as a guide to construct reduced models of neurons that describe the relevant principles of their operation. Ultimately, these reduced models will be used in network models to show how dendritic mechanisms contribute to information processing in the brain.

## 4.5 Acknowledgements

Special thanks to my advisor, Bert Sakmann, for giving me the unique opportunity to work with him for twelve years, first part-time during my studies of physics, then during my diploma and doctoral theses. It was an exciting time during which new windows to the function of the brain were opened, and new kinds of experimental data became available for the first time. Sometimes it was difficult to decide which data to work on first. I am grateful to Bert Sakmann for his insistence to proceed step by step, to keep things simple, for his guidance, enthusiasm and generosity, and for exposing me to his way of doing science.

Special thanks also go to Peter Jonas, who introduced me to cellular neuroscience, supervised my first research project and insisted that things should be done properly; to Michael Häusser for his friendship and close collaboration over many years; to Winfried Denk for late-night discussions and guidance; to Idan Segev for theoretical insights and inspiration, and to Greg Stuart, Nelson Spruston, Jackie & Izik Schiller and Henry Markram for an exciting time, lots of upshots and for teaching me to be unafraid of asking "stupid" questions.

I am grateful to Philippe Ascher, Boris Barbour, Tom Bartol, Gerard Borst, Michael Brecht, Beverley Clark, Erik De Schutter, Jeff Diamond, Jörg Geiger, Fritjof Helmchen, Michael Hines, Julian Jack, Katharina Kaiser, Georg Köhr, Alon Korngreen, Matthew Larkum, Mickey London, Zach Mainen, Guy Major, Troy Margrie, Zoltan Nusser, Carl Petersen, Alex Reyes, Paul Rhodes, Angus Silver, Joel Stiles, Nathan Urban, Sam Wang and Jack Waters, whose data, software, ideas, comments, discussion, and other help were essential for the present work,

to Philip Broser, Veronica Egger, Dirk Feldmeyer, Joe Lübke, Ora Ohana, Kurt Sätzler and Gabriel Wittum for ongoing collaboration,

to Moritz Helmstaedter and Andreas Schaefer for giving a much-needed boost to the theory department at Abteilung Zellphysiologie,

to Klaus Bauer and Klaus Rohm for managing and maintaining excellent computing facilities,

to Marlies Kaiser and Ramon Granadillo for being there when I needed their help, and to my parents for everything.



## 5 References

### 5.1 References cited

Abeles, M. (1982). Role of the cortical neuron: integrator or coincidence detector? *Israeli Journal of Medical Sciences* **18**, 83-92.

Altman, J. (1972). Postnatal development of the cerebellar cortex in the rat. II. Phases in the maturation of Purkinje cells and of the molecular layer. *Journal of Comparative Neurology* **145**, 399-463.

Amitai, Y., Friedman, A., Connors, B.W. & Gutnick, M.J. (1993). Regenerative activity in apical dendrites of pyramidal cells in neocortex. *Cerebral Cortex* **3**, 26-38.

Baer, S.M. & Rinzel, J. (1991). Propagation of dendritic spikes mediated by excitable spines: a continuum theory. *Journal of Neurophysiology* **65**, 874-890.

Bailey, C.H. & Kandel, E.R. (1993). Structural changes accompanying memory storage. *Annual Review of Physiology* **55**, 397-426.

Barbour, B., Keller, B.U., Llano, I. & Marty, A. (1994). Prolonged presence of glutamate during excitatory synaptic transmission to cerebellar Purkinje cells. *Neuron* **12**, 1331-1343.

Berry, M. & Bradley, P. (1976). The growth of the dendritic trees of Purkinje cells in the cerebellum of the rat. *Brain Research* **112**, 1-35.

Bischofberger, J. & Jonas, P. (1997). Action potential propagation into the presynaptic dendrites of rat mitral cells. *Journal of Physiology* **504**, 359-365.

Bischofberger, J. & Jonas, P. (2002). TwoB or not twoB: differential transmission at glutamatergic mossy fiber-interneuron synapses in the hippocampus. *Trends in Neurosciences* **25**, 600-603.

Borst, J.G.G., Helmchen, F. & Sakmann, B. (1995). Pre- and postsynaptic whole-cell recordings in the medial nucleus of the trapezoid body of the rat. *Journal of Physiology* **489**, 825-840.

Borst, J.G.G., Lodder, J.C. & Kits, K.S. (1994). Large amplitude variability of GABAergic IPSCs in melanotropes from *Xenopus laevis* – evidence that quantal size differs between synapses. *Journal of Neurophysiology* **71**, 639-655.

Brecht, M., Roth, A. & Sakmann, B. (2003). Dynamic receptive fields of reconstructed pyramidal cells in layers 3 and 2 of rat somatosensory barrel cortex. *Journal of Physiology* **553**, 243-265.

Buzsáki, G. & Kandel, A. (1998). Somadendritic backpropagation of action potentials in cortical pyramidal cells of the awake rat. *Journal of Neurophysiology* **79**, 1587-1591.

Callaway, J.C. & Ross, W.N. (1995). Frequency-dependent propagation of sodium action potentials in dendrites of hippocampal CA1 pyramidal neurons. *Journal of Neurophysiology* **74**, 1395-1403.

Carnevale, N.T. & Johnston, D. (1982). Electrophysiological characterization of remote chemical synapses. *Journal of Neurophysiology* **47**, 606-621.

Chen, W.R., Midtgaard, J. & Shepherd, G.M. (1997). Forward and backward propagation of dendritic impulses and their synaptic control in mitral cells. *Science* **278**, 463-467.

Christie, J.M. & Westbrook, G.L. (2003). Regulation of backpropagating action potentials in mitral cell lateral dendrites by A-type potassium currents. *Journal of Neurophysiology* **89**, 2466-2472.

Clements, J.D. & Redman, S.J. (1989). Cable properties of cat spinal motoneurons measured by combining voltage clamp, current clamp and intracellular staining. *Journal of Physiology* **409**, 63-87.

Colbert, C.M., Magee, J.C., Hoffman, D.A. & Johnston, D. (1997). Slow recovery from inactivation of Na<sup>+</sup> channels underlies the activity-dependent attenuation of dendritic action potentials in hippocampal CA1 pyramidal neurons. *Journal of Neuroscience* **17**, 6512-6521.

De Schutter, E. & Bower, J.M. (1994). Simulated responses of cerebellar Purkinje cells are independent of the dendritic location of granule cell synaptic inputs. *Proceedings of the National Academy of Sciences of the USA* **91**, 4736-4740.



DiGregorio, D.A., Nusser, Z. & Silver, R.A. (2002). Spillover of glutamate onto synaptic AMPA receptors enhances fast transmission at a cerebellar synapse. *Neuron* **35**, 521-533.

Dzubay, J.A. & Jahr, C.E. (1999). The concentration of synaptically released glutamate outside of the climbing fiber-Purkinje cell synaptic cleft. *Journal of Neuroscience* **19**, 5265-5274.

Engert, F. & Bonhoeffer, T. (1999). Dendritic spine changes associated with hippocampal long-term synaptic plasticity. *Nature* **399**, 66-70.

Finkel, A.S. & Redman, S.J. (1983). The synaptic current evoked in cat spinal motoneurons by impulses in single group Ia axons. *Journal of Physiology* **342**, 615-632.

Fleshman, J.W., Segev, I. & Burke, R.B. (1988). Electrotonic architecture of type-identified alpha-motoneurons in the cat spinal cord. *Journal of Neurophysiology* **60**, 60-85.

Forsythe, I.D. & Barnes-Davies, M. (1993). The binaural auditory pathway – excitatory amino-acid receptors mediate dual timecourse excitatory postsynaptic currents in the rat medial nucleus of the trapezoid body. *Proceedings of the Royal Society B* **251**, 151-157.

Gentet, L.J., Stuart, G.J. & Clements, J.D. (2000). Direct measurement of specific membrane capacitance in neurons. *Biophysical Journal* **79**, 314-320.

Golding, N.L. & Spruston, N. (1998). Dendritic sodium spikes are variable triggers of axonal action potentials in hippocampal CA1 pyramidal neurons. *Neuron* **21**, 1189-1200.

Golding, N.L., Staff, N.P. & Spruston, N. (2002). Dendritic spikes as a mechanism for cooperative long-term potentiation. *Nature* **418**, 326-331.

Goldstein, S.S. & Rall, W. (1974). Changes of action potential shape and velocity for changing core conductor geometry. *Biophysical Journal* **14**, 731-757.

Gould, E., Woolley, C.S., Frankfurt, M. & McEwen, B.S. (1990). Gonadal steroids regulate dendritic spine density in hippocampal pyramidal cells in adulthood. *Journal of Neuroscience* **10**, 1286-1291.

Grosche, J., Kettenmann, H. & Reichenbach, A. (2002). Bergmann glial cells form distinct morphological structures to interact with cerebellar neurons. *Journal of Neuroscience Research* **68**, 138-149.

Häusser, M. (1994). Kinetics of excitatory synaptic currents in Purkinje cells studied using dendritic patch-clamp recording. *Society for Neuroscience Abstracts* **20**, 891.

Häusser, M. & Roth, A. (1997). Estimating the time course of the excitatory synaptic conductance in neocortical pyramidal cells using a novel voltage jump method. *Journal of Neuroscience* **17**, 7606-7625.

Häusser, M., Spruston, N. & Stuart, G.J. (2000). Diversity and dynamics of dendritic signaling. *Science* **290**, 739-744.

Häusser, M., Stuart, G., Racca, C. & Sakmann, B. (1995). Axonal initiation and active dendritic propagation of action potentials in substantia nigra neurons. *Neuron* **15**, 637-647.

Harris, K.M., Jensen, F.E. & Tsao, B. (1992). Three-dimensional structure of dendritic spines and synapses in rat hippocampus (CA1) at postnatal day 15 and adult ages: implications for the maturation of synaptic physiology and long-term potentiation. *Journal of Neuroscience* **12**, 2685-2705.

Helmchen, F., Fee, M.S., Tank, D.W. & Denk, W. (2001). A miniature head-mounted two-photon microscope: High-resolution brain imaging in freely moving animals. *Neuron* **31**, 903-912.

Helmchen, F., Svoboda, K., Denk, W. & Tank, D.W. (1999). *In vivo* dendritic calcium dynamics in deep-layer cortical pyramidal neurons. *Nature Neuroscience* **2**, 989-996.

Hestrin, S. (1993). Different glutamate receptor channels mediate fast excitatory synaptic currents in inhibitory and excitatory cortical neurons. *Neuron* **11**, 1083-1091.

Hestrin, S., Nicoll, R.A., Perkel, D.J. & Sah, P. (1990). Analysis of excitatory synaptic action in pyramidal cells using whole-cell recording from rat hippocampal slices. *Journal of Physiology* **422**, 203-225.

Hines, M.L. & Carnevale, N.T. (1997). The NEURON simulation environment. *Neural Computation* **9**, 1179-1209.

Hines, M.L. & Carnevale, N.T. (2000). Expanding NEURON's repertoire of mechanisms with NMODL. *Neural Computation* **12**, 839-851.

Hodgkin, A.L. & Huxley, A.F. (1952). A quantitative description of membrane current and its application to conductance and excitation in nerve. *Journal of Physiology* **117**, 500-544.

Hoffman, D.A., Magee, J.C., Colbert, C.M. & Johnston, D. (1997). K<sup>+</sup> channel regulation of signal propagation in dendrites of hippocampal pyramidal neurons. *Nature* **387**, 869-875.

Holmes, W.R. (1989). The role of dendritic diameters in maximizing the effectiveness of synaptic inputs. *Brain Research* **478**, 127-137.

Huguenard, J.R., Hamill, O.P. & Prince, D.A. (1988). Developmental changes in Na<sup>+</sup> conductances in rat neocortical neurons: appearance of a slowly inactivating component. *Journal of Neurophysiology* **59**, 778-795.

Isaacson, J.S. & Walmsley, B. (1995). Receptors underlying excitatory synaptic transmission in slices of the rat anteroventral cochlear nucleus. *Journal of Neurophysiology* **73**, 964-973.

Jack, J.J.B., Noble, D. & Tsien, R.W. (1983). *Electric Current Flow in Excitable Cells*. Clarendon Press, Oxford.

Jack, J.J.B., Redman, S.J. & Wong, K. (1981). The components of synaptic potentials evoked in spinal motoneurons by impulses in single group Ia afferents. *Journal of Physiology* **321**, 65-96.

Jaslove, S.W. (1992). The integrative properties of spiny distal dendrites. *Neuroscience* **47**, 495-519.

Johnston, D. & Brown, T.H. (1983). Interpretation of voltage-clamp measurements in hippocampal neurons. *Journal of Neurophysiology* **50**, 464-486.

Johnston, D., Hoffman, D.A., Colbert, C.M. & Magee, J.C. (1999). Regulation of back-propagating action potentials in hippocampal neurons. *Current Opinion in Neurobiology* **9**, 288-292.

Johnston, D., Magee, J.C., Colbert, C.M. & Christie, B.R. (1996). Active properties of neuronal dendrites. *Annual Review of Neuroscience* **19**, 165-186.

Jonas, P., Major, G. & Sakmann, B. (1993). Quantal components of unitary EPSCs at the mossy fibre synapse on CA3 pyramidal cells of rat hippocampus. *Journal of Physiology* **472**, 615-663.

Jonas, P., Racca, C., Sakmann, B., Seeburg, P.H. & Monyer, H. (1994). Differences in Ca<sup>2+</sup> permeability of AMPA-type glutamate receptor channels in neocortical neurons caused by differential GluR-B subunit expression. *Neuron* **12**, 1281-1289.

Joyner, R.W., Moore, J.W. & Ramon, F. (1975). Axon voltage-clamp simulations. III. Postsynaptic region. *Biophysical Journal* **15**, 37-54.

Joyner, R.W., Westerfield, M. & Moore, J.W. (1980). Effects of cellular geometry on current flow during a propagated action potential. *Biophysical Journal* **31**, 183-194.

Jung, H.-Y., Mickus, T. & Spruston, N. (1997). Prolonged sodium channel inactivation contributes to dendritic action potential attenuation in hippocampal pyramidal neurons. *Journal of Neuroscience* **17**, 6639-6646.

Kamondi, A., Acsády, L. & Buzsáki, G. (1998). Dendritic spikes are enhanced by cooperative network activity in the intact hippocampus. *Journal of Neuroscience* **18**, 3919-3928.

Kasper, E.M., Lübke, J., Larkman, A.U. & Blakemore, C. (1994). Pyramidal neurons in layer 5 of the rat visual cortex. III. Differential maturation of axon targeting, dendritic morphology, and electrophysiological properties. *Journal of Comparative Neurology* **339**, 495-518.

Kim, H.G. & Connors, B.W. (1993). Apical dendrites of the neocortex: correlation between sodium- and calcium-dependent spiking and pyramidal cell morphology. *Journal of Neuroscience* **13**, 5301-5311.

Kirson, E.D. & Yaari, Y. (1996). Synaptic NMDA receptors in developing mouse hippocampal neurones: functional properties and sensitivity to ifenprodil. *Journal of Physiology* **497**, 437-455.

Kleppe, I.C. & Robinson, H.P.C. (1999). Determining the activation time course of synaptic AMPA receptors from openings of colocalized NMDA receptors. *Biophysical Journal* **77**, 1418-1427.

König, P., Engel, A.K. & Singer, W. (1996). Integrator or coincidence detector? The role of the cortical neuron revisited. *Trends in Neurosciences* **19**, 130-137.

Koh, D.-S., Jonas, P. & Vogel, W. (1994). Na<sup>+</sup>-activated K<sup>+</sup> channels localized in the nodal region of myelinated axons of *Xenopus*. *Journal of Physiology* **479**, 183-197.

Lapicque, L. (1907). Recherches quantitatives sur l'excitation électrique des nerfs traitée comme une polarisation. *Journal de Physiologie et de Pathologie générale* **9**, 620-635.

Larkum, M.E., Kaiser, K.M.M. & Sakmann, B. (1999a). Calcium electrogenesis in distal apical dendrites of layer 5 pyramidal cells at a critical frequency of back-propagating action potentials. *Proceedings of the National Academy of Sciences of the USA* **96**, 14600-14604.

Larkum, M.E., Zhu, J.J. & Sakmann, B. (1999b). A new cellular mechanism for coupling inputs arriving at different cortical layers. *Nature* **398**, 338-341.

Larkum, M.E., Zhu, J.J. & Sakmann, B. (2001). Dendritic mechanisms underlying the coupling of the dendritic with the axonal action potential initiation zone of adult rat layer 5 pyramidal neurons. *Journal of Physiology* **533**, 447-466.

Linden, D.J. (1999). The return of the spike: postsynaptic action potentials and the induction of LTP and LTD. *Neuron* **22**, 661-666.

Llano, I., Marty, A., Armstrong, C.M. & Konnerth, A. (1991). Synaptic and agonist-induced currents of Purkinje cells in rat cerebellar slices. *Journal of Physiology* **434**, 183-213.

Llinás, R.R. (1988). The intrinsic electrophysiological properties of mammalian neurons: insights into central nervous system function. *Science* **242**, 1654-1664.

Llinás, R. & Sugimori, M. (1980). Electrophysiological properties of *in vitro* Purkinje cell dendrites in mammalian cerebellar slices. *Journal of Physiology* **305**, 197-213.

Lübke, J., Roth, A., Feldmeyer, D. & Sakmann, B. (2003). Morphometric analysis of the columnar innervation domain of neurons connecting layer 4 and layer 2/3 of juvenile rat barrel cortex. *Cerebral Cortex* **13**, 1051-1063.

Lüscher, H.R. & Shiner, J.S. (1990). Computation of action potential propagation and presynaptic bouton activation in terminal arborizations of different geometries. *Biophysical Journal* **58**, 1377-1388.

MacDermott, A.B. & Westbrook, G.L. (1986). Early development of voltage-dependent sodium currents in cultured mouse spinal cord neurons. *Developmental Biology* **113**, 317-326.

Magee, J., Hoffman, D., Colbert, C. & Johnston, D. (1998). Electrical and calcium signaling in dendrites of hippocampal pyramidal neurons. *Annual Review of Physiology* **60**, 327-346.

Mainen, Z.F., Joerges, J., Huguenard, J.R. & Sejnowski, T.J. (1995). A model of spike initiation in neocortical pyramidal neurons. *Neuron* **15**, 1427-1439.

Mainen, Z.F. & Sejnowski, T.J. (1996). Influence of dendritic structure on firing pattern in model neocortical neurons. *Nature* **382**, 363-366.

Major, G. (1993). Solutions for transients in arbitrarily branching cables: III. Voltage clamp problems. *Biophysical Journal* **65**, 469-491.

Major, G., Evans, J.D. & Jack, J.J.B. (1993). Solutions for transients in arbitrarily branching cables: II. Voltage clamp theory. *Biophysical Journal* **65**, 450-468.

- Major, G., Larkman, A.U., Jonas, P., Sakmann, B. & Jack, J.J.B. (1994). Detailed passive cable models of whole-cell recorded CA3 pyramidal neurons in rat hippocampal slices. *Journal of Neuroscience* **14**, 4613-4638.
- Maletic-Savatic, M., Malinow, R. & Svoboda, K. (1999). Rapid dendritic morphogenesis in CA1 hippocampal dendrites induced by synaptic activity. *Science* **283**, 1923-1927.
- Manor, Y., Koch, C. & Segev, I. (1991). Effect of geometrical irregularities on propagation delay in axonal trees. *Biophysical Journal* **60**, 1424-1437.
- Markram, H., Lübke, J., Frotscher, M., Roth, A. & Sakmann, B. (1997). Physiology and anatomy of synaptic connections between thick tufted pyramidal neurones in the developing rat neocortex. *Journal of Physiology* **500**, 409-440.
- Martina, M., Vida, I. & Jonas, P. (2000). Distal initiation and active propagation of action potentials in interneuron dendrites. *Science* **287**, 295-300.
- Mel, B.W. (1993). Synaptic integration in an excitable dendritic tree. *Journal of Neurophysiology* **70**, 1086-1101.
- Mel, B.W. (1994). Information processing in dendritic trees. *Neural Computation* **6**, 1031-1085.
- Mennerick, S. & Zorumski, C.F. (1995). Presynaptic influence on the time course of fast excitatory synaptic currents in cultured hippocampal cells. *Journal of Neuroscience* **15**, 3178-3192.
- Migliore, M., Hoffman, D.A., Magee, J.C. & Johnston, D. (1999). Role of an A-type K<sup>+</sup> conductance in the back-propagation of action potentials in the dendrites of hippocampal pyramidal neurons. *Journal of Computational Neuroscience* **7**, 5-15.
- Miles, R., Toth, K., Gulyás, A., Hájos, N. & Freund, T. (1996). Differences between dendritic and somatic inhibition in the hippocampus. *Neuron* **16**, 815-823.
- Nedivi, E., Wu, G.Y. & Cline, H.T. (1998). Promotion of dendritic growth by CPG15, an activity-induced signaling molecule. *Science* **281**, 1863-1866.

Nelson, P.G., Pun, R.Y.K. & Westbrook, G.L. (1986). Synaptic excitation in cultures of mouse spinal cord neurones: receptor pharmacology and behaviour of synaptic currents. *Journal of Physiology* **372**, 169-190.

O'Dowd, D.K., Ribera, A.B. & Spitzer, N.C. (1988). Development of voltage-dependent calcium, sodium, and potassium currents in *Xenopus* spinal neurons. *Journal of Neuroscience* **8**, 792-805.

Ohme, M. & Schierwagen, A. (1998). An equivalent cable model for neuronal trees with active membrane. *Biological Cybernetics* **78**, 227-243.

Paré, D., Lang, E.J. & Destexhe, A. (1998). Inhibitory control of somatodendritic interactions underlying action potentials in neocortical pyramidal neurons *in vivo*: an intracellular and computational study. *Neuroscience* **84**, 377-402.

Parnas, I. & Segev, I. (1979). A mathematical model for conduction of action potentials along bifurcating axons. *Journal of Physiology* **295**, 323-343.

Pastushenko, V.F., Markin, V.S. & Chizmadzhev, Y.A. (1969). Impulse propagation in a model of a non-uniform nerve fiber. 3. Interaction of impulses in the area of a branching node of a nerve fiber. *Biofizika* **14**, 883-890.

Paternain, A.V., Morales, M. & Lerma, J. (1995). Selective antagonism of AMPA receptors unmasks kainate receptor-mediated responses in hippocampal neurons. *Neuron* **14**, 185-189.

Pauwelussen, J. (1982). One way traffic of pulses in a neuron. *Journal of Mathematical Biology* **151**, 151-172.

Pearce, R.A. (1993). Physiological evidence for two distinct GABA<sub>A</sub> responses in rat hippocampus. *Neuron* **10**, 189-200.

Peters, A., Kaiserman-Abramof, I.R. (1970). The small pyramidal neuron of the rat cerebral cortex: the perikaryon, dendrites and spines. *American Journal of Anatomy* **127**, 321-356.

Pinsky, P.F. & Rinzel, J. (1994). Intrinsic and network rhythmogenesis in a reduced Traub model for CA3 neurons. *Journal of Computational Neuroscience* **1**, 39-60.



Poirazi, P., Brannon, T. & Mel, B.W. (2003). Pyramidal neuron as two-layer neural network. *Neuron* **37**, 989-999.

Poirazi, P. & Mel, B.W. (2001). Impact of active dendrites and structural plasticity on the memory capacity of neural tissue. *Neuron* **29**, 779-796.

Press, W.H., Teukolsky, S.A., Vetterling, W.T. & Flannery, B.P. (1992). *Numerical Recipes in C*, Second Edition. Cambridge UP, Cambridge.

Provencher, S.W. (1976). A Fourier method for the analysis of exponential decay curves. *Biophysical Journal* **16**, 27-41.

Purves, D. & Hadley, R.D. (1985). Changes in the dendritic branching of adult mammalian neurones revealed by repeated imaging *in situ*. *Nature* **315**, 404-406.

Rall, W. (1964). Theoretical significance of dendritic trees for neuronal input-output relations. In: *Neural Theory and Modeling*, Ed. R.F. Reiss. Stanford University Press, Palo Alto, pp. 73-97.

Rall, W. (1967). Distinguishing theoretical synaptic potentials computed for different soma-dendritic distributions of synaptic input. *Journal of Neurophysiology* **30**, 1138-1168.

Rall, W. (1969). Time constants and electrotonic length of membrane cylinders and neurons. *Biophysical Journal* **9**, 1483-1508.

Rall, W. & Segev, I. (1985). Space-clamp problems when voltage clamping branched neurons with intracellular microelectrodes. In: *Voltage and Patch Clamping with Microelectrodes*, Eds. T.G. Smith, H. Lecar, S.J. Redman and P. Gage. American Physiological Society, Bethesda, MD, pp. 191-215.

Ramon, F., Joyner, R.W. & Moore, J.W. (1975). Propagation of action potentials in inhomogeneous axon regions. *Federation Proceedings* **34**, 1357-1363.

Ramón y Cajal, S. (1904). *La Textura del Sistema Nerviosa del Hombre y los Vertebrados*. Moya, Madrid.

Rapp, M., Yarom, Y. & Segev, I. (1996). Modeling back propagating action potential in weakly excitable dendrites of neocortical pyramidal cells. *Proceedings of the National Academy of Sciences of the USA* **93**, 11985-11990, 1996.

Redman, S. (1973). The attenuation of passively propagating dendritic potentials in a motoneurone cable model. *Journal of Physiology* **234**, 637-664.

Rinzel, J. & Rall, W. (1974). Transient response in a dendritic neuron model for current injected at one branch. *Biophysical Journal* **14**, 759-790.

Rossi, D., Alford, S., Mugnaini, E. & Slater, N.T. (1995). Properties of transmission at a giant glutamatergic synapse in the cerebellum: the mossy fibre-unipolar brush cell synapse. *Journal of Neurophysiology* **74**, 24-42.

Roth, A. & Häusser, M. (2001). Compartmental models of rat cerebellar Purkinje cells based on simultaneous somatic and dendritic patch-clamp recordings. *Journal of Physiology* **535**, 445-472.

Sah, P. & Bekkers, J.M. (1996). Apical dendritic location of slow afterhyperpolarization current in rat hippocampal pyramidal neurons: implications for the integration of long-term potentiation. *Journal of Neuroscience* **15**, 4537-4542.

Schaefer, A.T., Helmstaedter, M., Sakmann, B. & Korngreen, A. (2003a). Correction of conductance measurements in non-space-clamped structures: 1. Voltage-gated K<sup>+</sup> channels. *Biophysical Journal* **84**, 3508-3528.

Schaefer, A.T., Larkum, M.E., Sakmann, B. & Roth, A. (2003b). Coincidence detection in pyramidal neurons is tuned by their dendritic branching pattern. *Journal of Neurophysiology* **89**, 3143-3154.

Schiller, J., Schiller, Y., Stuart, G. & Sakmann, B. (1997). Calcium action potentials restricted to distal apical dendrites of rat neocortical pyramidal neurons. *Journal of Physiology* **505**, 605-616.

Schoppa, N.E. & Westbrook, G.L. (1999). Regulation of synaptic timing in the olfactory bulb by an A-type potassium current. *Nature Neuroscience* **2**, 1106-1113.

Schneggenburger, R. & Konnerth, A. (1992). GABA-mediated synaptic transmission in neuroendocrine cells: a patch-clamp study in a pituitary slice preparation. *Pflügers Archiv* **421**, 364-373.

Schwindt, P.C. & Crill, W.E. (1998). Synaptically evoked dendritic action potentials in rat neocortical pyramidal neurons. *Journal of Neurophysiology* **79**, 2432-2446.

Seamans, J.K., Gorelova, N.A. & Yang, C.R. (1997). Contributions of voltage-gated Ca<sup>2+</sup> channels in the proximal versus distal dendrites to synaptic integration in prefrontal cortical neurons. *Journal of Neuroscience* **17**, 5936-5948.

Segev, I. (1992). Single neurone models: oversimple, complex and reduced. *Trends in Neurosciences* **15**, 414-421.

Segev, I. & Rall, W. (1998). Excitable dendrites and spines: earlier theoretical insights elucidate recent direct observations. *Trends in Neurosciences* **21**, 453-460.

Shelton, D.P. (1985). Membrane resistivity estimated for the Purkinje neuron by means of a passive computer model. *Neuroscience* **14**, 111-131.

Silver, R.A., Colquhoun, D., Cull-Candy, S.G. & Edmonds, B. (1996). Deactivation and desensitization of non-NMDA receptors in patches and the time course of EPSCs in rat cerebellar granule cells. *Journal of Physiology* **493**, 167-173.

Silver, R.A., Farrant, M. & Cull-Candy, S.G. (1995). Filtering of the synaptic current estimated from the timecourse of NMDA channel opening. *Society for Neuroscience Abstracts* **21**, 584.

Silver, R.A., Traynelis, S.F. & Cull-Candy, S.G. (1992). Rapid-time-course miniature and evoked excitatory currents at cerebellar synapses *in situ*. *Nature* **355**, 163-166.

Sjöström, P.J. & Nelson, S.B. (2002). Spike timing, calcium signals and synaptic plasticity. *Current Opinion in Neurobiology* **12**, 305-314.

Smith, T.G., Wuerker, R.B. & Frank, K. (1967). Membrane impedance changes during synaptic transmission in cat spinal motoneurons. *Journal of Neurophysiology* **30**, 1072-1096.

Softky, W. (1994). Sub-millisecond coincidence detection in active dendritic trees. *Neuroscience* **58**, 13-41.

Soltesz, I., Smetters, D.K. & Mody, I. (1995). Tonic inhibition originates from synapses close to the soma. *Neuron* **14**, 1273-1283.

Spruston, N., Jaffe, D.B. & Johnston, D. (1994). Dendritic attenuation of synaptic potentials and currents: the role of passive membrane properties. *Trends in Neurosciences* **17**, 161-166.

Spruston, N., Jaffe, D.B., Williams, S.H. & Johnston, D. (1993). Voltage- and space-clamp errors associated with the measurement of electrotonically remote synaptic events. *Journal of Neurophysiology* **70**, 781-802.

Spruston, N., Schiller, Y., Stuart, G. & Sakmann, B. (1995). Activity-dependent action potential invasion and calcium influx into hippocampal CA1 dendrites. *Science* **268**, 297-300.

Stratford, K.J., Mason, A.J.R., Larkman, A.U., Major, G. & Jack, J.J.B. (1989). The modelling of pyramidal neurones in the visual cortex. In: *The Computing Neuron*, Eds. R. Durbin, C. Miall and G. Mitchison. Addison-Wesley, Wokingham, pp. 296-321.

Strichartz, G.R. (1973). The inhibition of sodium currents in myelinated nerve by quaternary derivatives of lidocaine. *Journal of General Physiology* **62**, 37-57.

Stricker, C., Field, A.C. & Redman, S.J. (1996). Statistical analysis of amplitude fluctuations in EPSCs evoked in rat CA1 pyramidal neurons in vitro. *Journal of Physiology* **490**, 419-441.

Stuart, G. & Häusser, M. (1994). Initiation and spread of sodium action potentials in cerebellar Purkinje cells. *Neuron* **13**, 703-712.

Stuart, G.J. & Sakmann, B. (1994). Active propagation of somatic action potentials into neocortical pyramidal cell dendrites. *Nature* **367**, 69-72.

Stuart, G. & Sakmann, B. (1995). Amplification of EPSPs by axosomatic sodium channels in neocortical pyramidal neurons. *Neuron* **15**, 1065-1076.

Stuart, G., Schiller, J. & Sakmann, B. (1997a). Action potential initiation and propagation in rat neocortical pyramidal neurons. *Journal of Physiology* **505**, 617-632.

Stuart, G. & Spruston, N. (1998). Determinants of voltage attenuation in neocortical pyramidal neuron dendrites. *Journal of Neuroscience* **18**, 3501-3510.

Stuart, G., Spruston, N., Sakmann, B. & Häusser, M. (1997b). Action potential initiation and backpropagation in neurons of the mammalian CNS. *Trends in Neuroscience* **20**, 125-131.

Svoboda, K., Denk, W., Kleinfeld, D. & Tank, D.W. (1997). In vivo dendritic calcium dynamics in neocortical pyramidal neurons. *Nature* **385**, 161-165.

Svoboda, K., Helmchen, F., Denk, W. & Tank, D.W. (1999). Spread of dendritic excitation in layer 2/3 pyramidal neurons in rat barrel cortex in vivo. *Nature Neuroscience* **2**, 65-73

Turner, R.W., Meyers, D.E., Richardson, T.L. & Barker, J.L. (1991). The site for initiation of action potential discharge over the somatodendritic axis of rat hippocampal CA1 pyramidal neurons. *Journal of Neuroscience* **11**, 2270-2280.

Turrigiano, G.G. & Nelson, S.B. (2004). Homeostatic plasticity in the developing nervous system. *Nature Reviews Neuroscience* **5**, 97-107.

Ulrich, D. & Lüscher, H.-R. (1993). Miniature excitatory synaptic currents corrected for dendritic cable properties reveal quantal size and variance. *Journal of Neurophysiology* **69**, 1769-1773.

Wadiche, J.I. & Jahr, C.E. (2001). Multivesicular release at climbing fiber-Purkinje cell synapses. *Neuron* **32**, 301-313.

Walker, H.C., Lawrence, J.J. & McBain, C.J. (2002). Activation of kinetically distinct synaptic conductances on inhibitory interneurons by electrotonically overlapping afferents. *Neuron* **35**, 161-171.

Waters, J., Larkum, M., Sakmann, B. & Helmchen, F. (2003). Supralinear Ca<sup>2+</sup> influx into dendritic tufts of layer 2/3 neocortical pyramidal neurons *in vitro* and *in vivo*. *Journal of Neuroscience* **23**, 8558-8567.

Williams, S.R. & Stuart, G.J. (2000). Action potential backpropagation and somato-dendritic distribution of ion channels in thalamocortical neurons. *Journal of Neuroscience* **20**, 1307-1317.

Wu, G.Y. & Cline, H.T. (1998). Stabilization of dendritic arbor structure in vivo by CaMKII. *Science* **279**, 222-226.

Wu, G.Y., Zou, D.J., Rajan, I. & Cline, H.T. (1999). Dendritic dynamics in vivo change during neuronal maturation. *Journal of Neuroscience* **19**, 4472-4483.

Yacoubian, T.A. & Lo, D.C. (2000). Truncated and full-length TrkB receptors regulate distinct modes of dendritic growth. *Nature Neuroscience* **3**, 342-349.

Yuste, R., Gutnick, M.J., Saar, D., Delaney, K.R. & Tank, D.W. (1994). Ca<sup>2+</sup> accumulations in dendrites of neocortical pyramidal neurons: an apical band and evidence for two functional compartments. *Neuron* **13**, 23-43.

Zador, A.M., Agmon-Snir, H. & Segev, I. (1995). The morphoelectrotonic transform: a graphical approach to dendritic function. *Journal of Neuroscience* **15**, 1669-1682.

Zhang, S. & Trussell, L.O. (1994). Voltage clamp analysis of excitatory synaptic transmission in the avian nucleus magnocellularis. *Journal of Physiology* **480**, 123-136.

Zhu, J.J. (2000). Maturation of layer 5 neocortical pyramidal neurons: amplifying salient layer 1 and layer 4 inputs by Ca<sup>2+</sup> action potentials in adult rat tuft dendrites. *Journal of Physiology* **526**, 571-587.

## 5.2 Vita

Name Arnd Erich Roth

Address Abteilung Zellphysiologie  
Max-Planck-Institut für Medizinische Forschung  
Postfach 10 38 20  
D-69028 Heidelberg  
Germany

Telephone +49-6221-486-467  
Fax +49-6221-486-459  
E-mail roth@mpimf-heidelberg.mpg.de

Date of birth 28 October 1970  
Nationality German

### Education:

1990 Abitur, Ludwig-Georgs-Gymnasium Darmstadt  
1997 Diploma in Physics, University of Heidelberg  
Thesis: "Simulation der exzitatorischen synaptischen Übertragung zwischen detailliert rekonstruierten Nervenzellen"  
Supervisors: Professor C. Cremer & Professor B. Sakmann

### Awards and Distinctions:

1990 Dilthey prize of the Ludwig-Georgs-Gymnasium Darmstadt  
1996 Student of the Crete Course in Computational Neuroscience

### Teaching Experience:

1998 Teaching assistant, Crete Course in Computational Neuroscience, Heraklion, Greece.  
1999–2000 Supervision of the diploma thesis of Andreas Schaefer, "Untersuchung morphologischer Korrelate elektrophysiologischer Eigenschaften von Pyramidenzellen im Neocortex der Ratte", University of Heidelberg, Department of Physics, 2000.

- 2001 Teaching assistant, Informatics I, Interdisciplinary Center of Scientific Computing, University of Heidelberg.
- 2002, 2003 Teaching assistant, EU Advanced Course in Computational Neuroscience, Obidos, Portugal.

## 5.3 Publications

### 5.3.1 Papers

Roth, A. & London, M. (2004). Rebuilding dendritic democracy (editorial focus). *Journal of Neurophysiology*, in press.

Schaefer, A.T., Larkum, M.E., Sakmann, B. & Roth, A. (2003). Coincidence detection in pyramidal neurons is tuned by their dendritic branching pattern. *Journal of Neurophysiology* **89**, 3143-3154.

Lübke, J.\* , Roth, A.\* , Feldmeyer, D.\* & Sakmann, B.\* (2003). Morphometric analysis of the columnar innervation domain of neurons connecting layer 4 and layer 2/3 of juvenile rat barrel cortex. *Cerebral Cortex* **13**, 1051-1063.

Brecht, M., Roth, A. & Sakmann, B. (2003). Dynamic receptive fields of reconstructed pyramidal cells in layers 3 and 2 of rat somatosensory barrel cortex. *Journal of Physiology* **553**, 243-265.

Roth, A. & Häusser, M. (2001). Compartmental models of rat cerebellar Purkinje cells based on simultaneous somatic and dendritic patch-clamp recordings. *Journal of Physiology* **535**, 445-472.

Vetter, P.\* , Roth, A.\* & Häusser, M. (2001). Propagation of action potentials in dendrites depends on dendritic morphology. *Journal of Neurophysiology* **85**, 926-937.

Markram, H., Roth, A. & Helmchen, F. (1998). Competitive calcium binding: implications for dendritic calcium signaling. *Journal of Computational Neuroscience* **5**, 331-348.

Geiger, J.R.P., Lübke, J., Roth, A., Frotscher, M. & Jonas, P. (1997). Submillisecond AMPA receptor-mediated signaling at a principal neuron-interneuron synapse. *Neuron* **18**, 1009-1023.



Häusser, M. & Roth, A. (1997). Estimating the time course of the excitatory synaptic conductance in neocortical pyramidal cells using a novel voltage jump method. *Journal of Neuroscience* **17**, 7606-7625.

Häusser, M. & Roth, A. (1997). Dendritic and somatic glutamate receptor channels in rat cerebellar Purkinje cells. *Journal of Physiology* **501**, 77-95.

Ullman, S., Roth, A., Thomson, A. & Linne, M.-L. (1997). Create, channels, cells, circuits and computers. *Trends in Neurosciences* **20**, 53-54.

Markram, H., Lübke, J., Frotscher, M., Roth, A. & Sakmann, B. (1997). Physiology and anatomy of synaptic connections between thick tufted pyramidal neurones in the developing rat neocortex. *Journal of Physiology* **500**, 409-440.

Brown, T.J.N., Mallion, R.B., Pollak, P. & Roth, A. (1996). Some methods for counting the spanning trees in labeled molecular graphs, examined in relation to certain fullerenes. *Discrete Applied Mathematics* **67**, 51-66.

Roth, A. (1990). Pendelauslösung der Kugelpyramide. *Praxis der Naturwissenschaften Physik* **40**, 46-47.

\* equal contribution

### 5.3.2 Book chapters

Geiger, J.R.P., Roth, A., Taskin, B. & Jonas, P. (1999). Glutamate-mediated synaptic excitation of cortical interneurons. In: *Ionotropic Glutamate Receptors in the CNS* (vol. 141 of *Handbook of Experimental Pharmacology*), Eds. P. Jonas and H. Monyer. Springer-Verlag, Berlin, pp. 363-398.

Sakmann, B., von Kitzing, E. & Roth, A. (1998). Unitary EPSPs in pairs of anatomically reconstructed cortical pyramidal neurons. In: *Central Synapses: Quantal Mechanisms and Plasticity*, Eds. D.S. Faber, H. Korn, S.J. Redman, S.M. Thompson and J.S. Altman. HFSP, Strasbourg, pp. 64-73.

### 5.3.3 Abstracts

Feldmeyer, D., Lübke, J., Roth, A. & Sakmann, B. (2002). Columnar and transcolumar organisation of axonal and dendritic domains in synaptically coupled neurons in cortical layer 4 and 2/3 of the rat barrel cortex. *FENS Abstracts* **1**, A015.13.

Roth, A., Wilkinson, J.A., Cottingham, C.A., Nusser, Z. & Häusser, M. (2001). Spatiotemporal dynamics of transmitter diffusion at excitatory synapses in the cerebellar cortex. *Society for Neuroscience Abstracts* **27**, 155.6.

Roth, A., Ohana, O., Sätzler, K., Geiger, J.R.P., Frotscher, M., Sakmann, B. & Lübke, J. (2000). 3-D reconstruction of synapses onto layer 5 pyramidal neurons in rat somatosensory cortex. *Society for Neuroscience Abstracts* **26**, 1122.

Nusser, Z., Roth, A., Schorge, S. & Häusser, M. (2000). Simulations of synaptic transmission in 3-D reconstructions of cerebellar neuropil. *Society for Neuroscience Abstracts* **26**, 1122.

Lübke, J.H.R., Sätzler, K., Söhl, L., Roth, A., Eils, R., Frotscher, M. & Sakmann, B. (2000). The Calyx of Held: 3-D reconstruction and quantitative analysis of its morphology. *Society for Neuroscience Abstracts* **26**, 676.

Schaefer, A.T., Roth, A. & Sakmann, B. (2000). Morphological correlates of BAC-firing threshold in model layer 5 pyramidal neurons. *European Journal of Neuroscience* **12** Suppl. 11, 369.

Häusser, M., Nusser, Z. & Roth, A. (2000). Modelling synaptic transmission at granule cell-Purkinje cell synapses. *European Journal of Neuroscience* **12** Suppl. 11, 182.

Roth, A., Nusser, Z. & Häusser, M. (2000). Monte Carlo simulations of synaptic transmission in detailed three-dimensional reconstructions of cerebellar neuropil. *European Journal of Neuroscience* **12** Suppl. 11, 14.

Egger, V., Roth, A. & Feldmeyer, D. (2000). Detailed passive compartmental models of spiny stellate neurons in juvenile rat barrel cortex. *Pflügers Archiv* **439**, R364.

Taskin, B., Roth, A., Lübke, J., Geiger, J.R.P. & Jonas, P. (2000). A detailed passive cable model of a dentate gyrus interneuron of rat hippocampus. *Pflügers Archiv* **439**, R364.

Roth, A. & Häusser, M. (1999). Compartmental models of rat cerebellar Purkinje cells constrained using simultaneous somatic and dendritic patch-clamp recording. *Journal of Physiology* **518.P**, 142P.

Vetter, P., Roth, A. & Häusser, M. (1999). Relating morphology and signal propagation in neuronal dendrites using compartmental modelling. *Journal of Physiology* **518.P**, 8P.

Lübke, J., Roth, A., Ohana, O., Sätzler, K., Frotscher, M. & Sakmann, B. (1999). Three-dimensional reconstruction of synapses onto layer 5 pyramidal neurons in rat somatosensory cortex from serial thin sections. *Göttingen Neurobiology Report 1999*, vol. II, 635.

Häusser, M., Vetter, P. & Roth, A. (1998). Action potential backpropagation depends on dendritic geometry. *Society for Neuroscience Abstracts* **24**, 1813.

Häusser, M. & Roth, A. (1996). A method for determining the time course of the synaptic conductance under conditions of inadequate space clamp. *Society for Neuroscience Abstracts* **22**, 1742.

Geiger, J.R.P., Lübke, J., Frotscher, M., Roth, A. & Jonas, P. (1996). Pre- and postsynaptic factors determine synaptic integration of glutamate-mediated EPSPs in GABAergic interneurons of the hippocampus. *Society for Neuroscience Abstracts* **22**, 495.

Roth, A. & Sakmann, B. (1995). Programmbausteine zur Simulation exzitatorischer synaptischer Übertragung zwischen detailliert rekonstruierten Nervenzellen. *SINN '95*, Lindau.



## 6 Abbreviations

|                 |  |
|-----------------|--|
| AMPA            | L- $\alpha$ -amino-3-hydroxy-5-methyl-4-isoxazolepropionic acid  |
| AP              | Action potential   |
| APV             | D-2-amino-5-phosphonovaleric acid, an antagonist of NMDA-type glutamate receptors  |
| ATP             | Adenosine triphosphate   |
| BAPTA           | 1,2,-bis-(2-aminophenoxy)ethane-N,N,N',N'-tetraacetic acid, a fast buffer of Ca <sup>2+</sup> ions   |
| C <sub>m</sub>  | Specific membrane capacitance (in $\mu\text{F cm}^{-2}$ )  |
| CNQX            | 6-cyano-7-nitroquinoxaline-2,3-dione, an antagonist of AMPA-type glutamate receptors   |
| EGTA            | Ethylene glycol-bis(b-aminoethyl-ether)-N,N,N',N'-tetraacetic acid, a slow buffer of Ca <sup>2+</sup> ions                                       |
| EM              | Electron microscope  |
| EPSC            | Excitatory postsynaptic current (in pA)  |
| EPSP            | Excitatory postsynaptic potential (in mV)  |
| $g_K$           | K <sup>+</sup> channel density (in pS $\mu\text{m}^{-2}$ )   |
| $g_{Na}$        | Na <sup>+</sup> channel density (in pS $\mu\text{m}^{-2}$ )  |
| $g_{Na,thresh}$ | Minimum Na <sup>+</sup> channel density required for full backpropagation of the AP (peak membrane potential > 0 mV) into all dendritic branches |
| GABA            | $\gamma$ -aminobutyric acid, an inhibitory neurotransmitter in the central nervous system  |
| Hepes           | 4-(2-hydroxyethyl)piperazine-1-ethanesulfonic acid   |
| I <sub>h</sub>  | Hyperpolarization-activated cation current   |
| IPSC            | Inhibitory postsynaptic current  |
| IPSP            | Inhibitory postsynaptic potential  |
| LM              | Light microscope   |
| NA              | Numerical aperture   |
| NMDA            | N-methyl-D-aspartate   |
| P               | Postnatal day  |
| PBS             | Phosphate-buffered saline  |
| QX-314          | Lidocaine N-ethyl bromide, a blocker of various types of voltage-gated channels  |
| $R_i$           | Specific resistivity of the intracellular medium (in $\Omega \text{ cm}$ )   |
| $R_m$           | Specific membrane resistance (in $\Omega \text{ cm}^2$ )   |
| S.E.M.          | Standard error of the mean   |

|          |  |
|----------|--|
| S.D.     | Standard deviation   |
| $\tau_m$ | $= R_m * C_m$ , membrane time constant   |
| TEA      | Tetraethylammonium, a blocker of voltage-gated K <sup>+</sup> channels   |
| TTX      | Tetrodotoxin, used to block voltage-gated Na <sup>+</sup> channels   |
| ZD 7288  | 4-ethylphenylamino-1,2-dimethyl-6-methylaminopyrimidinum chloride, a blocker of the hyperpolarization-activated current I <sub>h</sub> |